5-2017

# Computational Thermal-Hydraulics Modeling of Twisted Tape Enabled High Heat Flux Components

Emily Buckman Clark
*University of Tennessee, Knoxville*, ebuckman@vols.utk.edu

To the Graduate Council:

I am submitting herewith a dissertation written by Emily Buckman Clark entitled "Computational Thermal-Hydraulics Modeling of Twisted Tape Enabled High Heat Flux Components." I have examined the final electronic copy of this dissertation for form and content and recommend that it be accepted in partial fulfillment of the requirements for the degree of Doctor of Philosophy, with a major in Energy Science and Engineering.

Arnold Lumsdaine, Kivanc Ekici, Major Professor

We have read this dissertation and recommend its acceptance:

Arthur Ruggles, David Donovan

Accepted for the Council:

Dixie L. Thompson

Vice Provost and Dean of the Graduate School

(Original signatures are on file with official student records.)

# Computational Thermal-Hydraulics Modeling of Twisted Tape Enabled High Heat Flux Components

A Dissertation Presented for the
Doctor of Philosophy
Degree
The University of Tennessee, Knoxville

Emily Buckman Clark
May 2017

*To my husband, John, for your unwavering support and confidence in me. I can't wait to start our next adventure.*

*To my parents, Diana and Mitch, for always believing in me and pushing me to succeed. You showed me the drive to make this possible.*

# Acknowledgements

This accomplishment would not have been possible without the support of a great number of people. Thank you to my advisors Dr. Kivanc Ekici and Dr. Arnold Lumsdaine. Thank you to Dr. Ekici for supporting me throughout my whole graduate school experience. He saw the potential in me and gave me the opportunities to make me the researcher and engineer that I am today. Thank you to Dr. Lumsdaine for bringing me into the world of fusion energy. He showed me that I can be flexible with my skills and taught me how to approach a problem even if I know nothing about it. I would also like to thank Dr. Art Ruggles for his mentorship and guidance. He showed me the value of a questioning attitude and instilled the importance of driving towards a goal.

I wouldn't be where I am today without the Bredesen Center. Thank you to Dr. Lee Riedinger for bringing me into the family and giving me the opportunity to pursue this work. Joining the Bredesen Center was the best decision of my graduate career. The Bredesen Center opened my eyes to the wide world of possibilities that scientists can achieve. It not only taught me how to communicate effectively with both scientists and the public but also why it's important to do so. The Bredesen Center showed me the importance of looking at the bigger picture, and I know that perspective will be invaluable in my career.

I would also like to thank those who supported my work at Oak Ridge National Laboratory in the Fusion and Materials for Nuclear Systems Division. Thank you to Phil Ferguson and Gary Bell for supporting me as I developed my skills. Thank you to Jean Boscary for his collaboration and guidance on this work. Furthermore, thank you to the Office of Fusion Energy Sciences, which generously funded this collaboration with the Wendelstein 7-X experiment.

Lastly, this work would not have been possible without the support of my closest friends. Thank you to Jordan Sawyer, Zeke Stannard, and Michael Merriweather. As we continue our careers and move apart, I know we'll always be "BEFFs." Thank you to Guinevere Shaw for our countless hours of discussion and laughter. Your passion and drive

are inspirational. Thank you to Mark Christian for our brainstorming sessions and discussions. I know you will meet your goals. Finally, thank you to Kate Manz and Reed Wittman. From football games to dinner parties, we always had a great time and a ton of laughs. I can't wait to see where your careers take you. Friends are the family we choose for ourselves, and the Clarks choose all of you.

# Abstract

The goal of this work was to perform a computational investigation into the thermal-hydraulic performance of water-cooled, twisted tape enabled high heat flux components at fusion relevant conditions. Fusion energy is a promising option for future clean energy generation, but the community must overcome significant scientific and engineering challenges before meeting the goal of electricity generation. One such challenge is the high heat flux thermal management of components in fusion and plasma physics experiments. Plasma facing components in the magnetic confinement devices, such as ITER or W7-X, will be subjected to extreme heat loads on the order of 10-20 $MW/m^2$. The heat dissipation issue will become critical as these next generations of experiments come online, and active cooling will be necessary to decrease the thermal loading and prevent failure of the components.

Single-phase computational modeling was performed with the ANSYS CFX software to investigate the performance of water-cooled twisted tape devices. Computational investigations were first performed for a general geometry at moderate conditions and were then ramped up to fusion relevant conditions. This work resulted in a wide range of topics including comparisons to experiments and legacy correlations, comparisons of various turbulence models, investigations into local information, a parametric sweep of different tape characteristics, and identification of future opportunities.

Key results stemmed from the investigation into the local flow field. The work revealed characteristics of twisted tape enabled swirl flow, which has not yet been noted in the literature. Secondary circulation resulted in so-called “inflow” regions, where the boundary layer was reinjected into the freestream. At moderate, uniform heating conditions, these regions were shown to correspond to regions of low wall shear stress, low heat transfer coefficients, and high surface temperatures making them candidates for early burnout. Investigation of wall shear stress contours revealed apparent “striping” that develops in twisted tape induced swirl flow due to the secondary circulation. While these key qualitative features were still noted in the fusion relevant investigation, the connection

between the inflow regions and surface temperature was concluded to be minimal under one-sided, high heat flux conditions.

# Table of Contents

# List of Tables

# List of Figures

# Nomenclature

### *Abbreviations*

| | |
|---|---|
| AMC® | Active metal casting |
| CB | Center beam location |
| CC | Curvature correction method |
| cc | Contact conductance |
| CFC | Carbon-carbon fiber composite |
| CFD | Computational fluid dynamics |
| GLADIS | Garching Large Divertor Sample |
| HTC | Heat transfer coefficient |
| IAPWS | International Association for the Properties of Water and Steam |
| IF-97 | Industrial Formulation 1997 |
| k-eps | Standard k-epsilon model |
| low Re | Low Reynolds number approach |
| MB | Manglik and Bergles correlation [15] |
| PFCs | Plasma facing components |
| PHF | Peak heat flux |
| RANS | Reynolds averaged Navier-Stokes |
| RMS | Root mean square |
| RNG k-eps | Renormalized group k-epsilon model |
| RSM | Reynolds stress model |
| SS | Steady state |
| SST | Shear stress transport model |
| TC1 | First transient refinement |

| | |
|---|---|
| TC2 | Second transient refinement |
| TCR | Thermal contact resistance |
| Ts | Surface temperature |
| Tsat | Saturation temperature |
| W7-X | Wendelstein 7-X |

***Symbols***

| | |
|---|---|
| a | Speed of sound |
| $A_c$ | Cross-sectional area |
| C | Dimensionless integration constant |
| $C_f$ | Fanning friction factor |
| $c_p$ | Specific heat at constant pressure |
| $c_v$ | Specific heat at constant volume |
| d | Empty tube diameter |
| G | Mass flux |
| $\vec{g}$ | Gravity vector |
| H | 180 degree twist pitch |
| h | Enthalpy |
| HTC | Heat transfer coefficient |
| k | Thermal conductivity |
| L | Total length |
| $L_C$ | Calming length |
| $L_{ent}$ | Entrance length |
| $L_{exit}$ | Exit length |
| $L_H$ | Heated length |
| $L_{swirl}$ | Swirling length |

| | |
|---|---|
| M | Mach number |
| $\dot{m}$ | Mass flow rate |
| Nu | Nusselt number |
| P | Pressure |
| Pr | Prandtl number |
| ΔP | Pressure drop |
| $q''$ | Heat flux |
| R | Universal gas constant |
| Re | Reynolds number |
| $S_{ij}$ | Strain rate tensor |
| T | Temperature |
| t | Time |
| $T^+$ | Dimensionless temperature |
| $\Delta T_{edges}$ | Monoblock edge temperature difference |
| u | Axial velocity |
| $u^+$ | Dimensionless velocity |
| $u^*$ | Alternative velocity scale in ANSYS CFX |
| $\vec{V}$ | Velocity vector |
| y | Twist ratio |
| $y^+$ | Non-dimensional wall coordinate |
| $y^*$ | Alternative non-dimensional wall distance in ANSYS CFX |
| $\tilde{y}^*$ | Calculated non-dimensional wall distance in ANSYS CFX |
| Δy | Distance from the wall in ANSYS CFX |
| Z | Compressibility factor |
| z | Axial location along the test section |

| | |
|---|---|
| $\beta$ | Volumetric coefficient of thermal expansion |
| $\gamma$ | Ratio of specific heats |
| $\delta$ | Twisted tape width |
| $\delta_{ij}$ | Kronecker delta function |
| $\theta$ | Circumferential angular coordinate |
| $\kappa$ | Kármán's constant |
| $\lambda$ | Coefficient of bulk viscosity |
| $\mu$ | Dynamic viscosity |
| $\mu_t$ | Eddy viscosity |
| $\nu$ | Kinematic viscosity |
| $\nu^*$ | Friction velocity |
| $\rho$ | Density |
| $\tau_{ij}$ | Reynolds stress tensor |
| $\tau_w$ | Wall shear stress |
| $\phi$ | CFC misalignment angle |

***Subscripts***

| | |
|---|---|
| a | Axial flow condition |
| b | Bulk property |
| D | Based on empty tube diameter |
| diabatic | Heated conditions |
| h | Hydraulic diameter |
| in | Inlet condition |
| iso | Isothermal conditions |
| m | Mean or bulk property |
| o | Near the outlet |
| s | Swirl flow condition |

# Chapter 1: Introduction

Nuclear fusion is the process that powers the sun and the stars. Since the mid-20th century, scientists and engineers have been working to create and to harness those fusion reactions here on Earth with the ultimate goal of generating electricity. By achieving that goal, the fusion community will create a groundbreaking source of nearly unlimited, clean, and reliable energy for the world for generations to come. The community is currently moving towards this purpose with research of magnetic confinement devices such as the ITER tokamak and the Wendelstein W7-X (W7-X) stellarator. In such machines, fusion reactions result in a superheated gas, or plasma, that is confined by magnetic fields. Existing magnetic confinement devices will facilitate plasma physics experiments to help scientists learn more about the plasma and its interaction with internal components. This knowledge will then be used to design a next-generation machine, such as DEMO, that will aim to demonstrate the capability to generate electricity from fusion reactions [1]. While fusion is a promising option for future clean energy generation, the field must still overcome significant scientific and engineering challenges. One such challenge is the high heat flux thermal management of components in fusion and plasma physics experiments. The plasma facing components (PFCs) in magnetic confinement devices, such as ITER or W7-X, will be subjected to extreme heat fluxes as high as 10-20 $MW/m^2$. The heat dissipation issue will become critical as this next generation of experiments come online, and active cooling will be an essential element.

Active cooling will be utilized to decrease the thermal loading and to prevent the failure of PFCs. Throughout the years, many coolants have been proposed for active cooling including helium, liquid metals, and water [2]. While there have been recent advancements in helium cooling, water is commonly chosen as the coolant in current generation devices and is the focus of this work. The current state-of-the-art water-cooled technologies can accommodate extremely high heat fluxes. These technologies often utilize passive heat transfer enhancement techniques, such as fins or swirl flow, to decrease the thermal loading on the components and typically involve the use of subcooled boiling due to the

extreme heat loads experienced. Swirling flow is a common enhancement technique used for cooling PFCs; the swirling motion is often induced with a twisted tape that is inserted into a circular tube. Such twisted tape devices are planned for widespread use across the fusion community with implementations in machines such as W7-X, ITER, and WEST [3-5].

Overall, the goal of this dissertation research was to computationally investigate the thermal-hydraulic performance and characteristics of twisted tape enabled high heat flux components at fusion relevant conditions. While there have been many studies on the current state-of-the-art water-cooled technologies, the basic physical mechanism for their effectiveness is not well understood, and there are a host of topics that could be studied to further the field. A computational multiphysics analysis of water-cooled PFCs was performed based on W7-X parameters by Clark et al. [3]. This investigation of W7-X PFCs revealed the need to include the subcooled nucleate boiling process for a more accurate heat transfer model. Following the initial study, this author's work focused on the development of a two-phase model for twisted tape enabled high heat flux components. While computational fluid dynamics (CFD) and thermal models are well established for the single-phase regime, multiphase models are only starting to become a focus in the computational community. Nevertheless, there are commercial options available for modeling two-phase flow. In general, these commercial codes have similar multiphase capabilities. The governing equations are solved and mechanistic models are implemented to account for the phase change process when applicable. The mechanistic models, such as the RPI boiling model developed by Kurul and Podowski, are mostly based on a specific range of data [6]. For example, a vast majority of computational two-phase investigations benchmark their codes against the experimental work of Bartolomei and Chanturiya and then extrapolate to their application of interest [7]. In the case of fusion relevant conditions, the heat fluxes and flow rates are often one or two orders of magnitude higher than the conditions used to develop the mechanistic boiling models. Because PFC conditions extend so far past the typical boiling parameters, it was concluded that an accurate single-phase twisted tape induced swirl flow model was a pre-requisite to the addition of the second phase.

This dissertation will focus on single-phase computational modeling to investigate the thermal-hydraulic performance of water-cooled twisted tape devices. In the past, there have been a substantial number of experimental studies to investigate the twisted tape thermal-hydraulic design characteristics for single-phase convection [8]. However, there have been fewer computational studies concerning single-phase, turbulent swirl flow. Additionally, a majority of these computational works have focused on the determination of global thermal-hydraulic design characteristics rather than investigating the local flow features. Unfortunately, these studies generally exclude the benefit of computational solutions where local flow information can be extracted more easily than in an experimental setting. This work aims to exploit the advantage of computational simulations by investigating local flow information, and it will highlight future opportunities for furthering the understanding of twisted tape induced swirl flow in both the computational and experimental realms.

# Chapter 2: Background

## 2.1. Twisted Tape Background

Twisted tape devices have a long history in the heat transfer enhancement community. The first scientific experiment concerning the practical use of a twisted tape was recorded in 1896, and its application to water flows began in the 1960s due to rapid developments in nuclear fission power generation [8]. Twisted tapes are categorized as a passive heat transfer enhancement technique. Passive heat transfer enhancement techniques utilize surface modifications or integrate an additional device into the system. Examples of passive techniques include treated surfaces, coiled tubes, fluid additives, or fluid inserts. In general, these devices promote higher heat transfer coefficients by disturbing or changing the flow behavior, and they often generate "well-mixed" flows leading to sharper wall-temperature gradients than normal. The heat transfer enhancement in twisted tape devices is mostly attributed to the increased mixing that is generated by the swirling motion of the fluid along with some contributions from an increased effective flow length and increased flow velocity in the partitioned duct. While these devices are more thermally efficient, there is often a trade-off with increased hydraulic resistance leading to larger pressure drops [8].

Twisted tapes are versatile devices that can be used in a variety of applications for laminar or turbulent conditions in both single- and two-phase flow regimes. In addition to fusion cooling devices, some other applications of twisted tapes include heat exchangers, solar water heaters, and diesel engine cooling [8-11]. Twisted tapes are created by twisting a thin, metallic strip into a constant pitch helix. They are inserted into tubes to induce swirling flow in the fluid path. It is common to have a small gap between the tube wall and the tape, although the tape width is often approximated as the tube inside diameter [8]. The key geometric characteristics are shown in Figure 2.1 from Ref. [12]. The severity of the pitch is characterized by the dimensionless twist ratio ($y$) such that $y=H/d$ where $H$ is the 180° twist pitch and $d$ is the inside tube diameter.

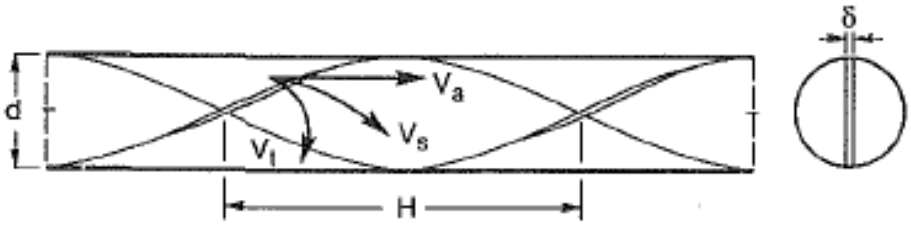


Figure 2.1: Twisted tape geometric characteristics from Ref. [12]

## 2.2. Current Status of Twisted Tape Research

### *2.2.1. Experimental Works*

#### *Development of Thermal-Hydraulic Correlations*

Because of their versatile nature, twisted tape devices have been widely studied for decades. Manglik and Bergles performed an extensive review of twisted tape literature in 2002 [8]. Their review highlights the substantial number of experimental studies related to twisted tapes. A majority of these were performed to investigate the heat transfer and pressure drop and to develop correlations for the thermal-hydraulic design characteristics such as the Nusselt number and Fanning friction factor [13-16].

Gambill et al. investigated the heat transfer, pressure drop, and burnout of water through tubes equipped with twisted tape inserts. Experiments were performed with electrically heated tubes for various tape twist ratios (2.3-12.0), heat fluxes (2.5-25 $MW/m^2$), and Reynolds numbers (Re) ($5x10^3$-$4.27x10^5$). Swirl flow heat transfer coefficients and friction factors were found to be larger than equivalent flow through a plain tube. The friction factors were found to be dependent on tube diameter and tape twist ratio but independent of Reynolds number [17].

Kidd investigated the heat transfer and pressure drop of nitrogen flowing in an electrically heated tube equipped with a twisted tape. The experiments ranged over various Reynolds numbers ($2x10^4$-$2x10^5$) and heat fluxes (0.03-0.3 $MW/m^2$) with twist ratios ranging from y=2.5-14. The results were found to be in good agreement with other experimental studies. An empirical correlation was developed for the heat transfer of

twisted tape induced gas flow, which was a function of the twist ratio, wall-to-gas temperature ratio, and the tube length [18].

Lopina and Bergles investigated the heat transfer and pressure drop of single-phase water in twisted tape generated swirl flow for twist ratios ranging from y=2.5-9. The isothermal and heated friction factors were investigated along with the Nusselt number for Reynolds numbers ranging from $1x10^4$-$1x10^5$. Thermal-hydraulic correlations were created from the experimental results and were shown to be in good agreement with data of other investigators [14].

Manglik and Bergles developed thermal-hydraulic correlations for flows with twisted tape inserts for both laminar and turbulent flow. Their goal was to develop generalized correlations that had a wide range of applicability. Experiments were performed with water and ethylene glycol with twisted tape inserts of three different twist ratios (3.0, 4.5, 6.0). The data covered a wide range of Prandtl numbers (3.5-100) and Reynolds numbers (300-$3.5x10^4$) for heating and cooling conditions [19]. The laminar and turbulent correlations were then developed from these experimental results [12, 15].

### *One-Sided Heating Experiments*

In addition to the focus on thermal-hydraulic correlations, a majority of twisted tape experiments utilized Joule heating of the tube to provide a relatively uniform heat flux to the system. However, in many fusion applications, PFCs are exposed to non-uniform one-sided heating conditions.

Araki et al. performed experiments for water-cooled smooth and swirl tubes under one-sided heating conditions for both single-phase and subcooled boiling conditions. The goal of the experiments was to establish a heat transfer correlation for water under one-sided heating. The experiments were performed in the Particle Beam Engineering Test Facility, where the heat flux was supplied by an ion source. The incident heat flux, which was increased from 2 $MW/m^2$ until burnout, was non-uniform and was applied to one side of the circular tube test sections. Experiments were performed with both plain tubes and tubes with twisted tape inserts. The swirl tubes had a twist ratio of y=3 and an inner

diameter of 10 mm; the flow velocity ranged from 4.2-16 m/s. The authors determined that existing heat transfer correlations were acceptable in the single-phase flow regime, but these correlations were unacceptable in the subcooled nucleate boiling regime. A new heat transfer correlation was proposed for the boiling regime [20].

Dedov et al. investigated the heat transfer and pressure drop of swirl flow under one-sided heating conditions for water-cooled ITER PFCs. Experiments were performed for four monoblock cross-sections, and the test sections were heated with an electron beam gun, which provided nearly uniform heating along the surface. The heat transfer in single-phase forced convection was investigated for twist ratios ranging from y=1.75-8.27 along with a straight tape (y=∞). Three heat flux values were investigated (2, 3, and 4.5 MW/m$^2$) across a range of Reynolds numbers (5x10$^3$-1x10$^5$). The Reynolds numbers given by Dedov et al. were based on the hydraulic diameter ($d_h$) such that $Re_h = \rho u d_h / \mu$. The authors determined that the pressure drop decreases with increasing wall temperature due to a decrease in the viscosity near the wall. This decrease in the pressure drop became less pronounced as the wall temperature approached the saturation temperature. Dedov et al. compared their data to a classical friction factor equation and determined that classical relations can be employed for swirl flow if they are edited to include the hydraulic diameter. Furthermore, the authors concluded that swirl flow heat transfer is not only affected by an increase in the flow velocity but also by body forces due to the swirling motion. A new heat transfer coefficient correlation was created for turbulent swirl flow under one-sided heating [21].

### *Flow Visualization Experiments*

Only a few experimental studies investigated the flow structure and the associated heat transfer enhancement in turbulent twisted tape induced swirl flow [8]. Smithberg and Landis and Seymour were two of the earliest studies that aimed to visualize the swirl flow structure in the turbulent regime [22, 23]. Both flow visualization studies used air as the working fluid and were performed under adiabatic conditions.

Seymour used a radioactive gas tracing method to view the swirl flow pattern at a Reynolds number of $3.1x10^5$ with a twist ratio of y=4.76. Using the same twist ratio, Seymour used a thermistor anemometer to determine axial velocity contours at a Reynolds number of $6.2x10^4$ [22]. Smithberg and Landis also developed axial velocity contours for a Reynolds number of $1.4x10^5$ with a twist ratio of y=5.15 [23]. The axial velocity contours for the two studies were qualitatively similar with both indicating secondary circulation due to a double vortex structure.

### *2.2.2. Computational Works*

#### *Classical Twisted Tape Inserts*

Compared to the vast amounts of experimental studies, there have been a limited number of computational investigations for turbulent twisted tape induced swirl flow. Rather than concentrating on local flow features, the majority of computational studies have focused on investigating the thermal-hydraulic design characteristics.

Date performed one of the first numerical investigations of twisted tape induced swirl flow in 1974. The problem of fully-developed, laminar and turbulent flow was formulated through partial differential equations for momentum and heat transfer considering uniform properties. The momentum and heat transfer equations were transformed into functions of the stream function and vorticity to allow for a simplified numerical solution. The constants of Jones and Launder [24], which are the basis for the standard k-epsilon model, were employed for turbulent flow, and the problem was solved with a finite difference method. The friction factor and Nusselt number were investigated for both laminar ($Re=40-2x10^3$) and turbulent ($Re=4x10^3-1x10^5$) flow fields across a range of twist ratios (2.25-15.72) along with a straight tape ($y=\infty$). The author found that the laminar flow predictions agreed with analytical solutions. However, the turbulent predictions using the standard k-epsilon constants were found to be insufficient as they led to an underprediction of the friction factor and Nusselt number [25].

Hata et al. performed a computational study of pressure drop and heat transfer for twisted tape induced swirl flow in a vertical tube, where the inner tube diameter was 6

mm. The study was completed with the PHOENICS code using the standard k-epsilon turbulence model. The solution was completed for a twist ratio of 3.39 for a range of heat fluxes (0.269-27.7 $MW/m^2$) and inlet velocities (4.13-13.63 m/s). The computational results were compared to experimental data at the same conditions, and the numerical solutions were in good agreement with the experiments in regards to the inner surface temperatures and the relation between the heat flux and the temperature difference [26].

Lumsdaine et al. performed CFD modeling to investigate the thermal-hydraulic performance of carbon-carbon fiber composite monoblock fingers equipped with a twisted tape, which are planned for use in the W7-X stellarator experiment. The modeling was performed with ANSYS CFX to determine if thermal and hydraulic design criteria would be met. The standard k-epsilon model was utilized in both the thermal and hydraulic solutions. A hydraulic analysis was performed for a single "module," which included four twisted tape enabled tubes connected by 180° bends. Each monoblock finger was equipped with a 12 mm inner diameter tube, and a twisted tape with a twist ratio of y=2. This analysis was completed for four flow rates ranging from 9.19-11.91 m/s. The authors noted that the computational results were about 25% higher than the Manglik and Bergles correlation [15] in the twisted tape regions. The thermal analysis was performed in CFX for one monoblock finger with a non-uniform heat flux, which peaked at 17 $MW/m^2$. The computational solution predicted a surface temperature near the design criteria limit, and highlighted the need for a more detailed CFD model including the addition of subcooled nucleate boiling [27].

### *Modified Twisted Tape Inserts*

In addition to the focus on global thermal-hydraulic effects, a significant portion of computational twisted tape studies are concerned with "modified" twisted tapes or loose-fit tapes rather than the traditional geometry [28-32]. Modified twisted tapes vary widely and include alterations such as a short tape near the tube inlet, short tapes interspaced throughout the tube, and variations in the geometry or surface (as seen in Figure 2.2) [8].

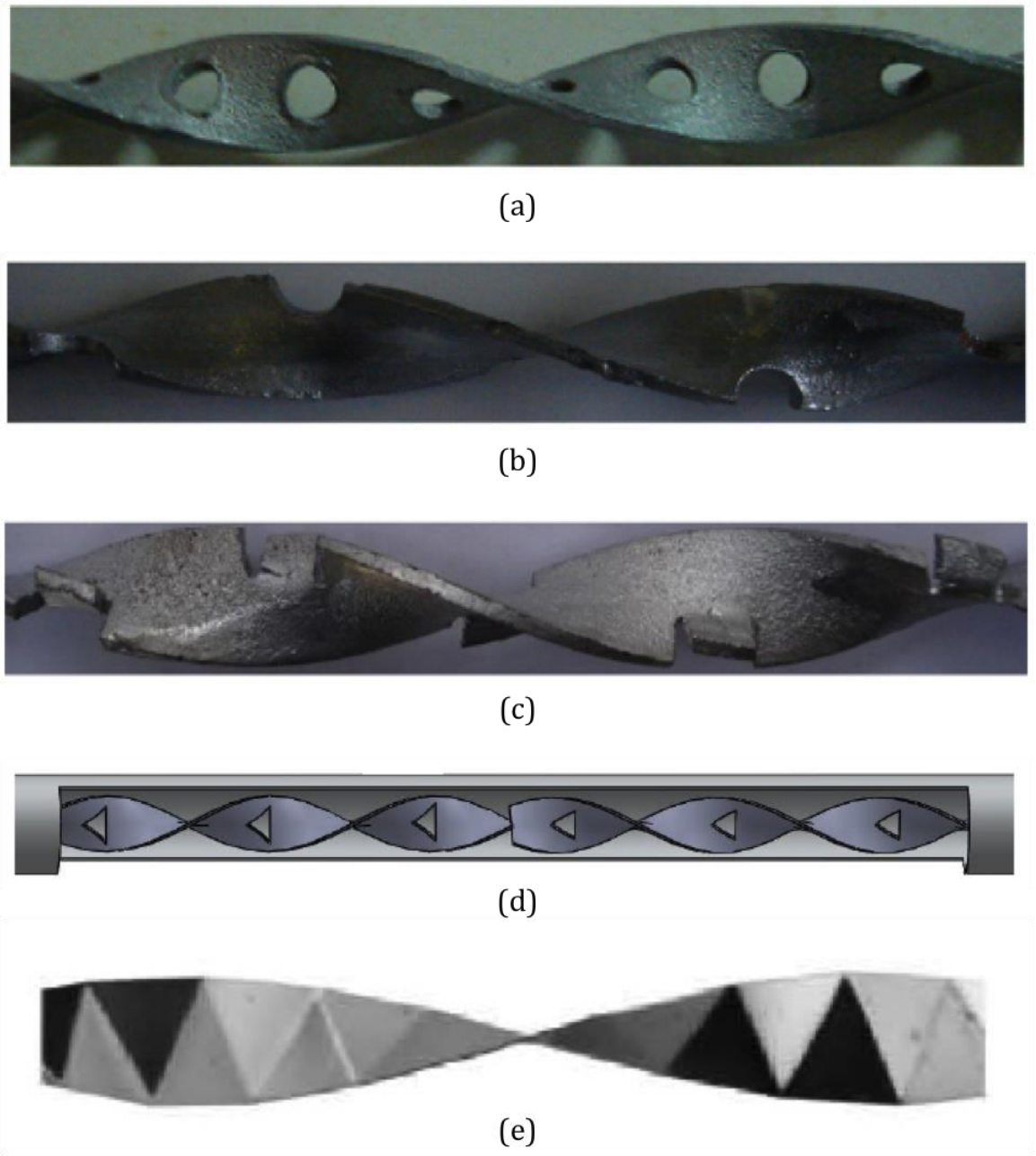


Figure 2.2: Modified twisted tape inserts with surface or geometry modifications including the (a) perforated twisted tape [28], (b) notched twisted tape [28], (c) jagged twisted tape [28], (d) triangular cut twisted tape [33, 34], and (e) edgefold twisted tape [31]

Rahimi et al. computationally investigated the thermal-hydraulic performance for a tube equipped with a classical twisted tape and three modified twisted tape inserts including "perforated," "notched," and "jagged" tapes (shown in Fig. 2.2). A conjugate heat transfer analysis was performed with the FLUENT6.2 software using the RNG k-epsilon model. The Reynolds number ranged from $2.95x10^3$ to $1.18x10^4$, and hot water at 42°C was flowed over a tube with cold water at 16°C. The friction factor and Nusselt number were calculated for each tape and were compared to that of an empty tube as well as the classic twisted tape. They determined that a "jagged" twisted tape yielded the best thermal-hydraulic performance over a classic insert due to an increased turbulent intensity [28].

Eiamsa-ard et al. 2009 performed computational simulations to investigate the effects of loose-fit twisted tapes with water as the testing fluid. The friction factor, Nusselt number, and a thermal performance factor were investigated for twisted tapes at two twist ratios (2.5, 5.0) at various tape widths. An isothermal simulation was performed using a finite volume method where the inner tube wall and inlet temperatures were kept at 36.85°C and 26.85°C, respectively, and the inlet Reynolds number ranged from $3x10^3$-$1x10^4$. The authors determined that, when compared to a plain tube, loose-fit tapes resulted in lower heat transfer enhancement as well as a lower increase in the friction factor than a tight-fit tape [29].

Liu and Bai studied helical vortices downstream of a short twisted tape placed near the inlet of a circular pipe. The numerical solution was completed with the FLUENT software, and two turbulence models were investigated including the RNG k-epsilon and the Reynolds stress model. A pipe with a 25.4 mm diameter was modeled with a short twisted tape ($y=2.36$) near the inlet region. The working fluid was room temperature water with an inlet velocity of 3.03 m/s. The authors determined that vortices formed in the region with the twisted tape and kept their structure downstream. The intensities of the helical vortices were found to increase with increasing Reynolds number [30].

Lei et al. compared the thermal-hydraulic performance of "staggered twisted tapes with central holes" to classical twisted tapes. Numerical solutions were completed for the two tape types using a finite volume method along with the RNG k-epsilon turbulence model.

Each type of twisted tape was modeled in a 19 mm diameter tube with a twist ratio of y=2. The solution was completed over Reynolds numbers ranging from $6x10^3$ to $2.8x10^4$. Unfortunately, there was no apparent discussion of the thermal boundary conditions, but the authors' resulting Nusselt numbers ranged from 100 to 350. The authors noted a better thermal-performance for the modified twisted tapes over the conventional approach. The hydraulic resistance was decreased along with an enhanced heat transfer for the staggered twisted tapes with central holes [32].

Oni and Paul performed a computational investigation of twisted tape equipped tubes where triangular cutouts were removed from the tape (as shown in Fig. 2.2). Their work focused on the effects of the cutout size on the thermal-hydraulic performance. Water was chosen for the working fluid, and seven modified twisted tapes were considered along with a plain tube. The computational solutions were performed for a range of Reynolds numbers ($5x10^3$-$2x10^4$) and twist ratios ($y\approx1.90$, 2.84, 3.79). A uniform heat flux was applied to the tube wall, and the flow field was solved with the use of the RNG k-epsilon turbulence model. The authors discovered that increasing the size of the cutouts enhanced the thermal performance of the system [34].

Cui and Tian investigated the heat transfer and pressure drop of air flow in tubes equipped with edgefold twisted tape (ETT) inserts (as seen in Fig. 2.2) and classical twisted tape inserts. The authors performed isothermal computational simulations using the FLUENT software. The solutions were completed with the RNG k-epsilon turbulence model for a range of Reynolds numbers ($2.5x10^3$-$9.5x10^3$) and twist ratios (5.4-11.4). The authors saw an increased thermal performance at a significant pressure drop penalty. They determined that the ETT inserts led to a 3.9-9.2% increase in the Nusselt number along with an 8.7-74% higher pressure drop compared to the classical twisted tapes [31].

Yadav and Padalkar also investigated air flow with modified twisted tapes. Their work focused on the heat transfer enhancement characteristics of flow in a circular tube with a partially decaying and partially swirling flow. This was investigated through four configurations of twisted tape inserts included the half-length upstream twisted tape, the half-length downstream twisted tape, the full-length twisted tape, and the plain tube. The

authors modeled air flow in an electrically heated tube using the FLUENT software. The k-epsilon turbulence model was employed, and solutions were completed for two uniform heat fluxes (2.3, 6.2 kW/m$^2$), various twist ratios (2.63, 3.70, 7.14), and a range of Reynolds numbers ($2.5x10^4$-$1.1x10^5$). The authors found that the modified configurations led to an increased heat transfer over the plain tube. However, this heat transfer enhancement was not as great as the full-length (or classical) twisted tape insert. The modified twisted tape inserts resulted in a lower pressure drop penalty than the classical twisted tape, and thus, the authors concluded that the modified configurations could be used to increase the thermal performance over that seen in plain tubes, while providing a lower pressure drop penalty than the classical twisted tape inserts [35].

### *Motivation for Current Study*

As seen in the literature, computational twisted tape studies often present the local flow information such as the velocity or temperature contours. However, the main focus of these studies is generally rooted in determining the thermal-hydraulic correlations. To this author's knowledge, no computational studies have focused on connecting the thermal-hydraulic performance to the local flow features of turbulent swirl flow. Drawing these connections could provide insight into the associated enhancement phenomena, which would help to inform the design of twisted tape devices.

As illustrated in Table 2.1, a review of the computational literature reveals no apparent consensus concerning the choice of turbulence model for twisted tape induced swirl flow. Many papers simply state the turbulence model used in the study while few papers investigate various options. To this author's knowledge, the most in-depth sweep of turbulence models was performed in the validation study of Eiamsa-ard et al. [29]. The validation was performed for isothermal conditions at Reynolds numbers ranging from $3x10^3$-$1x10^4$. The Nusselt number and friction factor were compared with the well-established correlations of Manglik and Bergles [15]. The authors determined that the shear stress transport turbulence model had the best performance, which goes against the model selected by a majority of studies as seen in Table 2.1. However, a few inconsistencies

in the study should be highlighted. Eiamsa-ard et al. appear to calculate the Darcy (or Moody) friction factor rather than the Fanning friction factor for their comparison. Manglik and Bergles developed correlations for the Fanning friction factor, which is defined as one-fourth of the Darcy friction factor [36]. It is unclear whether this is reflected in the data. Additionally, the range of Reynolds numbers investigated is suspect. Manglik and Bergles suggest that turbulent swirl flow exists at Reynolds numbers greater than $1x10^4$ [15]. However, Eiamsa-ard et al. investigated Reynolds numbers less than that. Considering the inconsistencies in this study and across the range of computational studies, it is important to perform an investigation into the variability across multiple turbulence models for twisted tape induced swirl flow.

Table 2.1: Variety of twisted tape (TT) geometries and turbulence models in the computational literature

| Authors | Application | Turbulence Model |
|---|---|---|
| **Date [25]** | Classic TT | k-epsilon |
| **Eiamsa-ard et al.* [29]** | Loose-fit TT | Shear stress transport |
| **Rahimi et al. [28]** | Modified TT | RNG k-epsilon |
| **Cui and Tian** [31]** | Edgefold TT | RNG k-epsilon |
| **Oni and Paul [34]** | Triangular cut TT | RNG k-epsilon |
| **Yadav and Paldalkar** [35]** | Half-length upstream; Half-length downstream | k-epsilon |
| **Lei et al. [32]** | Staggered TT with central holes | RNG k-epsilon |
| **Liu and Bai* [30]** | Short TT at inlet | Reynolds stress model |

*Authors compared at least two turbulence models
**Study performed with a working fluid of air

# Chapter 3: Overview of the Computational Approach

As outlined in Chapter 1, this research focuses on utilizing a computational approach to investigate the turbulent swirl flow induced by twisted tape inserts. Single-phase computational fluid dynamics (CFD) modeling was performed to investigate the thermal-hydraulic performance and local flow features of water-cooled twisted tape devices. The solutions were completed with the multiphysics commercial software ANSYS CFX, which can be used to model fluid flow, heat, and mass transfer for a wide range of flow fields. A detailed description of the solver capabilities can be found in Ref. [37].

In general, CFD is a tool that has been developed to solve fluid problems that may or may not include heat transfer. CFD is a well-established method for the solution and analysis of single-phase flow problems, and it can be utilized to solve problems from an array of applications such as combustion, aerodynamics, building ventilation, and electronics cooling, to name a few [38].

Because of the established nature of CFD solutions, the typical methodology and approaches are well-documented in the literature [33, 39, 40]. Only a brief overview of CFD methods will be presented in this chapter.

## 3.1. Governing Equations

CFD is used to investigate fluid and heat transfer problems by solving the governing equations over a particular region of interest. The underlying equations governing viscous flow have been known for over a century. However, the relations are considered to be complex and difficult to solve [39]**.** CFD solvers (including ANSYS CFX) help to discretize the flow field and solve the governing equations numerically.

Viscous flow is governed by the conservation of mass, momentum, and energy equations. The Navier-Stokes equations are often cited as the primary governing equations for viscous flow. Navier-Stokes is a vector equation derived by applying conservation of momentum to a fluid element. While Navier-Stokes really represents the conservation of

momentum, the name is sometimes used to refer to all of the governing equations as seen in the ANSYS CFX help guides [41, 42].

Only a brief summary of the governing equations will be provided here. A detailed derivation of the governing equations for viscous flow can be found in Ref. [39]. The conservation of mass (continuity), momentum (Navier-Stokes), and energy equations for an incompressible flow are summarized as follows [39]:

$$\vec{\nabla} \cdot \vec{V} = 0 \tag{3.1}$$

$$\rho \frac{D\vec{V}}{Dt} = \rho \vec{g} + \vec{\nabla} \cdot \tau'_{ij} - \vec{\nabla} P \tag{3.2}$$

$$\tau'_{ij} = \mu \left( \frac{\partial u_i}{\partial x_j} + \frac{\partial u_j}{\partial x_i} \right) + \delta_{ij} \lambda \vec{\nabla} \cdot \vec{V} \tag{3.3}$$

$$\rho \frac{Dh}{Dt} = \frac{DP}{Dt} + \vec{\nabla} \cdot \left( k \vec{\nabla} T \right) + \tau'_{ij} \frac{\partial u_i}{\partial x_j} \tag{3.4}$$

where P is the pressure, T is the temperature, $\vec{V}$ is the velocity vector, $\tau_{ij}$ is the stress tensor, $\delta_{ij}$ is the Kronecker delta function, and $\lambda$ is the coefficient of bulk viscosity. The governing equations are also a function of thermodynamic properties such as the density ($\rho$), dynamic viscosity ($\mu$), enthalpy (h), and thermal conductivity (k). Conservation of mass, momentum, and energy are represented by Equations 3.1, 3.2 and 3.3, and 3.4, respectively.

## 3.2. Turbulence Modeling

The swirling flows investigated in this work are in the turbulent regime, and thus, turbulence modeling must be implemented for the solution. A brief description of turbulence modeling will be discussed in this section. For more information, the reader is referred to the detailed discussions of Ref. [43, 44].

Turbulence is characterized by temporal and spatial fluctuations in the flow field. In order to predict turbulence, a great amount of research has been devoted to developing turbulence models. The most common approach to turbulence modeling involves the time-

averaging of fluctuating quantities as introduced by Reynolds in the early 19th century [44]. This process results in the Reynolds Averaged Navier-Stokes (RANS) equations, which represent the mean flow quantities. This approach reduces the computational effort needed to resolve turbulent flow. However, the averaging process results in extra unknowns, called Reynolds stresses, without introducing any additional equations. At the end of the averaging process, the number of unknowns outweigh the number of governing equations, thus the system is cannot be considered "closed." Ultimately, the goal of turbulence modeling is to utilize approximations for the unknowns. By doing so, the system can be closed [42, 44].

The most widely used approach for turbulence modeling involves the Boussinesq eddy viscosity approximation, which states that the Reynolds stress tensor is proportional to the mean strain rate as follows

$$\tau_{ij} = 2\mu_t S_{ij} - \frac{2}{3}\rho k \delta_{ij} \tag{3.5}$$

where $\mu_t$ is the eddy viscosity [45]. Turbulence models that implement the Boussinesq approximation are known as "eddy viscosity models." There are various types of eddy viscosity models, but the most popular subset consists of the two equation models. Two equation models are "very widely used, as they offer a good compromise between numerical effort and computational accuracy" [42]. The k-epsilon and k-omega models represent commonly used two equation models. These models mainly differ in the approximation of the eddy viscosity ($\mu_t$). For k-epsilon based models, the eddy viscosity is assumed to be a function of the turbulent kinetic energy ("k") and the turbulent dissipation ("epsilon"). On the other hand, k-omega based models assume that the eddy viscosity is linked to the turbulent kinetic energy and the turbulent frequency ("omega").

Another approach to turbulence modeling is implemented with Reynolds stress models. Rather than invoke the Boussinesq approximation, these models solve directly for the Reynolds stresses in the fluid. This approach inherently captures the anisotropies in the stress, which can make the models more suited to complex flows [42].

## 3.3. Selection of Turbulence Models

As suggested in Table 2.1, two equation eddy viscosity models, such as the k-epsilon or k-omega based models, are commonly chosen for computational twisted tape studies. However, it has been suggested that two equation eddy viscosity models are generally insensitive to streamline curvature and swirling flows [37, 42]. To combat this, investigators suggest the use of the more complex Reynolds Stress models (RSM) [46]. While RSM have been shown to perform better than two equation models in turbulent swirling flow, it has been suggested that their performance gains do not outweigh the associated complexity and computational cost increase [37]. Due to the increased complexity and computational cost involved with RSM, this study will focus on the more widely used two equation models. An alternative suggestion for sensitizing two equation models to streamline curvature is the addition of curvature correction terms to the simulation. To this author's knowledge, the use of curvature correction as developed by Spalart and Shur has not been utilized in the current computational twisted tape literature [47].

The initial computational investigations (as discussed in Chapter 4) were performed using the standard k-epsilon, shear stress transport, and renormalized group k-epsilon models. The curvature correction method was also employed to sensitize the standard models to streamline curvature and system rotation [37, 42]. Specific details on the implementation of these models in ANSYS CFX can be found in Ref. [42].

### *3.3.1. The Standard k-epsilon Model*

The standard k-epsilon model (k-eps) is one of the "most prominent" turbulence models in the CFD community, and it is often considered to be the industry standard. This model has been shown to be numerically robust with a well-established regime of predictive capability. In general, this model provides a good compromise between accuracy and robustness [37]. As implemented in CFX, the k-eps model uses a "scalable wall function" approach. With this approach, arbitrarily fine meshes are ignored in the solution to increase robustness [42].

While the k-eps model is considered an industry standard, there are still some applications where the model may not be suitable. Some of these include flows with boundary layer separation, sudden changes in the mean strain rate, rotating fluids, or flows over curved surfaces. At first glance, this would suggest the k-eps model is not well-suited for twisted tape induced swirl flow. However, as seen in Table 2.1, k-epsilon based models are some of the most commonly used in the swirl flow literature.

### *3.3.2. The Renormalized Group k-epsilon Model*

The renormalized group k-epsilon (RNG k-eps) model is an alternative to the standard k-epsilon model. It was derived from the instantaneous Navier-Stokes equations using a statistical technique called the renormalization group theory [33]. The equations for RNG k-eps are the same as those used for the k-eps model. The difference between the two lies in the constants used in the models. The CFX guidelines suggest that the RNG k-eps model offers "little improvement" over the standard k-epsilon model [37]. However, the RNG k-epsilon is widely used in the twisted tape swirl flow literature. It has been included in this study because of its popularity within the community.

### *3.3.3. The Shear Stress Transport Model*

The shear stress transport (SST) model was developed by Menter [48] to give "highly accurate predictions" for flow separation [37]. The SST model was developed to improve upon the Wilcox k-omega and the Menter k-omega baseline (BSL) model. The BSL model utilizes the k-omega model in the inner boundary layer region and switches to the standard k-epsilon model in the outer boundary layer region and in free shear flows [48].

The SST model is recommended by ANSYS CFX for high accuracy boundary layer simulations. In order to fully realize the benefits of this model, the mesh must include ten or more points in the boundary layer, which requires a higher mesh resolution compared to the k-epsilon based models. This model does not frequently appear in the computational twisted tape swirl flow literature. It has been included in this study because of its ability to

model the flow near the wall, and it is presumed to be more accurate for the thermal-hydraulics problems investigated.

### *3.3.4. The Curvature Correction Method*

One criticism of eddy viscosity models is their inherent lack of sensitivity to streamline curvature and system rotation—both of which play a large role in this work. Reynolds stress models naturally include these effects, but their increased complexity and computational cost prevented them from implementation in this research. An alternative approach to including streamline curvature and system rotation effects in the turbulence modeling was developed by Spalart and Shur [47]. They developed the curvature correction (CC) method, which modifies the production term in two equation eddy viscosity models. For further details on the model and its implementation in CFX, the reader is referred to the comprehensive discussions in Ref. [42, 47, 49]. To this author's knowledge, the CC method has not been utilized in the current computational twisted tape literature. It will be implemented to determine if the method improves the solution for twisted tape induced swirl flow.

## 3.4. Modeling in the Near Wall Region

### *3.4.1. Description of the Near Wall Region*

Another critical topic is the near wall treatment in the CFD solution. When considering turbulent flow, the near wall region can be divided into three layers consisting of an inner layer, an outer layer, and an overlap layer connecting them. Viscous shear dominates the inner layer, while turbulent shear dominates the outer layer. In the overlap layer, both types of shear play an important role, and the profile smoothly connects the inner and outer regions [39, 50].

The well-known "law of the wall" is used to describe the relationship between the dimensionless velocity ($u^+$) profile in the inner layer [39, 44, 50]. Note that there is an analogous law of the wall concerned with the non-dimensional temperature ($T^+$) profile in the near wall region [39]. The inner layer rises from the no-slip condition at the wall to

smoothly connect with the overlap layer at a dimensionless wall coordinate of $y^+ \approx 30$. Within this inner layer, the turbulence is damped out very close to the wall ($y^+ \leq 5$), and the boundary layer is dominated by viscous shear. The velocity profile is linear in this very small region close to the wall such that

$$u^+ = y^+ \tag{3.6}$$

This small region is known as the "viscous sublayer." Moving away from the wall, the velocity profile is neither linear nor logarithmic but is a merge between the two. This region is known as the "buffer layer" ($5 \leq y^+ \leq 30$) [39].

The overlap layer follows the buffer layer. It is also known as the "log layer" or "log wall region," and in this layer, the flow is considered to be fully turbulent [44, 51]. The non-dimensional velocity profile is described in this region by the log law such that

$$u^+ = \frac{1}{\kappa} \ln y^+ + C \tag{3.7}$$

where κ is Kármán's constant (≈0.41) and C is a dimensionless integration constant (≈5.0) [44].

The outer layer follows and is dominated by turbulent shear. It can also be referred to as the "defect" layer and is described by the "velocity-defect law," where defect refers to retardation in the flow due to wall effects [39, 44]. The outer layer was determined to be independent of molecular viscosity and dependent upon on the boundary layer thickness and the local pressure gradient [39, 50].

### *3.4.2. Turbulence Modeling Near the Wall*

Two approaches are commonly utilized to model flow near the wall. The first uses wall functions to impose suitable conditions in the near wall region without resolving the boundary layer. All turbulence models implemented in CFX are suitable for the wall function method. The second approach, known as a "low Reynolds number" or "low Re" method, resolves the boundary layer near the wall through implementation of a refined

mesh in that region. This method is suitable for turbulence models based on the turbulent frequency (or "omega"), such as the SST model. Note that the low Re method is not constrained to low Reynolds number flows. Instead, the term "low Re" refers to the turbulent Reynolds number, which is low in the near wall region [37]. The resolution of the flow field down to the wall necessitates a very fine mesh, which greatly increases the computation time compared to the wall function approach.

Different near wall treatments are used for different turbulence models in ANSYS CFX. So-called "scalable wall functions" are utilized for all turbulence models based on the turbulent dissipation (or "epsilon") such as k-eps and RNG k-eps. With this approach, arbitrarily fine meshes are ignored in the solution to increase robustness [42]. For omega based models (including SST), an "automatic near wall treatment" method is applied. The automatic near wall treatment was developed to reduce resolution requirements for the low Re approach. It allows for a gradual transition between wall functions to a low Re formulation near the wall where the mesh is refined enough [37]. A brief discussion of these near wall treatments will be included in the following sections. Detailed explanations of the methods can be found in Ref. [37, 42].

### *Scalable Wall Functions in CFX*

In general, the implementation of a turbulence model with the wall function approach is meant to be valid for the "fully turbulent region away from any viscosity-dominated near-walls" [White viscous flow]. Wall functions implement the log law as the constitutive relationship between the velocity and the surface shear stress. Thus, at the first mesh point away from the wall, the near wall velocity can be determined by Eq. 3.7 [44].

As discussed in Ref. [42], this is the method utilized for wall functions in ANSYS CFX. The log law is used to connect the wall conditions to the variables at the near wall mesh node, which is presumed to fall in the fully turbulent boundary layer region. The dimensionless velocity in the log law region is a function of the dimensionless wall distance such that

$$u^+ = \frac{u}{v^*} \tag{3.8}$$

$$y^+ = \frac{\rho \Delta y v^*}{\mu} \tag{3.9}$$

$$v^* = \sqrt{\tau_w / \rho} \tag{3.10}$$

where u is the axial velocity, v* is the friction velocity, Δy is the distance from the wall, $\tau_w$ is the wall shear stress, ρ is the density, and μ is the dynamic viscosity.

As discussed in Ref. [40, 42], one issue with the traditional wall function formulation is that it becomes singular as the axial velocity approaches zero. Another formulation was proposed to address the issue where the friction velocity was replaced with an alternative velocity scale ($u^*$) such that

$$u^* = C_\mu^{1/4} k^{1/2} \tag{3.11}$$

$$v^* = \frac{u}{\frac{1}{\kappa} \ln y^* + C} \tag{3.12}$$

$$\tau_w = \rho u^* v^* \tag{3.13}$$

$$y^* = \frac{\rho u^* \Delta y}{\mu} \tag{3.14}$$

which leads to altered equations for the friction velocity, wall shear stress, and the alternate non-dimensional wall distance ($y^*$) as shown in Eq. 3.12, 3.13, and 3.14, respectively [42].

One major drawback to the standard wall function approach is the dependence on the location of the first mesh point away from the wall and a sensitivity to near wall meshing [40, 42]. The so-called scalable wall function formulation was developed in ANSYS CFX to overcome inconsistencies with the approach due to refined meshes, and it can be applied to arbitrarily fine meshes.

The scalable wall function approach avoids issues due to meshes with points in the viscous sublayer, where the log law is not valid [40]. Essentially, the formulation sets a floor on the non-dimensional wall distance such that $\tilde{y}^* = \max(y^*, y^*_{lim})$. The limit, or the floor, is set to $y^*_{lim} = 11.06$. Thus, the calculated non-dimensional wall distance ($\tilde{y}^*$) is not allowed to fall below the limit, and all mesh points are outside of the viscous sublayer

thereby avoiding inconsistencies due to a refined mesh [42]. This method is the default approach utilized for wall function treatment in ANSYS CFX.

### *Automatic Near Wall Treatment in CFX*

One drawback of the traditional low Re approach is the requirement of a very refined near wall mesh resolution ($y^+<2$). While this provides an accurate simulation of the near wall region, it greatly increases computational costs. Furthermore, such a high fidelity mesh in the entire near wall region cannot be guaranteed for most applications [37].

The automatic near wall treatment can be implemented in CFX for k-omega based models. Essentially, this method switches from a low Re formulation where the mesh is fine enough to resolve the viscous sublayer to a wall function approach where the mesh is not as fine. This allows for a consistent mesh refinement from coarse meshes that do not resolve the viscous sublayer to fine meshes that do [40, 42]. To take full advantage of the automatic wall treatment, the ANSYS guides suggest the use of at least 10 nodes in the boundary layer [37]. The specific details of the automatic near wall treatment can be found in Ref. [42].

### *Temperature in the Near Wall Region*

The previous sections focused on the velocity treatment in the near wall region in ANSYS CFX. For simulations including heat transfer, the heat flux and dimensionless temperature can also be modeled with the use of the scalable wall function or automatic near wall treatment methods.

The dimensionless near wall temperature profile follows a universal profile from the viscous sublayer through the logarithmic region such that

$$T^+ = \frac{T_w - T}{T^*} \tag{3.15}$$

$$T^* = \frac{q''_w}{\rho c_p \nu^*} \tag{3.16}$$

where $T_w$ is the temperature at the wall, $c_p$ is the specific heat capacity, and $q''_w$ is the heat flux at the wall [39, 42].

For scalable wall functions in ANSYS CFX, the non-dimensional temperature profile follows the log law relationship such that

$$T^+ = 2.12 \ln y^* + \beta \tag{3.17}$$

$$\beta = \left(3.85 Pr^{1/3} - 1.3\right)^2 + 2.12 \ln Pr \tag{3.18}$$

where Pr is the Prandtl number of the fluid [42].

For the automatic near wall treatment method, the dimensionless temperature is modeled using the "thermal law-of-the-wall" function created by Kader [52]. The non-dimensional temperature profile is determined by blending the viscous sublayer and the logarithmic law of the wall such that [42]

$$T^+ = Pry^* e^{-\Gamma} + [2.12 \ln y^* + \beta] e^{-1/\Gamma} \tag{3.19}$$

$$\Gamma = \frac{0.01(Pry^*)^4}{1+5Pr^3 y^*} \tag{3.20}$$

Both near wall treatments will be utilized in this work for thermal-hydraulics simulations. The epsilon based models (k-eps and RNG k-eps) will implement the scalable wall function method, while the omega based model (SST) will utilize the automatic near wall treatment approach. A brief investigation into the near wall behavior is discussed in Chapter 6.

# Chapter 4: Computational Investigation for a Tube Equipped with a Twisted Tape

*Portions of this work have been published in the following peer-reviewed manuscript in which the author performed all analysis:*

*E. Clark, A. Lumsdaine, K. Ekici, and A. E. Ruggles, "Computational Investigation of the Thermal-Hydraulic Performance for Twisted Tape Enabled High Heat Flux Components," Accepted for Publication in Fusion Science and Technology, 2017.*

This chapter will discuss a computational investigation performed for a general geometry including a tube equipped with a twisted tape insert. There were two main goals for this study. The first was to investigate the capability of the ANSYS CFX software to solve the twisted tape induced flow field, and the second was to take advantage of the computational nature of this work by analyzing the local flow information. Following those goals, the results are partitioned into two main sections: the computational validation and an investigation the local flow field. Furthermore, the investigation was performed for both adiabatic and diabatic conditions. For validation purposes, the diabatic heating conditions were chosen to be moderate and uniform.

## 4.1. Computational Models

### *4.1.1. Adiabatic Investigation*

#### *Adiabatic Model Geometry*

In this chapter, the computational model was developed to mimic the experiments of Manglik and Bergles, which were the basis for their well-accepted and commonly cited twisted tape correlations for turbulent swirl flow [15, 19]. Only the water and the twisted tape were simulated in this initial study. Thus, no tube was included in the model. As seen in Figure 4.1, the geometry consists of a straight entrance and exit region ($L_{ent}$ and $L_{exit}$, respectively) with a swirling region ($L_{swirl}$) in between the two plain tube sections.

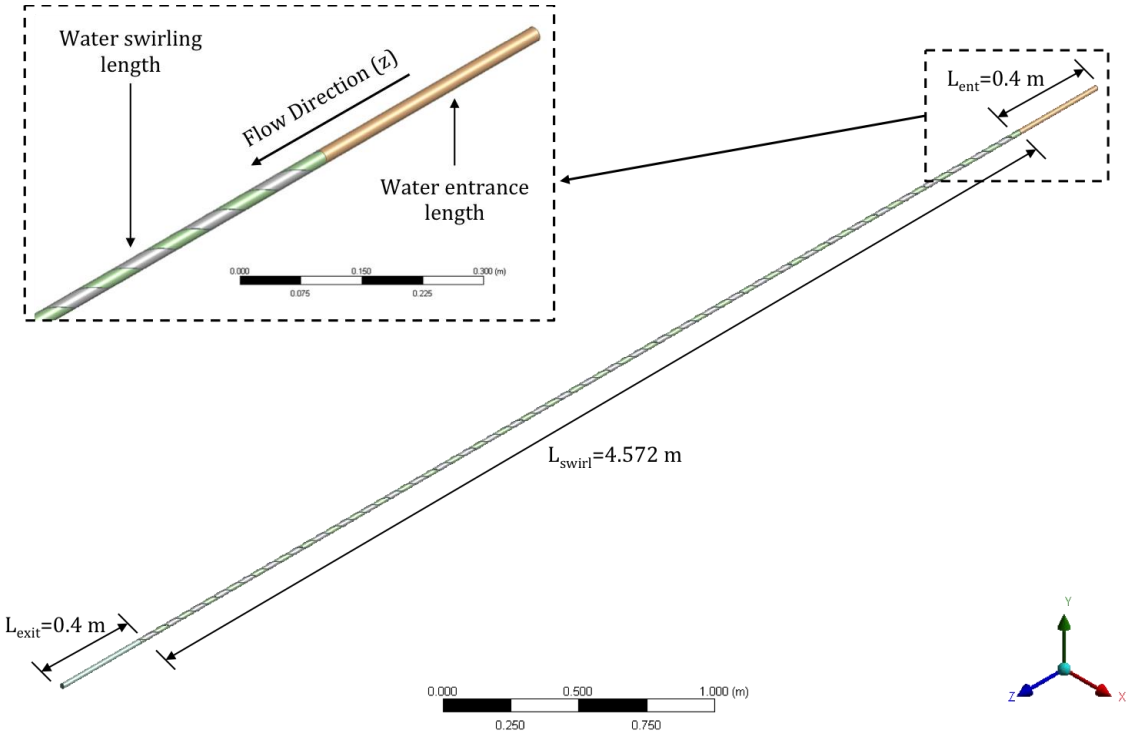


Figure 4.1: Adiabatic validation model geometry

The swirling region consists of two water parts, which are separated by a twisted tape. The entrance and exit regions were chosen to be 0.4 m in length, while the length of the swirling region was set to match the experiments at 4.572 m. A closer view of the entrance and swirling regions can be seen in Figure 4.1 along with the flow direction. Following the Manglik and Bergles experiments, the axial diameter of the model is 0.02118 m. The twisted tape is characterized by a width ($\delta$) of $4.826 \times 10^{-4}$ m and a twist ratio y=3.

### *Adiabatic Conditions*

The adiabatic investigation was performed for various Reynolds numbers for the turbulence models discussed in Chapter 3 (k-eps, RNG k-eps, and SST). A typical mesh study was performed for the standard turbulence models investigated. Inflation layers were implemented on the water-solid interfaces and were set by a first layer thickness, maximum number of layers, and a growth rate. The first layer height was adjusted to give an appropriate non-dimensional wall coordinate ($y^+$), and the freestream mesh was refined until the pressure drop changed less than 1% from case to case. Convergence was evaluated with three criteria: (1) residuals reached an acceptable level, (2) imbalances were less than 1%, and (3) pressure drop monitor point reached a steady value. The final meshes varied for each Reynolds number investigated. The final mesh for k-epsilon based models had an average non-dimensional wall coordinate of $y^+ \approx 17\text{-}32$ with a mesh count ranging from approximately 0.4–1.6 million elements. The SST model required a finer mesh to resolve the flow field close to the wall. The final mesh for the SST model had an average non-dimensional wall coordinate of $y^+ < 1$ and a mesh count ranging from approximately 3-7.2 million elements. The curvature correction method was implemented with a coefficient in ANSYS CFX using the final mesh obtained for the standard turbulence models [37, 42]. Unfortunately, the ANSYS guides do not provide much detail about the preferred value of the CC coefficient. The default value is 1, and a value greater than that should increase the curvature scaling factor. The CC solutions were started with the default coefficient, and the coefficient was then increased at each successive run until there was minimal impact on the solution.

In total, eighteen cases were considered for the adiabatic investigation. Each case was simulated using a steady solver in ANSYS CFX. The inlet temperature and outlet pressure were set to 20°C and 1 atm, respectively. Three Reynolds numbers were chosen to create turbulent swirl flow in the model: $1x10^4$, $8x10^4$, and $1.5x10^5$. The corresponding inlet axial velocities are 0.474, 3.790, 7.106 m/s. These Reynolds numbers were chosen for a variety of reasons [11]. First, the Reynolds numbers represent a wide range of turbulent conditions that extend the conditions often investigated in the twisted tape swirl flow literature. The medium and higher values are much higher than those typically seen in the computational literature for single-phase twisted tape induced swirl flow, where it is common to investigate flows at an order of magnitude lower than those chosen for this study [29, 34]. Thus, the selected range of Reynolds numbers will expand the knowledge base of turbulent twisted tape induced swirl flow behavior at higher flow rates. Furthermore, this range of Reynolds numbers bounds the expected flow value for a W7-X twisted tape enabled device. Boscary et al. provided expected flow parameters for a W7-X PFC prototype, where the inlet velocity is 12 m/s (including the tape) and the empty tube diameter is 12 mm [53]. For flow at 20°C and 1 MPa, this results in a Reynolds number of approximately $1.25x10^5$. Furthermore, these Reynolds numbers are relevant to the range of values seen for some ITER relevant experiments such as Araki et al. The authors investigated the flow for an empty tube diameter of 10 mm at a range of inlet velocities (4.2-16 m/s), inlet temperatures (20-80°C), and pressures (0.5-1.3 MPa) [20]. These flow parameters result in Reynolds numbers ranging from $4.2x10^4$ to $4.4x10^5$.

### *4.1.2. Diabatic Investigation*

#### *Diabatic Model Geometry*

Initially, the diabatic investigation was performed on a slightly altered model from the one discussed in the previous section. The exit region was removed from the geometry to improve convergence, but a similar approach was taken with the model. As discussed in Clark et al., only the water and the twisted tape were modeled initially (i.e. no pipe included) [11].

This initial model resulted in the key features noted in the adiabatic solutions. However, it was determined that the diabatic model would be more representative of the physical situation with the inclusion of a pipe in the geometry. In an experimental setting, the heat flux would be applied all around the outside of the tube, including the part adjacent to the twisted tape. By excluding the heat addition along the tape, a portion of the heat flux was neglected in the model. The addition of the tube resulted in a few differences in the solution. It led to a higher, non-uniform heat flux from the tube to the water, which was due to the smaller surface area on the water-tube interface than the outside of the tube. This alteration yielded a more realistic heat flux applied to the water. With the addition of the tube, the heat flowed into the corners created by the tape-tube interface as opposed to the corners being set to a certain applied heat flux, and the total power applied to the outside of the tube was transferred to the water. The tube thickness was set to match that of the Manglik and Bergles experiments, which led to an outer tube diameter of 0.0254 m. The inside tube diameter, twist ratio, and tape thickness were unchanged from that discussed in the previous section.

### *Diabatic Conditions*

For the diabatic investigation, the swirling region in the geometry consisted of a "calming length" ($L_C$) of 1.524 m, and the rest of the length was the "heated section" ($L_H$) as shown in Figure 4.2. Figure 4.2 also shows the uniform, constant heat flux that was applied to the outside of the tube in the "heated section." The inlet temperature and exit pressure were set to 20°C and 1 atm, respectively. Heat transfer was modeled from the tube to the water, throughout the water, and at the water-tape interfaces. The tape-tube interfaces were considered to be adiabatic, and radiation effects were not considered.

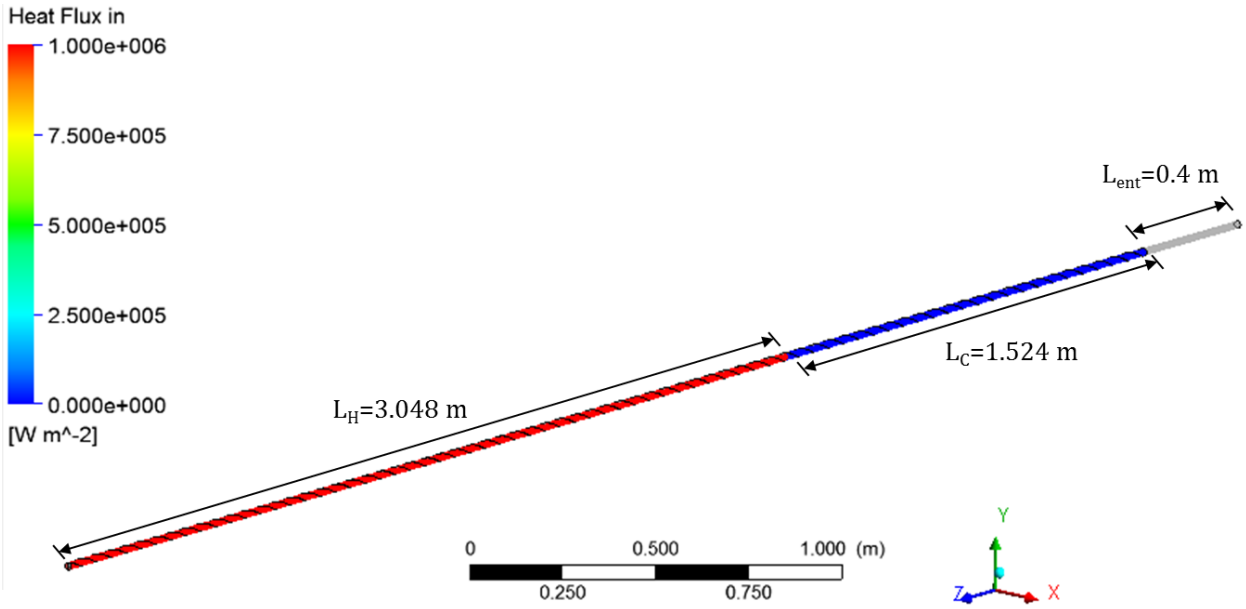


Figure 4.2: Applied heat flux of 1 MW/m$^2$ where $L_H$ is the heated section, $L_C$ is the calming section, and $L_{ent}$ is the straight entrance region [11]

The water properties were implemented as temperature and pressure dependent according to the International Association for the Properties of Water and Steam Industrial Formulation 1997 (IAPWS-IF97) [54]. The twisted tape and tube were modeled with constant properties as yellow brass and a copper-nickel alloy (Cu-Ni 70-30 (SB111)), respectively [19]. The analysis was performed for two moderate heat fluxes and two turbulent Reynolds numbers resulting in a total of four cases as seen in Table 4.1.

The Reynolds numbers in Table 4.1 were chosen as discussed in Section 4.1.1. The lowest Reynolds number ($Re=1x10^4$) was removed for this study because it is much lower than what could be expected for fusion or plasma physics experiments. As seen in Table 4.1, two moderate heat fluxes were chosen for this initial investigation. Moderate heat fluxes were selected to keep the flow in the single-phase regime. As discussed in Chapter 1, the aim of this study is to further the understanding of the local flow features in single-phase turbulent swirl flow before including the complexity of the two-phase model. The global parameters in this study will be compared to the Manglik and Bergles and other legacy twisted tape design correlations [14-17]. Because these correlations were developed for single-phase flow, it was important to select moderate heat fluxes rather than the high heat fluxes typically seen in fusion relevant applications.

Table 4.1: Diabatic cases investigated

| | **Case 1** | **Case 2** | **Case 3** | **Case 4** |
|---|---|---|---|---|
| **Heat flux [MW/m$^2$]** | 0.5 | 1 | 0.5 | 1 |
| **Inlet Reynolds number** | $8x10^4$ | $8x10^4$ | $1.5x10^5$ | $1.5x10^5$ |
| **Inlet axial velocity [m/s]** | 3.79 | 3.79 | 7.11 | 7.11 |

Simulations for the four cases were completed for the same turbulence models discussed in Section 4.1.1, which resulted in a total of 24 sets of results. The approach to the mesh study was adopted from the adiabatic investigation, and it was completed before the tube was added to the diabatic model. A typical mesh study was performed for the standard turbulence models (k-eps, RNG k-eps, and SST). Inflation layers were implemented on the water-solid interfaces and were set by a first layer thickness, maximum number of layers, and a growth rate. The first layer height was adjusted to give an appropriate non-dimensional wall coordinate ($y^+$), and the freestream mesh was refined successively until the pressure drop, mean temperature near the outlet, and mean surface temperature near the outlet changed less than 2% from case to case. Convergence was evaluated with three criteria: (1) residuals reached an acceptable level, (2) imbalances were less than 1%, and (3) all monitor points reached a steady value. For the diabatic cases, monitor points were set for the pressure drop, average outlet temperature, and maximum outlet temperature. The final meshes varied for each Reynolds number investigated. The final mesh for k-epsilon based models had an average non-dimensional wall coordinate of $y^+ \approx 31\text{-}44$ with a mesh count ranging from approximately 0.8–1.6 million elements. The SST model required a finer mesh to resolve the flow field close to the wall. The final mesh for the SST model had an average non-dimensional wall coordinate of $y^+ \approx 0.9\text{-}1.3$ and a mesh count ranging from approximately 4.9-7.9 million elements. The curvature correction method was implemented for this study as well. The CC solutions were started with the default coefficient of 1, and the coefficient was then increased at each successive run until there was minimal impact on the solution. As noted above, this initial mesh study was performed for each case prior to adding the tube to the model. The addition of the tube did not necessitate a whole new mesh study for the 24 cases. The simulations were performed with the final mesh from the initial study. The addition of the tube increased the element sizes for the mesh but did not significantly alter the non-dimensional wall coordinates.

## 4.2. Computational Validation

The computational validation was performed to investigate the capability of the ANSYS CFX software to solve the twisted tape flow field to an acceptable level of predictive capability by comparing to results from the literature. However, there is limited experimental information available in the literature for validation purposes. This may be a significant factor behind the tendency for computational studies to focus on thermal-hydraulic correlations rather than local flow information. Many of those works validate against global parameters, then present the local flow information for their particular application of interest [29, 34]. A similar approach was adopted for this work. The computational validation mostly consists of comparisons of global parameters, such as the Fanning friction factor and Nusselt number, to legacy correlations. The exception to this involves comparisons to adiabatic flow visualization experiments performed by Smithberg and Landis and Seymour [22, 23]. A more in-depth discussion of the local flow information will follow the comparisons to the legacy works.

Furthermore, the validation study allowed for an investigation into the variability of results due to different turbulence models. The apparent lack of consensus in the literature as identified by Table 2.1 is a strong motivator for a detailed turbulence model sweep. The study included both adiabatic and diabatic analyses on a general twisted tape geometry. The global parameters are compared to the well-accepted and frequently cited turbulent twisted tape correlations of Manglik and Bergles as well as other legacy correlations [13-17, 22]. The adiabatic validation was performed for a range of Reynolds numbers over various turbulence models, and the diabatic validation, which was performed over a range of Reynolds numbers, heat fluxes, and turbulence models.

### *4.2.1. Adiabatic Validation*

#### *Calculations and Legacy Friction Factor Correlations*

The adiabatic results were compared to the legacy turbulent swirl correlations via the Fanning friction factor. The legacy correlations are shown in Table 4.2.

Table 4.2: Legacy Fanning friction factor correlations for isothermal conditions as cited in Ref. [8]

| Authors | $C_f$ Correlation |
|---|---|
| **Gambill and Bundy [13]** | $C_f = \frac{0.046}{Re^{0.2}}\left[\frac{\pi+2-2\delta/d}{\pi-4\delta/d}\right]^{1.8}\left[\frac{\pi}{\pi-4\delta/d}\right]^{1.2} + \frac{0.0525}{y^{1.31}}\left[\frac{2000}{Re}\right]^{0.81}\left[\frac{\pi+2-2\delta/d}{\pi-4\delta/d}\right]^{0.38}\left[\frac{\pi}{\pi-4\delta/d}\right]^{2.62}$ |
| **Lopina and Bergles [14]** | $C_f = \frac{0.1265}{y^{0.406}Re^{0.2}}\left[\frac{\pi+2-2\delta/d}{\pi-4\delta/d}\right]^{1.2}\left[\frac{\pi}{\pi-4\delta/d}\right]^{1.8}$ |
| **Manglik and Bergles [15]** | $C_f = \frac{0.0791}{Re^{0.25}}\left[1+\frac{2.752}{y^{1.29}}\right]\left[\frac{\pi+2-2\delta/d}{\pi-4\delta/d}\right]^{1.25}\left[\frac{\pi}{\pi-4\delta/d}\right]^{1.75}$ |
| **Ibragimov et al. [16]** | $C_f = \frac{0.0791}{Re^{0.25}}\left[1+\frac{14.375}{y^{4}}\right]\left[\frac{\pi+2-2\delta/d}{\pi-4\delta/d}\right]^{1.25}\left[\frac{\pi}{\pi-4\delta/d}\right]^{1.75}$ |
| **Seymour [22]** | $C_f = \frac{7.375}{y\sqrt{Re}}\left[\frac{\pi}{\pi-4\delta/d}\right]^{1.5} + \frac{23.75}{Re}\left[\frac{\pi}{\pi-4\delta/d}\right] + 0.00875\left[\frac{\pi}{\pi-4\delta/d}\right]^{2}$ |

As discussed by Manglik and Bergles, all parameters in the correlations are based on empty tube dimensions [15]. Thus, the Reynolds number was calculated as $Re = \rho u d/\mu$. The Fanning friction factor ($C_f$) was calculated for each case such that

$$C_f = \frac{\Delta P}{2\rho u_{in}^2 (L/d)} \tag{4.1}$$

where $\Delta P$ is the total pressure drop, $\rho$ is the density, $u_{in}$ is the inlet axial velocity, $L$ is the total length, and $d$ is the empty tube diameter.

## *Experimental Ranges of the Legacy Friction Factor Correlations*

The legacy correlations shown in Table 4.2 are based on experimental results, which range across various parameters. Table 4.3 summarizes some of the key hydraulic parameters behind the legacy correlations used in this comparison. The studies were performed across various ranges of Reynolds numbers, twist ratios, and fluids. A comparison of the selected Reynolds numbers ($1\text{x}10^4$, $8\text{x}10^4$, $1.5\text{x}10^5$) and Table 4.3 shows that the flow rates fall within some of the hydraulic ranges investigated in the legacy experiments.

Table 4.3: Experimental parameters for legacy friction factor correlations

| Study | Fluid | Re | y |
|---|---|---|---|
| **Gambill and Bundy [13, 55]*** | Water; Ethylene Glycol | $4x10^3 – 8x10^4$ | 2.3 – 12 |
| **Lopina and Bergles [14]** | Water | $8x10^3 – 1.3x10^5$ | 2.48 – 9.2 |
| **Manglik and Bergles [19]** | Water; Ethylene Glycol | $3x10^2 – 3.5x10^4$ | 3 – 6 |
| **Ibragimov et al. [16, 55]*** | Water | $1x10^4 – 5x10^4$ | 2.1 – ∞ |
| **Seymour [8, 22]** | Air | $1x10^3 – 2x10^5$ | 1.84 – ∞ |

* Reynolds numbers are based on the hydraulic diameter ($Re_h$) as cited in Ref. [55]. $Re_h$ for the adiabatic validation are approximately $6x10^3$, $5x10^4$, and $9x10^4$.

Note that some of the studies recorded Reynolds numbers based on the hydraulic diameter ($Re_h$). In order to compare to these studies, the $Re_h$ was calculated for the adiabatic validation. For the selected twist ratio, tape thickness, and Reynolds numbers of $1x10^4$, $8x10^4$, and $1.5x10^5$, the $Re_h$ is approximately $6x10^3$, $5x10^4$, and $9x10^4$, respectively. The lowest Reynolds number falls within the experimental ranges of each legacy correlation except Ibragimov et al., while the highest one only aligns with the Seymour experiments. The moderate Reynolds number falls within the experimental range of each legacy correlation except the Manglik and Bergles experiments. Furthermore, the twist ratio investigated in the adiabatic validation (y=3) falls within the ranges investigated in all of the legacy correlations.

### *Comparison of Adiabatic Global Parameters to Legacy Works*

Figure 4.3 shows the comparison between the simulated results and various friction factor correlations (as shown in Table 4.2) [13-16, 22]. This figure highlights the general trend of the friction factor due to a change in Reynolds number.

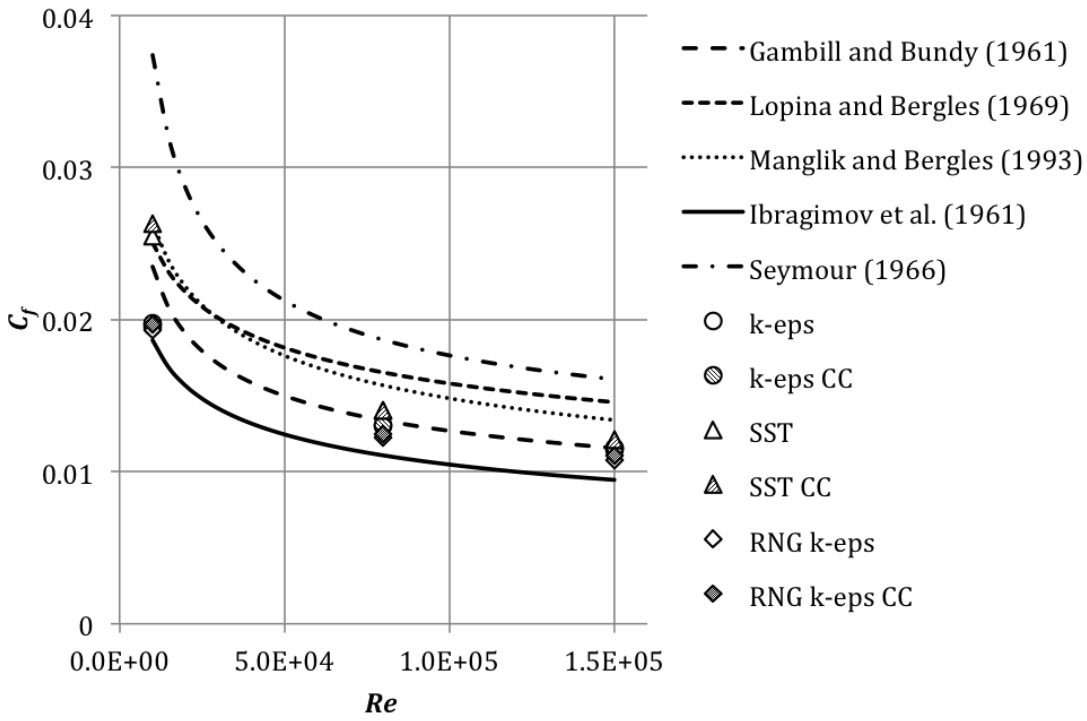


Figure 4.3: Fanning friction factor comparison of computational results and legacy correlations [13-16, 22]

As the Reynolds number increases, the friction factor decreases. Figure 4.3 also highlights the wide range of results from the legacy correlations. The simulated results show a wider scatter at the lower Reynolds number, while they cluster around the Gambill and Bundy correlations for the higher flow rates [13].

Figure 4.4 shows the comparison between the simulated results and the Manglik and Bergles correlation for the friction factor [15]. Again, the turbulence models yield a wider range of results at the lower Reynolds number. The SST model clearly outperforms the k-epsilon based models at the low Reynolds number. However, as the Reynolds number is increased, the performance gap between the various turbulence models closes. The SST models are slightly closer to the correlation followed by the k-epsilon model and then the RNG k-epsilon model. The curvature correction method also seems to have a bigger impact on the solution at lower Reynolds numbers, where the SST CC results match the Manglik and Bergles correlation. However, at larger Reynolds numbers, the addition of the curvature correction coefficient does not appear to have a significant impact on the solution. The variations revealed in this study will be further investigated with diabatic cases to see whether the addition of heat to the solution will impact the effects of utilizing various turbulence models.

### *Comparison to Adiabatic Flow Visualization Experiments*

The adiabatic local flow information was investigated to gain insight into the structure of the twisted tape swirl flow. As is common in the literature, the flow pattern can be determined by analysis of the velocity contours [22, 23]. However, only a few experimental studies investigated the flow structure of turbulent twisted tape induced swirl flow. Smithberg and Landis and Seymour performed adiabatic flow visualization studies using air as the working fluid. Smithberg and Landis performed their flow visualization with a Reynolds number of $1.4 \times 10^5$ and a twist ratio of 5.15 [23]. Seymour performed the adiabatic study with a Reynolds number of $6.2 \times 10^4$ and a twist ratio of 4.76 [22].

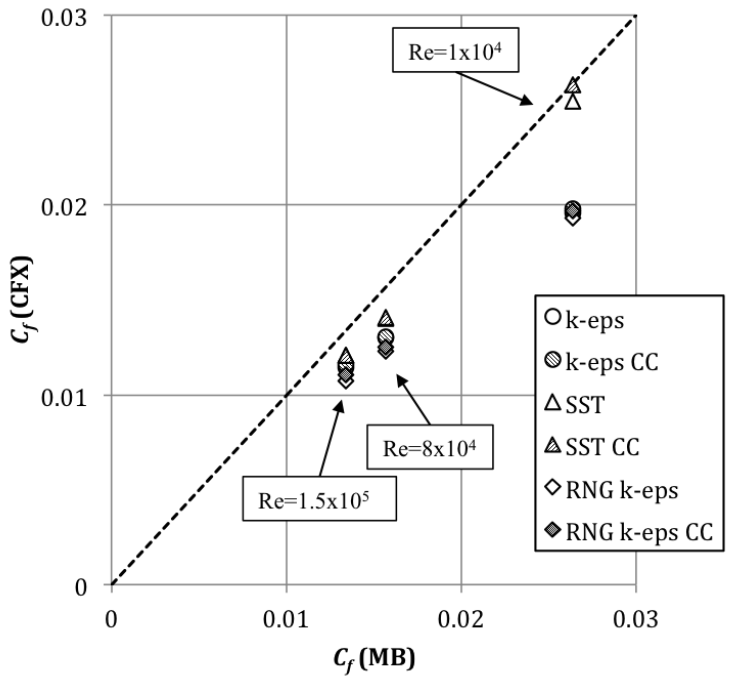


Figure 4.4: Adiabatic Fanning friction factor comparison of simulated results (CFX) and the Manglik and Bergles correlation (MB) [15]

For validation purposes, the velocity contours from the water-cooled solutions were initially qualitatively compared against the legacy flow patterns (as will be shown in Section 4.3.1). However, this was not a direct comparison because there was difference in the working fluids (water vs. air). Two air solutions were performed to compare to the legacy experiments using the adiabatic model discussed in Section 4.1.1. The k-epsilon turbulence model was used for both air solutions. The working fluid was changed from water to air at 25°C using the built-in material property library in ANSYS CFX. The twist ratio and Reynolds numbers were set to match the experiments. The Mach number (M) was investigated to determine if the air could be treated as an incompressible fluid. As suggested by Anderson [56], gas velocities less than about 0.3 times the speed of sound can be assumed to be incompressible. The Mach number was calculated for each case to check compressibility effects such that

$$M = \frac{u_{in}}{a} \tag{4.2}$$

where a is the speed of sound and $u_{in}$ is the inlet velocity. The speed of sound was calculated with the perfect gas law as follows

$$a = \sqrt{\gamma RT} \tag{4.3}$$

where γ is the ratio of the specific heat at constant pressure to the specific heat at constant volume ($c_p/c_v$), R is the universal gas constant, and T is the temperature. For standard air conditions, γ=1.4 and R=287 J/kgK. The validity of the perfect gas law for the speed of sound can be determined by the compressibility factor (Z) as shown in Eq. 4.4 [57]. If Z is close to unity, then the conditions are appropriate for the perfect gas law to be used.

$$Z = \frac{P}{\rho RT} \tag{4.4}$$

For air at 25°C and 1 atm, the compressibility factor was 0.999. This allowed for the use of Eq. 4.3 to determine the Mach number as shown in Eq. 4.2. The Mach numbers for the two cases were 0.13 and 0.3 for the Seymour [22] and Smithberg and Landis [23] conditions,

respectively. With the Mach numbers approximately less than 0.3, the working fluid was treated as incompressible.

Figures 4.5 and 4.6 show comparisons between the computational results and the flow patterns from the experiments. The axial velocity contours are compared to the axial velocity measurements from the experiments. In both cases, the experimental flow measurements have been flipped to match the swirl direction in the adiabatic model. When viewing the velocity contours, the flow is considered to be rotating counterclockwise and coming out of the page unless otherwise noted. As seen in Figures 4.5 and 4.6, the computational results are qualitatively similar to the experimental measurements. One key feature to note is the "inflow" region near the center of the tape, which was also noted in the legacy papers. This inflow region is indicative of the secondary circulation occurring in the fluid. The secondary motion causes a reinjection of the slow moving boundary layer fluid into the freestream. Smithberg and Landis suggest that this secondary circulation takes the form of a double vortex structure, which leads to "high velocity islands" in the contour map [23]. One such "high velocity island" is also shown in Figures 4.5 and 4.6. The contours reveal a high velocity "island" where the velocity is slightly higher than the surrounding region. In addition to the inflow region near the tape, the computational results also show inflow regions along the outer perimeter (denoted by arrows). This phenomenon was not observed clearly in the legacy experiments, which could be due to the low resolution of the experiments.

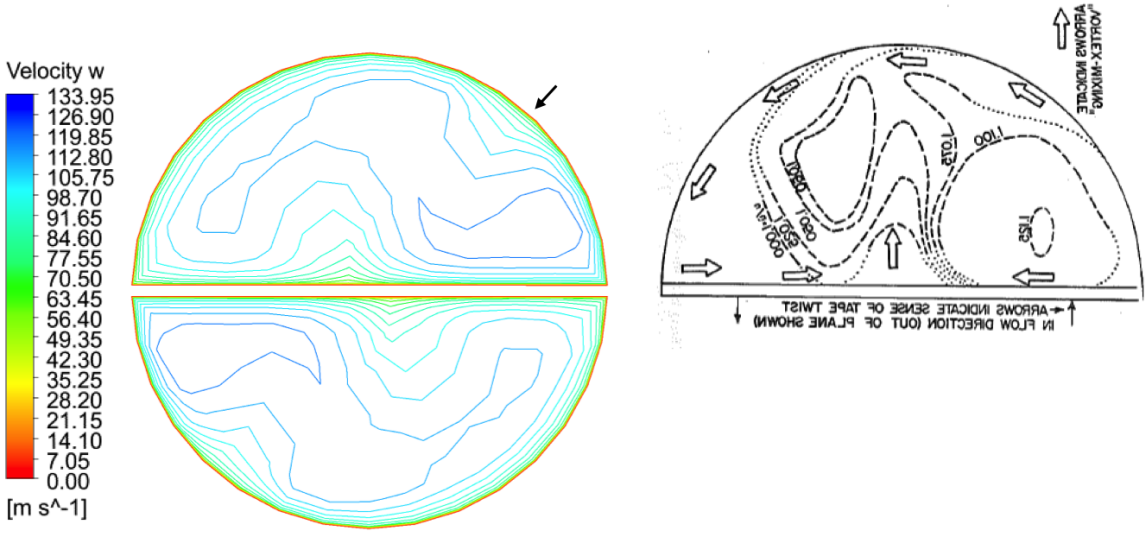


(a) (b)

Figure 4.5: Comparison of (a) computational axial velocity contour to (b) experimental flow measurements of Smithberg and Landis [23]

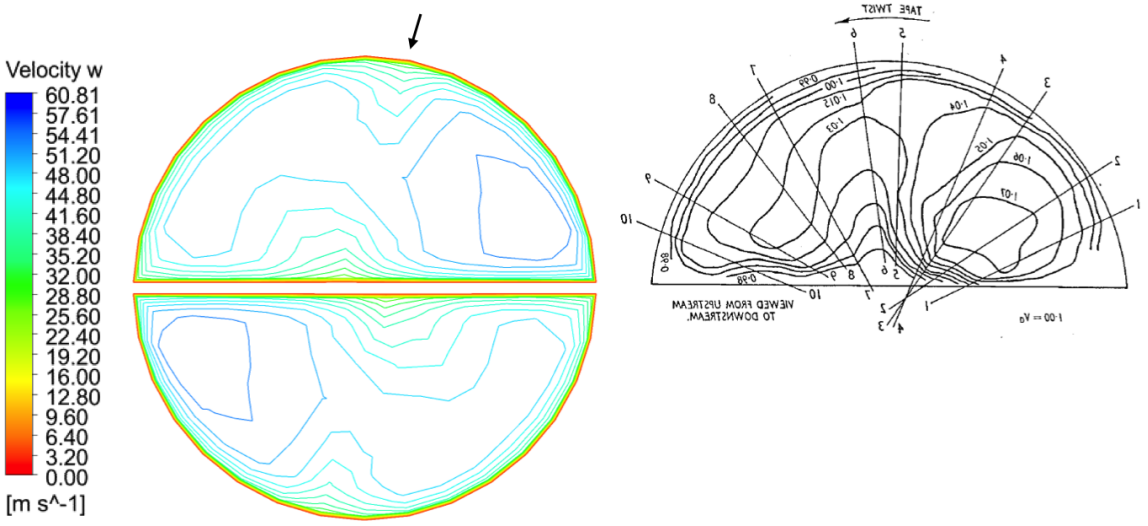


(a) (b)

Figure 4.6: Comparison of (a) computational axial velocity contour to (b) experimental flow measurements of Seymour [22]

### *4.2.2. Diabatic Validation*

#### *Calculations and Legacy Nusselt Number Correlations*

The diabatic results were compared to the well-accepted Manglik and Bergles correlations for turbulent twisted tapes via the Fanning friction factor and the Nusselt number [15]. The Nusselt number was compared to other legacy correlations as well [14-17]. The legacy Nusselt number correlations are shown in Table 4.4. As discussed by Manglik and Bergles, all parameters in the correlations are based on empty tube dimensions, and fluid properties are evaluated at the length averaged bulk temperature (mean temperature) unless noted otherwise [15]. Fluid properties were calculated using the IAPWS-IF97 formulation as discussed in Ref. [54]. The Nusselt number ($Nu$) was calculated such that

$$Nu = \frac{(HTC)(d)}{k_m} \tag{4.5}$$

where $k_m$ is the thermal conductivity at the mean temperature and $HTC$ is the heat transfer coefficient calculated from Newton's law of cooling as given by

$$HTC = \frac{q_{w,o}''}{T_{w,o} - T_{m,o}} \tag{4.6}$$

where $q_{w,o}''$ is the surface heat flux, $T_{w,o}$ is the surface temperature, and $T_{m,o}$ is the mean temperature at a plane near the exit. The mean temperature was calculated as defined by Incropera et al. [58] using an area integral function in the post processor such that

$$T_m = \frac{\int \rho u c_p T dA_c}{\dot{m} c_p} \tag{4.7}$$

The surface temperature and surface heat flux were calculated using the length average function along the outer perimeter.

Table 4.4: Legacy Nusselt number correlations

| Authors | *Nu* Correlation |
|---|---|
| **Gambill et al. [17]** | $Nu = \left[\frac{0.05014}{y^{0.09} Pr^{2/3} Re^{0.2}}\right](c_p G)[1 + (d/L)^{0.7}]\left(\frac{d}{k}\right)$ |
| **Lopina and Bergles [14]** | $Nu = F\left\{0.023 Re^{0.8} Pr^{0.4}(1 + 0.25y^{-2})^{0.4}\left[\frac{\pi + 2 - 2\delta/d}{\pi - 4\delta/d}\right]^{0.2}\left[\frac{\pi}{\pi - 4\delta/d}\right]^{0.8} + 0.193\left[\mathrm{Pr}\,\beta\Delta T_w (Re/y)^2\left[\frac{\pi}{\pi - 4\delta/d}\right]^2\right]^{1/3}\right\}$ <br> $F \cong 1$ |
| **Manglik and Bergles [15]** | $Nu = 0.023 Re^{0.8} Pr^{0.4}\left[\frac{\pi + 2 - 2\delta/d}{\pi - 4\delta/d}\right]^{0.2}\left[\frac{\pi}{\pi - 4\delta/d}\right]^{0.8}\left[1 + \frac{0.769}{y}\right]\left(\frac{\mu_b}{\mu_w}\right)^n$ <br> $n = \begin{cases} 0.18\ for\ liquid\ heating \\ 0.30\ for\ liquid\ cooling \end{cases}$ |
| **Ibragimov et al. [16]** | $Nu = \left\{0.021 Re^{0.8} Pr^{0.43}\left(\frac{Pr_b}{Pr_w}\right)^{0.25}\left[\frac{\pi + 2 - \frac{2\delta}{d}}{\pi - \frac{4\delta}{d}}\right]^{0.2}\left[\frac{\pi}{\pi - \frac{4\delta}{d}}\right]^{0.8}\right\} \cdot \left\{1 + \frac{5.65x10^4}{yRe^{1.2}}\left[\frac{\pi + 2 - 2\delta/d}{\pi - 4\delta/d}\right]^{1.2}\left[\frac{\pi}{\pi - 4\delta/d}\right]^{1.2}\right\}$ |

The Fanning friction factor was calculated similarly to Equation 4.1 with the inclusion of the density at the mean temperature. It was compared to the Manglik and Bergles friction factor correlation as shown in Table 4.2 with diabatic alterations included. Because this correlation was originally developed for isothermal conditions, it had to be altered for comparison to diabatic results. As discussed in Ref. [8], the isothermal friction factor for turbulent flows can be altered to the diabatic condition by following the recommendations of Lopina and Bergles [14]. Lopina and Bergles suggested the following multiplier to correct isothermal data to heated conditions for swirl flow

$$C_{f\,iso} = C_{f\,diabatic}\left(\frac{\mu_b}{\mu_w}\right)^{0.35(d_h/d)} \tag{4.8}$$

where $d_h$ is the hydraulic diameter, $\mu_b$ is the viscosity at the bulk temperature, and $\mu_w$ is the viscosity at the wall. Rearrangement of the multiplier provides the equation used to determine the diabatic friction factor for the Manglik and Bergles correlation

$$C_{f\,diabatic} = C_{f\,iso}\left(\frac{\mu_w}{\mu_b}\right)^{0.35(d_h/d)} \tag{4.9}$$

where $C_{f_{iso}}$ was calculated using the correlation shown in Table 4.2. It should be noted that this multiplier is not consistent with that provided by Manglik and Bergles in their review paper [8]. In that paper, the Lopina and Bergles multiplier is given as the inverse of that seen in Eq. 4.9. However, Eq. 4.9 is consistent with the work of Lopina and Bergles as well as that of Dormer and Bergles [14, 59]. Thus, the correction to the diabatic condition has been implemented as presented in Eq. 4.9.

### *Experimental Ranges of the Legacy Nusselt Number Correlations*

The Fanning friction factor and Nusselt number are first compared to the Manglik and Bergles correlations for turbulent swirl flow. This is then followed by a comparison of the Nusselt number to other legacy correlations. All of the correlations are based on experimental results, which range across various parameters.

Table 4.5 summarizes some of the key thermal-hydraulic parameters behind the legacy correlations used in this comparison. With the exception of Gambill et al. [17], the hydraulic parameters for the legacy experiments were discussed in Section 4.2.1. Lopina and Bergles performed experiments with electrically heated test sections for a range of Reynolds numbers and twist ratios. The temperature difference between the wall and the fluid (ΔT) was varied from 10 to 140°F, and the reported heat transfer coefficient (h) ranged from $2x10^3$-$1.8x10^4$ Btu/hrft$^2$ [14]. Considering the reported ΔT and h ranges, the heat flux range for these experiments can be calculated in SI units as 0.06-8 MW/m$^2$. Gambill et al. also completed experiments with electrically heated test sections. The tests were performed with a range of twist ratios (2.3-12), Reynolds numbers ($5x10^3$-$4.27x10^5$), and heat fluxes (2.5-25 MW/m$^2$) [17]. Gostintsev summarized the experiments performed by Ibragimov et al. A heat flux or temperature condition was not provided for these experiments, but a Nusselt number range of 200-600 was reported [16, 60]. Lastly, the Manglik and Bergles tests were performed for a range of parameters including various twist ratios, a range of Reynolds numbers, and a range of Prandtl numbers (3.5-100). The experiments were performed with a double-pipe heat exchanger where the resulting Nusselt numbers ranged from 25 to 280 for a twist ratio of y=4.5 [19, 55].

Table 4.5: Experimental parameters for legacy correlations

| Study | Fluid | Re | $q''$ [MW/m$^2$] | Nu |
|---|---|---|---|---|
| **Manglik and Bergles [19]** | Water; Ethylene Glycol | $3x10^2$ – $3.5x10^4$ | – | 25 – 280 |
| **Gambill et al. [17]** | Water | $5x10^3$ – $4.27x10^5$ | 2.5 – 25 | – |
| **Ibragimov et al. [16, 55]*** | Water | $1x10^4$ – $5x10^4$ | – | 200 – 600 |
| **Lopina and Bergles [14]** | Water | $8x10^3$ – $1.3x10^5$ | 0.06 – 8 | – |

* Reynolds numbers are based on the hydraulic diameter ($Re_h$) as cited in Ref. [55]. $Re_h$ for the diabatic validation are approximately $5x10^4$ and $9x10^4$.

A comparison of Tables 4.1 and 4.5 shows that the selected heat fluxes and Reynolds numbers for this study fall within some of the parameter ranges investigated in the legacy experiments. The chosen Reynolds numbers are within the ranges investigated by both Gambill et al., Lopina and Bergles, and Ibragimov et al. [14, 16, 17]. The heat fluxes are slightly below those investigated by Gambill et al. [17], but they fall within the range used by Lopina and Bergles [14]. While the Manglik and Bergles experiments are based on a limited range of data, the turbulent flow correlations were developed to have a "very generalized applicability." The turbulent correlations are cited as relevant for Reynolds numbers greater than $1x10^4$ and were validated against previously published data, which included gases and liquids, heating and cooling conditions, and a range of tape geometries [15]. The conditions simulated in the diabatic validation fall outside the Reynolds numbers and Nusselt numbers tested in the Manglik and Bergles experiments [19]. However, these correlations are thought to represent the current best modeling basis for the thermal-hydraulic performance of twisted tape enabled devices. This is indicated by their frequent use to predict the performance beyond the range of the experimental data in fusion relevant literature [61-63].

### *Comparison of Diabatic Global Parameters to Legacy Works*

Figure 4.7 shows the comparison of the Fanning friction factor between the simulated results and the Manglik and Bergles correlation [15] as calculated by Eq. 4.9 for the two heat fluxes investigated. The computational results are reasonably close to the correlation in all cases. Overall, the friction factor values are clustered together with only slight differences between the different heat fluxes (at given Reynolds numbers). As shown in Figure 4.7, the friction factor is more sensitive to the Reynolds number than the heat flux at these conditions. At both heat fluxes, the higher Reynolds number cases result in a lower friction factor. However, this is not indicative of a lower pressure drop, but rather is due to a higher inlet axial velocity in the denominator. Lastly, the clustering of results shown in Figure 4.7 indicates that the friction factor is not greatly affected by the choice of the turbulence model.

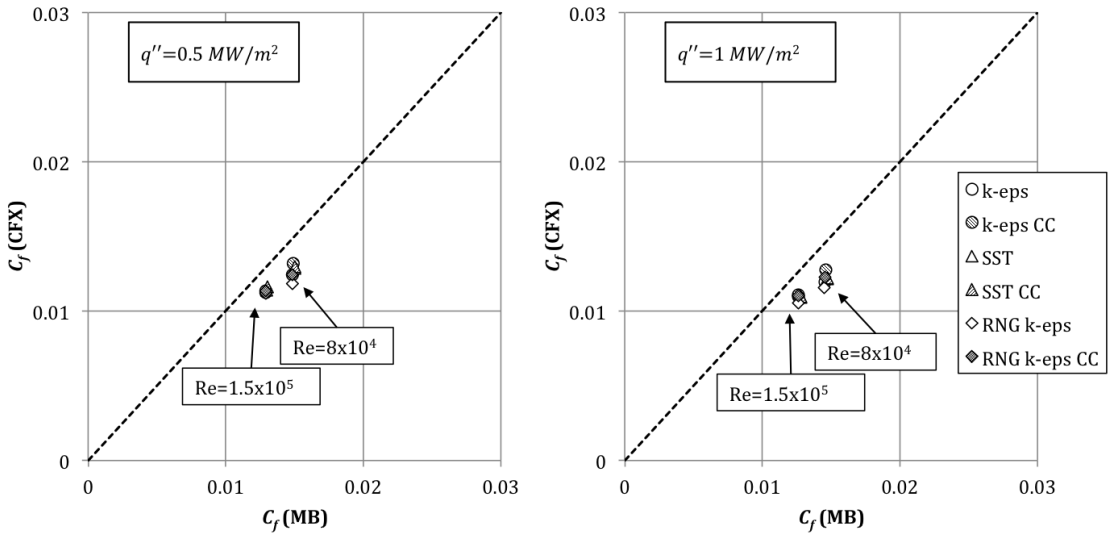


Figure 4.7: Diabatic Fanning friction factor comparison of simulated results (CFX) and the Manglik and Bergles correlation (MB) [15] for heat fluxes of 0.5 MW/m² (left) and 1 MW/m² (right)

The Nusselt number comparison is presented in Figure 4.8, where it is shown to be much more sensitive to the Reynolds number and heat flux than the friction factor. Figure 4.8 also reveals that higher Reynolds number flows and higher heat fluxes result in a better overall thermal performance. Futhermore, the Nusselt number calculations are more affected by the choice of turbulence model. The k-epsilon based models yield Nusselt numbers close to the correlation. However, as seen in Figure 4.8, each investigated turbulence model overpredicted the correlation in all cases. The k-epsilon models are relatively close to the Manglik and Bergles correlation, while the SST model greatly overpredicts the correlation in all cases. Figures 4.7 and 4.8 also show the impact of the curvature correction (CC) method to the friction factor and Nusselt number. Overall, the addition of the CC method does not appear to have a significant impact on the solutions.

The Nusselt number was further compared to other legacy correlations because of the wide range of computational results and the limited thermal range in the experiments behind the Manglik and Bergles correlation [15, 19]. Figure 4.9 shows the computational results along with four legacy correlations as shown in Table 4.4. Note that the legacy correlations are not linear. Lines have been drawn between two points on this figure to help guide the eye. The SST turbulence model overpredicts all of the legacy correlations in all cases investigated. The k-epsilon based models are in agreement with the Gambill et al. correlation [17] for all cases. The computational results are greater than the Manglik and Bergles, Lopina and Bergles, and Ibragimov et al. correlations [14-16] for all cases.

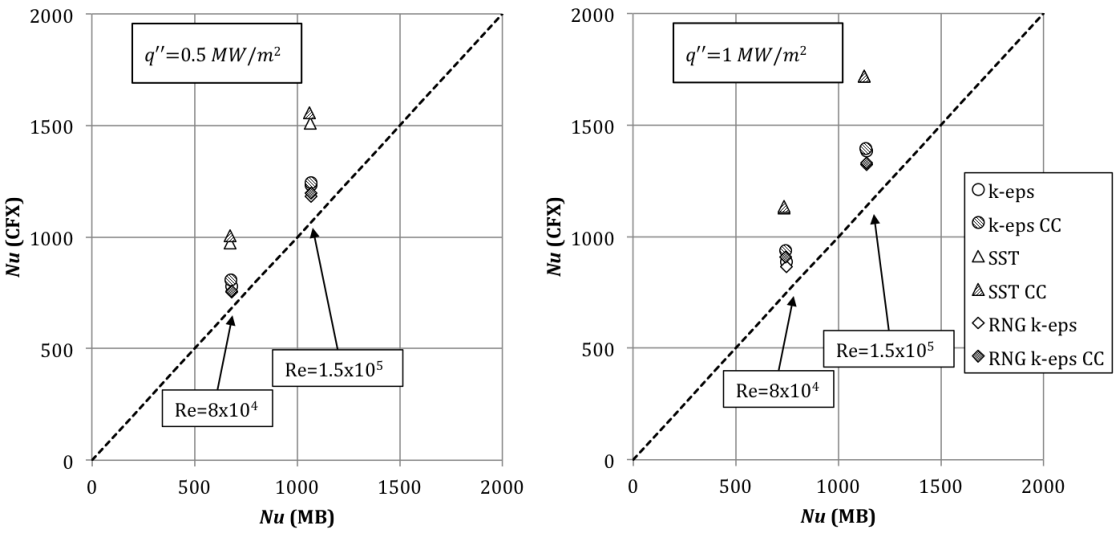


Figure 4.8: Nusselt number comparison of simulated results (CFX) and the Manglik and Bergles correlation (MB) [15] for heat fluxes of 0.5 MW/m² (left) and 1 MW/m² (right)

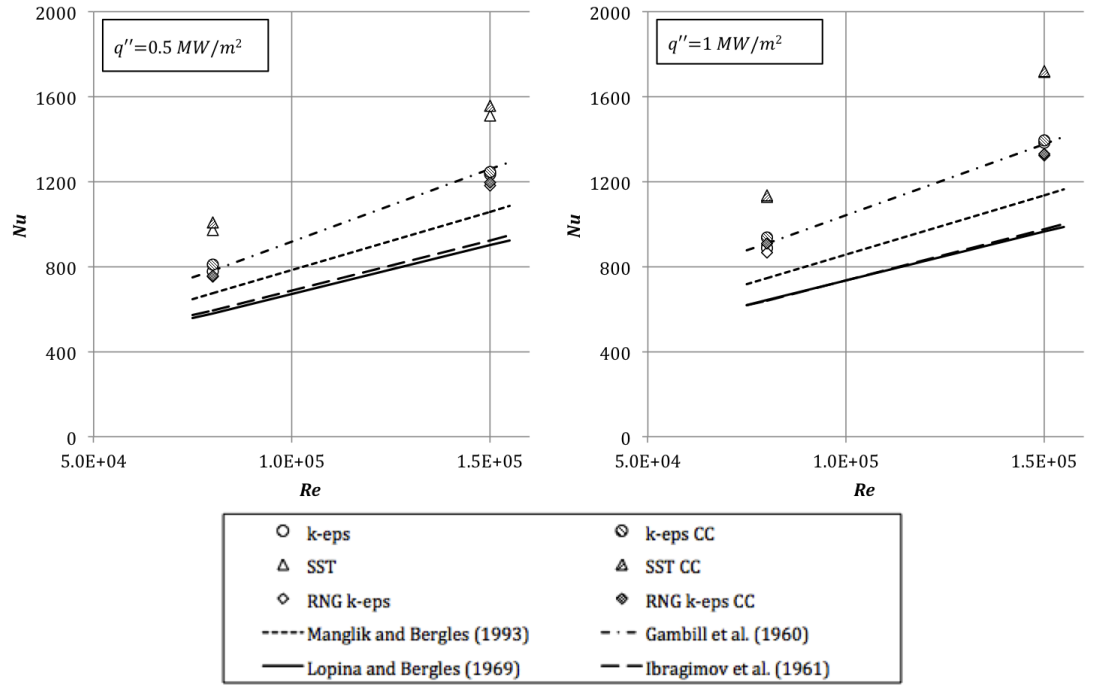


Figure 4.9: Nusselt number comparison of simulated results to legacy correlations [14-17] for heat fluxes of 0.5 MW/m² (left) and 1 MW/m² (right)

## 4.3. Investigation of Local Flow Information

### *4.3.1. Adiabatic Investigation into Local Flow Information*

#### *Adiabatic Flow Patterns*

The adiabatic local flow information was further investigated with water as the working fluid. Figure 4.10 (a) shows the total velocity contour for one of the eighteen cases investigated (Re=8x10$^4$, k-eps), while Figure 4.10 (b) shows the tangential velocity vectors at a plane near the exit (z=4.543 m). Figure 4.10 (b) helps to visualize how the flow is swirling throughout the tube. The contour shown in Figure 4.10 (a) (and the others investigated) is qualitatively similar to those in the experimental flow literature [22, 23]. The key features are still seen with water as a working fluid. These features include the inflow region near the center of the tape and a high velocity island. As with the air comparisons, inflow regions are also noted along the outer perimeter (denoted by arrows).

The flow patterns were investigated at three axial locations for all eighteen cases (as given in Table 4.6). The axial locations were chosen such that the tape was in a horizontal configuration near the beginning, middle, and end of the test section. Figure 4.11 shows the total velocity contours at those three locations for Re=8x10$^4$ and the k-epsilon turbulence model. While one might expect for fully developed flow to occur, it was not noted for these cases. The flow continued to change as it moved downstream. Furthermore, each turbulence model yielded different velocity contours as shown in Figure 4.12. The same qualitative features are yielded with each turbulence model such as the inflow regions and islands of high velocity. However, the actual contours vary from one to the next. While some yield a symmetric solution, others do not. Without more detailed flow visualization experiments, it is unclear which turbulence model provides the most accurate representation of the twisted tape induced swirl flow.

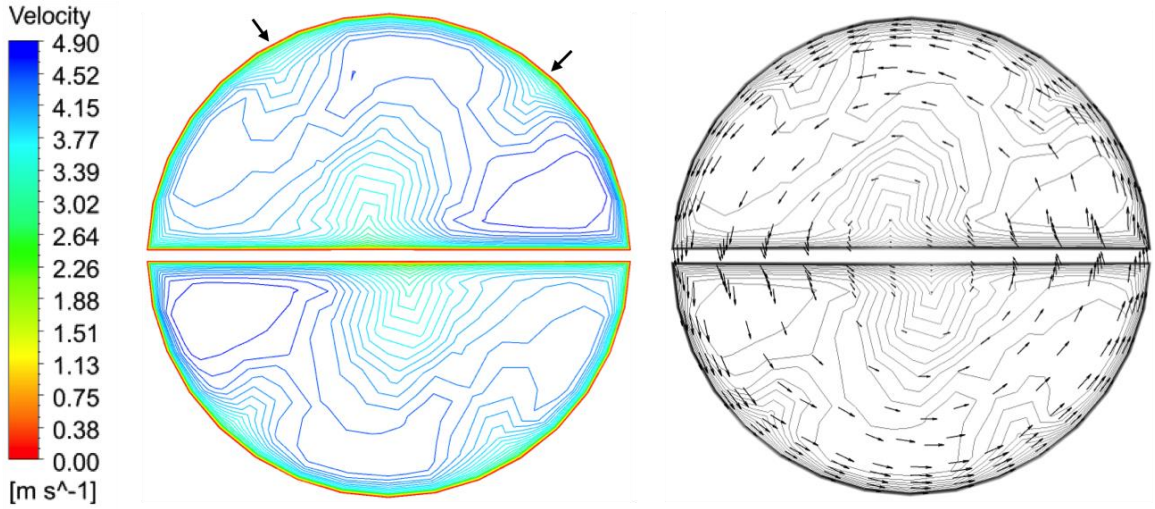


Figure 4.10: (a) Total velocity contour and (b) tangential velocity projection (Re=8x10$^4$, k-eps)

Table 4.6: Three axial locations selected for local flow investigation

| Plane | Axial location [m] | Test section location |
|---|---|---|
| **1** | 1.55673 | Start |
| **2** | 3.08169 | Middle |
| **3** | 4.54311 | End |

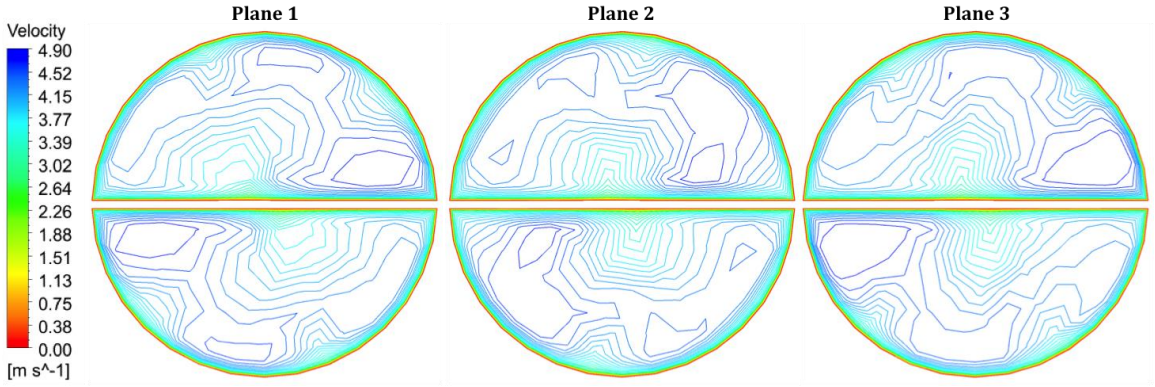


Figure 4.11: Comparison of total velocity contours as the flow moves downstream (Re=8x10$^4$, k-eps)

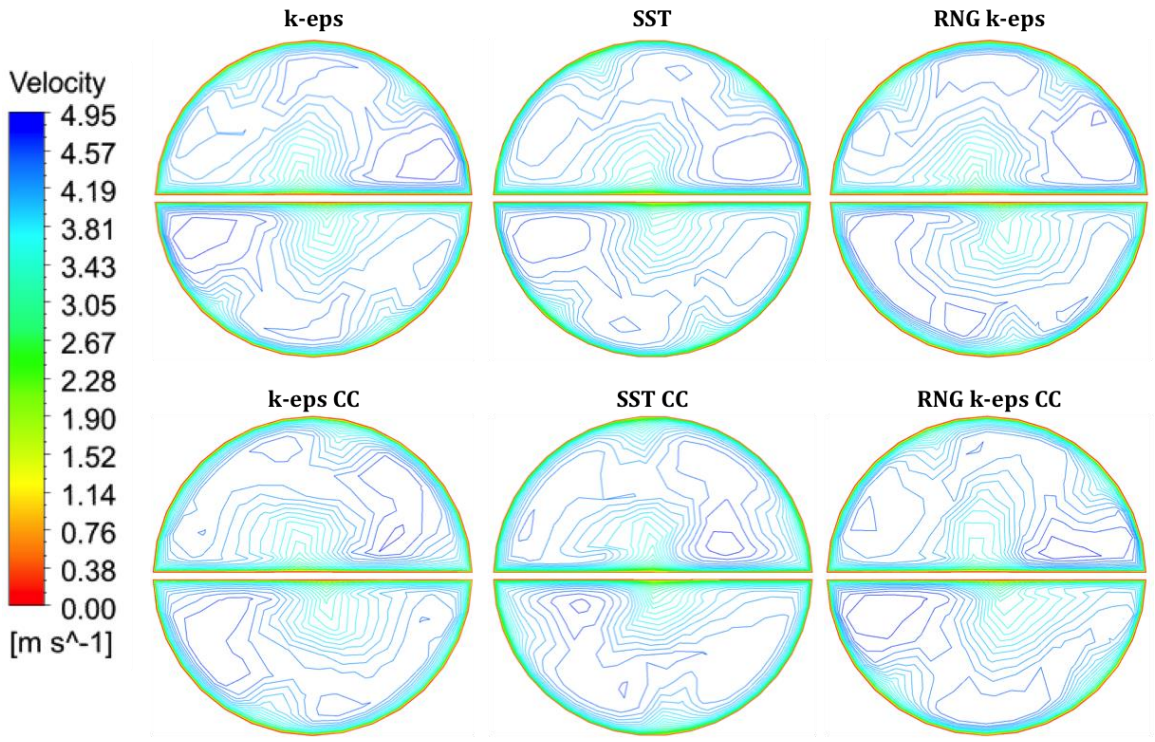


Figure 4.12: Comparison of total velocity contours for various turbulence models at a plane near the exit region (Plane 3, Re=8x$10^4$)

### *Further Investigation into Inflow Regions*

Inflow regions were seen in all of the aforementioned adiabatic cases and are believed to be a reflection of a physical phenomenon in the twisted tape flow. As can be seen in Figure 4.10 (a), the secondary flow causes some thickening of the boundary layer at the inflow regions. This local boundary layer thickening will cause lower local shear stress and should therefore result in a lower local heat transfer coefficient in the diabatic cases. Because of the reduced local heat transfer coefficient, these low shear stress regions could be candidates for early burnout.

The connection between the inflow regions and reduced local shear stress was investigated further by exporting the wall shear stress along the outer perimeter at a plane of interest (Plane 3 in Table 4.6). The wall shear stress is plotted against the angular coordinate as defined in Figure 4.13 along the outer perimeter of the domain (water-tube interface). The stress is shown in Figures 4.13 and 4.14, where the standard turbulence models and curvature correction models are compared, respectively. Comparison between the flow patterns in Figure 4.12 and the wall shear stress in Figures 4.13 and 4.14 illustrates the connection between the inflow regions and the local wall shear stress. In all cases, the dips in the stress correspond to the inflow locations around the outer perimeter.

The wall shear stress is further visualized by viewing surface contours of the stress along sections of the geometry. Figure 4.15 shows the wall shear contours for the k-epsilon turbulence model and $Re=8x10^4$ for half of the water domain in the swirling region. The geometry is cut into sections for easier viewing. The cut planes are indicated by the outlined numbers, and the locations are given in Table 4.7.

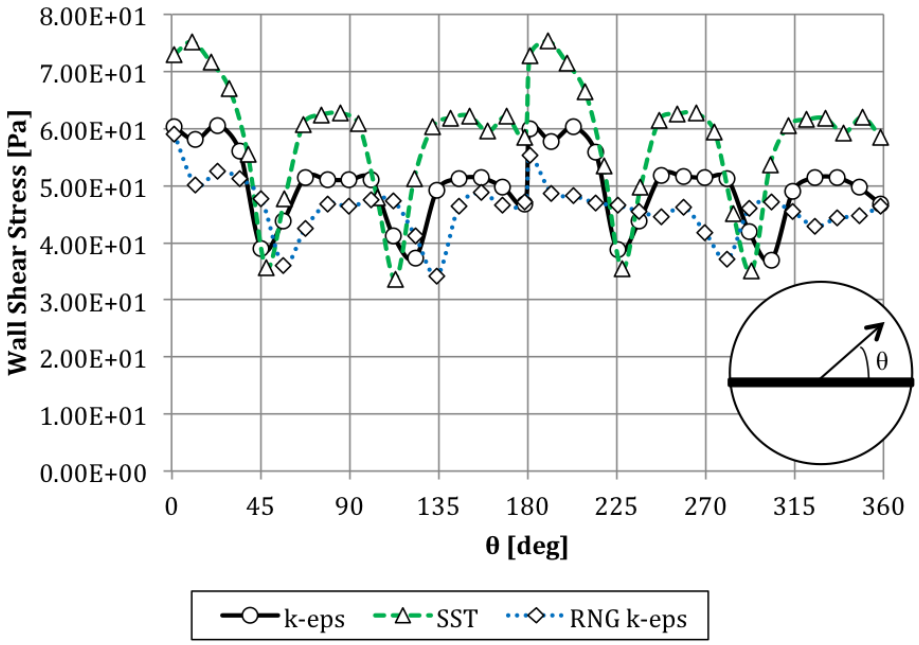


Figure 4.13: Wall shear stress for standard turbulence models along the outer perimeter at a plane near the exit region (Plane 3 in Table 4.6, Re=8x10$^4$)

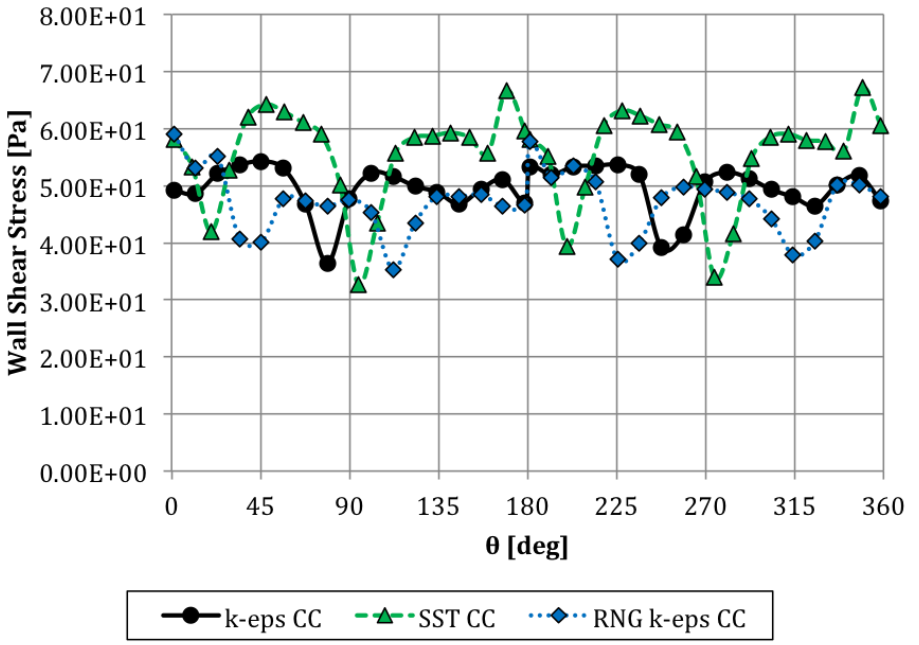


Figure 4.14: Wall shear stress for curvature correction (CC) turbulence models along the outer perimeter at a plane near the exit region (Plane 3 in Table 4.6, Re=8x10$^4$)

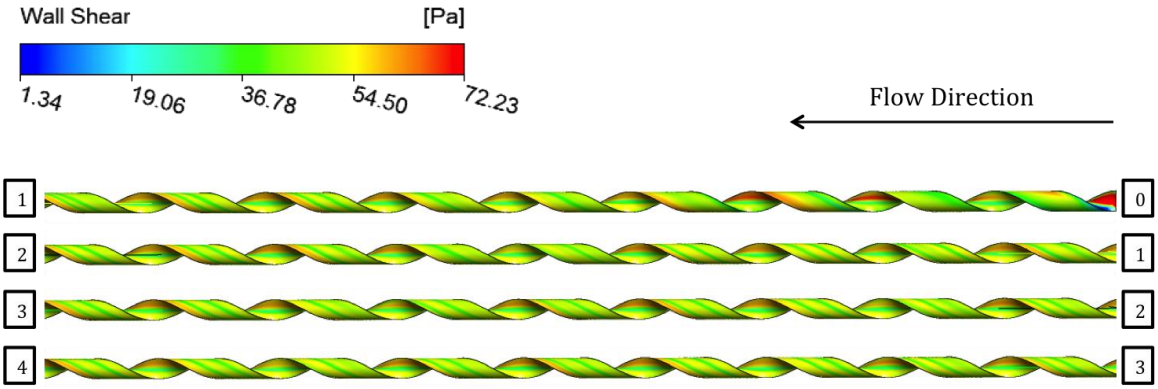


Figure 4.15: Adiabatic wall shear stress contours where cut plane locations are shown in Table 4.7 (Re=8x10$^4$, k-eps)

Table 4.7: Cut plane locations for wall shear stress contours

| Plane | Axial location [m] |
|---|---|
| **0** | 0 (start tape) |
| **1** | 1.143 |
| **2** | 2.286 |
| **3** | 3.429 |
| **4** | 4.572 |

Figure 4.15 shows the apparent wall shear stress "striping" that develops in twisted tape induced swirl flow. In this figure, the inflow regions correspond to the "striping" of low wall shear stress. The primary stripe along the inside of the geometry represents the inflow region that occurs along the water-tape interface. As shown in Figure 4.15, this is a constant feature throughout the flow field. Figure 4.15 also illustrates how the inflow regions along the outer perimeter shift along the length of the geometry. The number of so-called stripes and the location of those stripes (which correspond to inflow regions) shifts along the length of the test section.

To this author's knowledge, this phenomenon has not been cited in the twisted tape induced swirl flow literature. The relationship between the inflow regions and the heat transfer coefficient will be further investigated in the diabatic validation.

### *Transient Studies for Further Mesh Refinement*

Considering the differences in the local information across axial locations and turbulence models, it was determined that further mesh refinement was required. The mesh refinement was performed with transient solvers because finer meshes picked up unsteadiness in the flow field. Figure 4.16 shows the three mesh resolutions investigated: converged steady state (SS), first transient refinement (TC1), and second transient refinement (TC2). The geometry was simplified for the transient solutions to offset the increased computational cost. The entrance and exit regions were removed from the model, and the solution was completed on only half of the water domain. The transient solutions were performed for only one turbulence model (k-epsilon) at one Reynolds number ($8x10^4$). The solution duration was set to 200 outer iterations with a timestep of 0.05 [s]. The mesh statistics and runtime for these solutions are shown in Table 4.8. The runtimes reflect the significant increase in computational cost incurred with the transient solutions. The transient solutions took approximately 48 and 535 times longer than the steady solution, respectively.

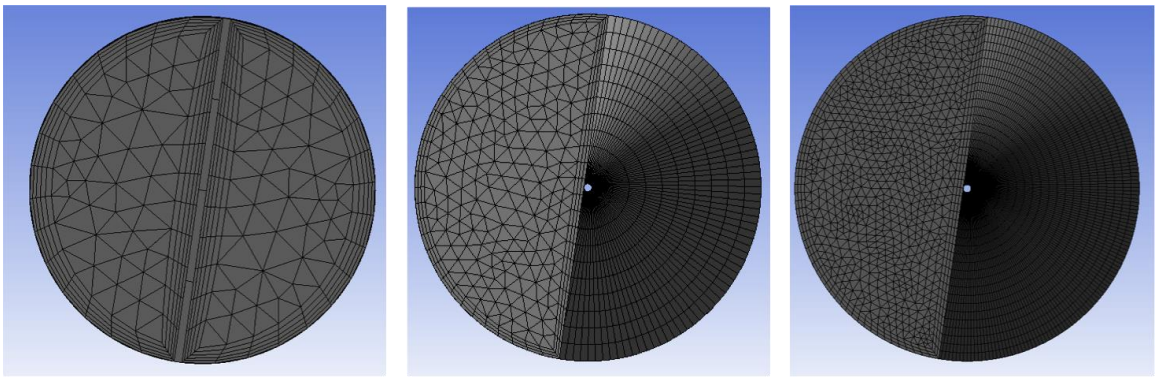

(a) (b) (c)

Figure 4.16: Mesh resolutions utilized for refinement study including (a) converged steady state (SS), (b) first transient refinement (TC1), and (c) second transient refinement (TC2)

Table 4.8: Mesh statistics and runtimes for mesh refinement studies

| Solution | Number of elements | Runtime* [hr] |
|---|---|---|
| **SS** | $1x10^6$ | 0.4 |
| **TC1** | $2.7x10^6$ | 19 |
| **TC2** | $1.63x10^7$ | 214 |

* Each solution was run in parallel on 30 processors. Runtime refers to the wall-clock time for each solution.

Both global and local information were compared across the steady and transient solutions. The pressure drop (ΔP) was calculated for all the cases. The steady state solution resulted in a pressure drop of ΔP=85,906 Pa. Meanwhile, both transient solutions yielded the same pressure drop value (ΔP=84,989 Pa). The steady state solution resulted in a slightly higher pressure drop, but this result is only approximately 1% higher than the transient solutions.

Figure 4.17 shows the comparison between total velocity contours at an axial location near the exit (Plane 3 as seen in Table 4.6). The contours presented for the transient solutions represent the time-averaged total velocity at that axial location. The time-averaged variables were solved for in CFX as the root mean square (RMS) of the instantaneous variable. As seen in Figure 4.17, the transient results revealed similar inflow regions as seen with the steady solver. However, the flow patterns did not appear to reach a steady or fully developed state as the solutions continued to change with each mesh refinement. The solutions also continued to change downstream. Figure 4.18 shows a comparison of the total velocity contours for TC1 and TC2 at three axial locations (as shown in Table 4.6). The results are qualitatively similar with TC2 providing smoother contours than TC1.

The wall shear stress striping was also investigated for one transient solution (TC1). The stress contours are shown in Figures 4.19 and 4.20, where both the RMS and instantaneous contours are shown, respectively. The instantaneous wall shear stress was taken at the end of the transient solution such that the time (t) was 10 seconds. The geometry is cut into sections for easier viewing, and the cut plane locations are given in Table 4.7. As indicated in Figures 4.19 and 4.20, the wall shear stress striping is not only captured with a steady solver. It is also seen with a refined mesh and a transient approach. This bolsters the statement that the striping is believed to be a physical feature of the twisted tape induced swirl flow as it has been seen in every case investigated in this study thus far.

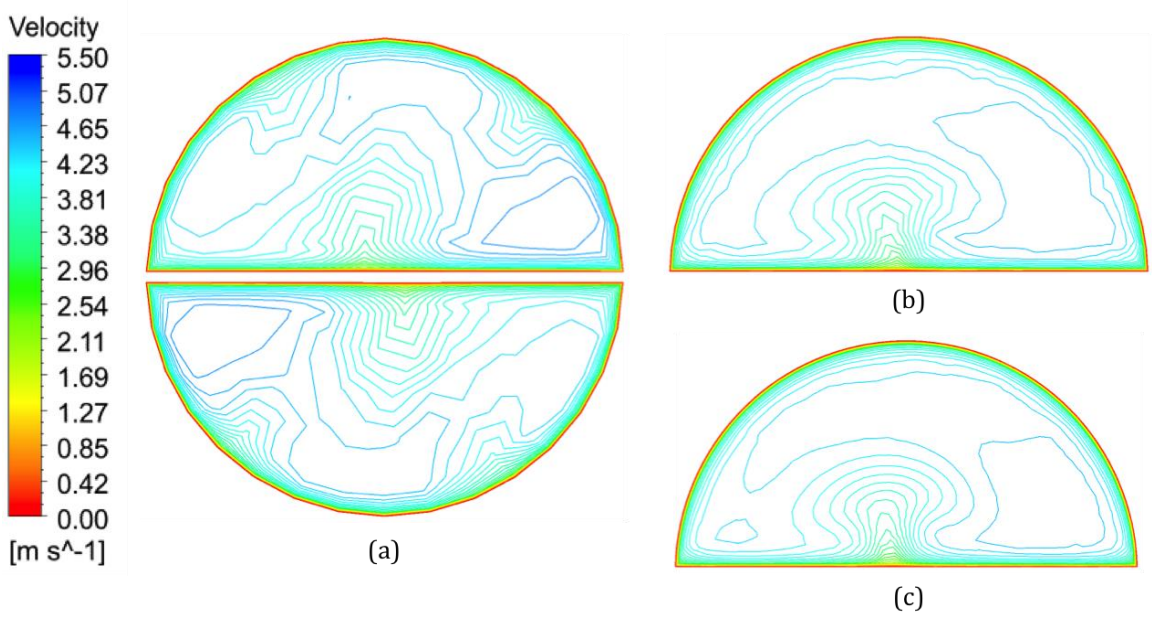


Figure 4.17: Comparison of total velocity contours for (a) SS, (b) TC1, and (c) TC2 at a plane near the exit region

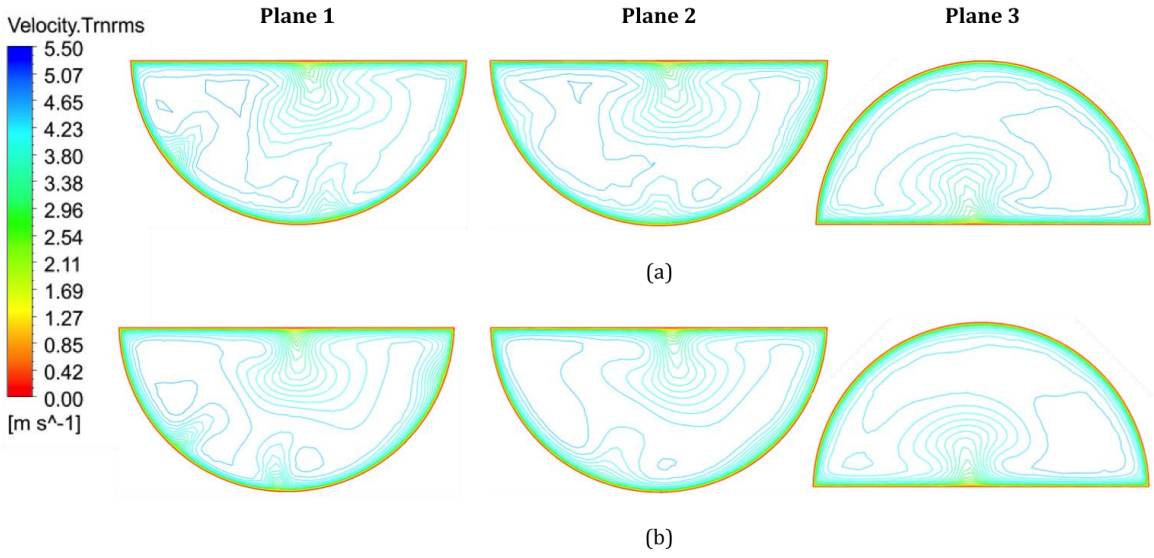


Figure 4.18: Comparison of total velocity contours for (a) TC1 and (b) TC2 at three axial locations

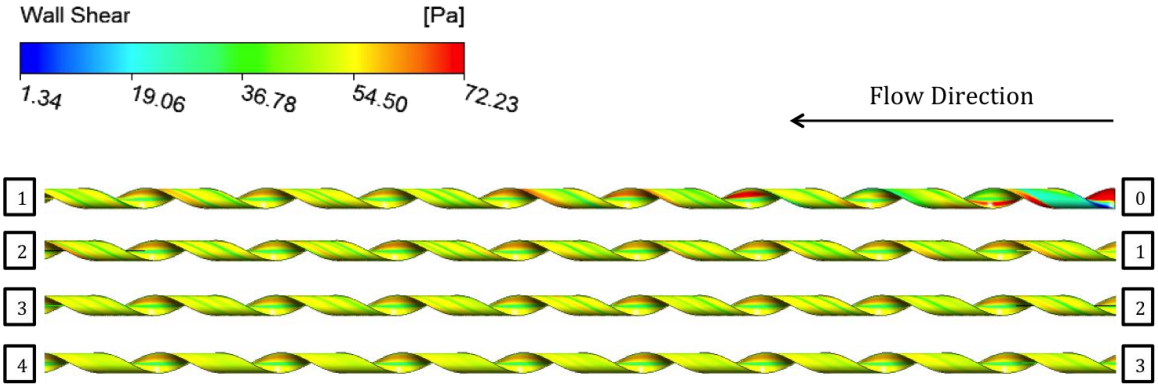


Figure 4.19: RMS wall shear stress contours for transient solution where cut plane locations are shown in Table 4.7 (TC1, Re=8x10$^4$, k-eps)

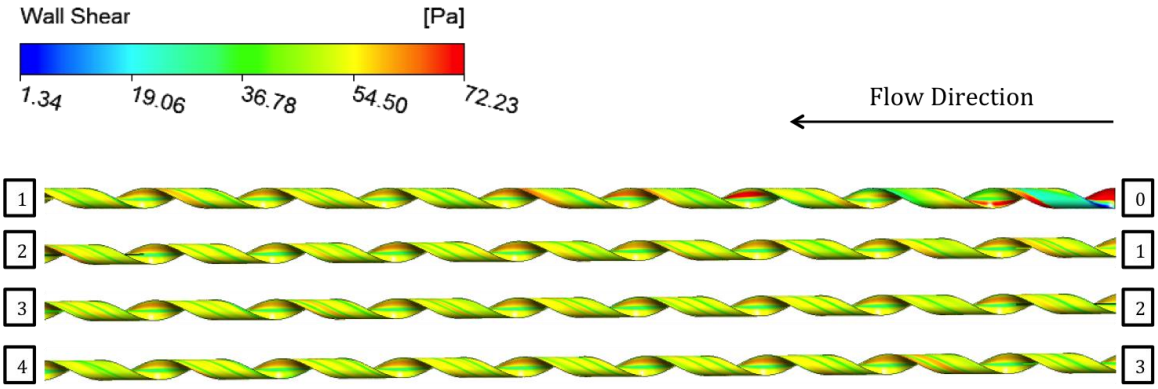


Figure 4.20: Instantaneous wall shear stress contours for transient solution where cut plane locations are shown in Table 4.7 (TC1, t=10 s, Re=8x10$^4$, k-eps)

Figures 4.19 and 4.20 also reveal the difference between the RMS and instantaneous wall shear stress. The inflow regions are apparently smoothed out by the RMS treatment on the water-tube interface near the end of the geometry. Meanwhile, the striping continues throughout the entire length for the instantaneous variable.

In general, the figures in the mesh refinement study reveal a few things about the twisted tape induced swirl flow. First, in all cases, the inflow regions and wall shear stress striping were noted at some point along the geometry. Therefore, the same key qualitative features were not only noted across all turbulence models investigated but also with further mesh refinement and transient solutions. Secondly, Figures 4.17 and 4.18 highlight the need for further high-resolution computational investigations of twisted tape induced turbulent swirl flow. A completely mesh-independent solution was not achieved in this study. While the global parameter (pressure drop) reached a constant value, the local flow information continued to change as the mesh was refined. A detailed transient study should be performed to obtain the CFD best practices for modeling twisted tape induced swirl flow. However, considering the available computational resources, a detailed transient study was determined to be outside the scope of this work. All work that follows this section was completed with a steady solver.

### *4.3.2. Diabatic Investigation into Local Flow Information*

#### *Diabatic Flow Patterns and Temperature Contours*

The diabatic results were further investigated at the local level through flow patterns and tempature contours. The flow patterns were investigated at three axial locations (as shown in Table 4.6). Figure 4.21 shows the total velocity contours at those three locations for Re=8x10$^4$, $q''$=1 MW/m$^2$, and the k-epsilon turbulence model due to a counterclockwise rotation in the water (as shown in Fig. 4.10 (b)). The diabatic flow patterns are qualitatively similar to the adiabatic results shown in Section 4.3.1 and those observed in the legacy adiabatic experiments [22, 23].

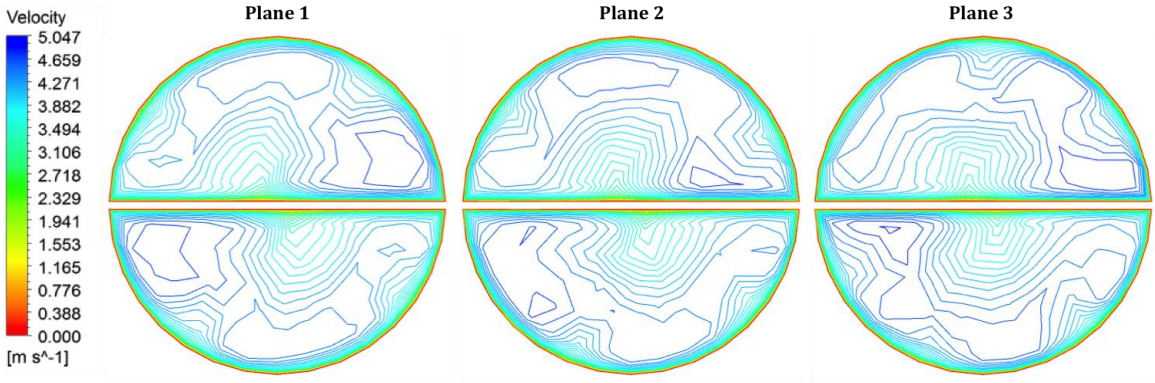


Figure 4.21: Comparison of diabatic total velocity contours as the flow moves downstream (Re=8x10$^4$, $q''$=1 MW/m$^2$, k-eps)

Fully developed flow was not noted for the diabatic cases investigated. As seen in Figure 4.21, the flow pattern continued to change in the downstream direction. Furthermore, the turbulence models yielded different velocity contours as shown in Figure 4.22. Similar qualitative features are noted with the various turbulence models such as islands of high velocity and inflow regions. However, the contours change from one model to the next. Some of the turbulence models result in a symmetric solution, but others do not. As discussed in Section 4.3.1, it is unclear which turbulence model provides the most accurate representation of the swirl flow because of a lack of detailed flow visualization experiments.

In the diabatic cases, the local temperature contours were also investigated at multiple axial locations and across various turbulence models. The temperature contours were investigated at two axial locations near the middle and end of the test section (as shown in Table 4.6). The contour is not shown for the beginning of the test section (Plane 1) because the temperature is essentially constant at this location. Figure 4.23 shows the temperature contours at for Re=8x10$^4$, $q''$=1 MW/m$^2$, and the k-epsilon turbulence model. As would be expected, Fig. 4.23 shows that the temperature increases as the fluid moves downstream.

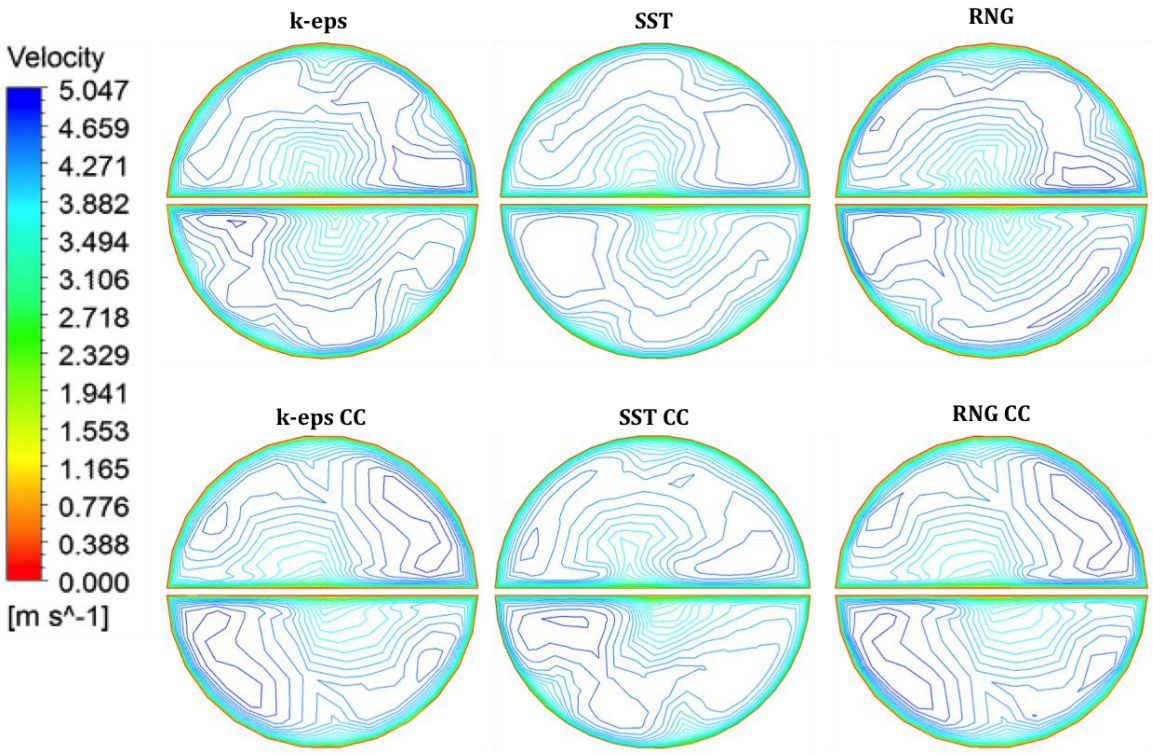


Figure 4.22: Comparison of diabatic total velocity contours for various turbulence models at a plane near the exit region (Plane 3 in Table 4.6, Re=8x10$^4$, $q''$=1 MW/m$^2$)

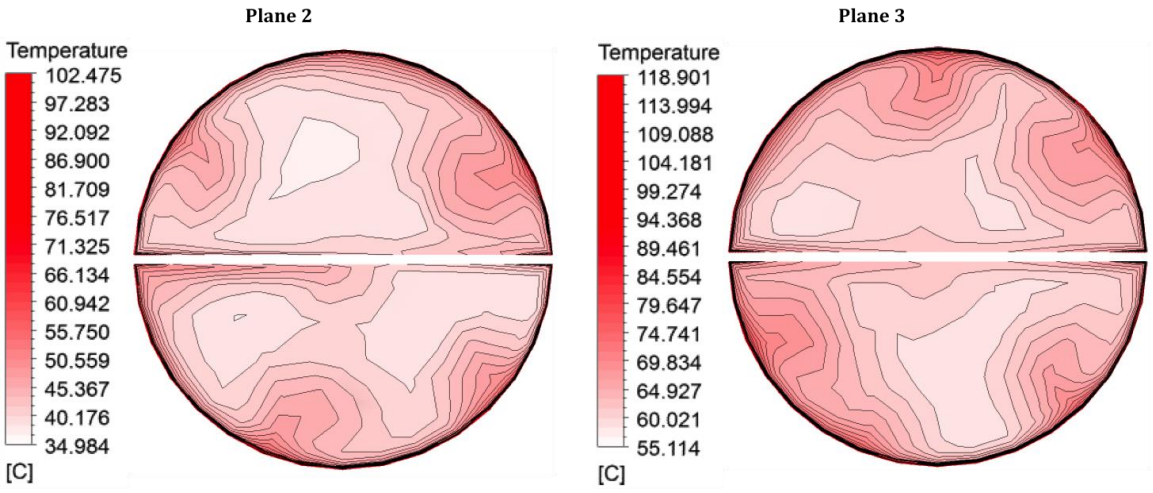


Figure 4.23: Comparison of temperature contours as the flow moves downstream (Re=8x10$^4$, $q''$=1 MW/m$^2$, k-eps)

It should be noted that for this case, the maximum temperature is greater than the saturation temperature (Tsat), where Tsat≈100°C at atmospheric pressure. However, this occurs near the end of the test section after roughly 2.7 m of applied heat. In the case of fusion relevant geometries, the test section lengths would be much shorter, and thus, boiling would not occur for this case. Furthermore, higher pressures would be imposed for fusion relevant conditions, which would increase the saturation temperature and suppress boiling. Figure 4.24 shows the temperature contours for various turbulence models. Similar to the flow patterns shown in Figure 4.22, the temperature contours vary from one turbulence model to the next. Furthermore, some solutions are symmetric, and others are not.

### *Further Investigation of Inflow Regions*

As discussed in Section 4.3.1, the secondary flow causes some thickening of the boundary layer at the inflow regions. This local boundary layer thickening will cause lower local shear stress and thus, a lower local heat transfer coefficient. These low shear stress regions could be candidates for early burnout. Figure 4.25 shows the velocity and temperature contours for Re=1.5x$10^5$, $q''$=1 MW/$m^2$, and the k-epsilon turbulence model. This figure allows for an initial investigation of this phenomenon through a qualitative comparison of the velocity and temperature contours at a particular axial location. Comparison of the contours shows that the inflow regions appear to correspond to hot spots along the water surface (as denoted by the arrows).

To investigate this phenomenon further, the wall shear stress, wall heat flux, and surface temperature were exported along the perimeter a plane of interest (near the exit). The heat transfer coefficient was calculated at each surface point using Eq. 4.6 along with the previously calculated mean temperature. Note that in Figure 4.25, the areas of interest for the temperature contour lie along the outer perimeter. Thus, the initial investigation will be performed along the water-tube interface. Following that, the entire perimeter will be investigated to show the full picture at the plane of interest.

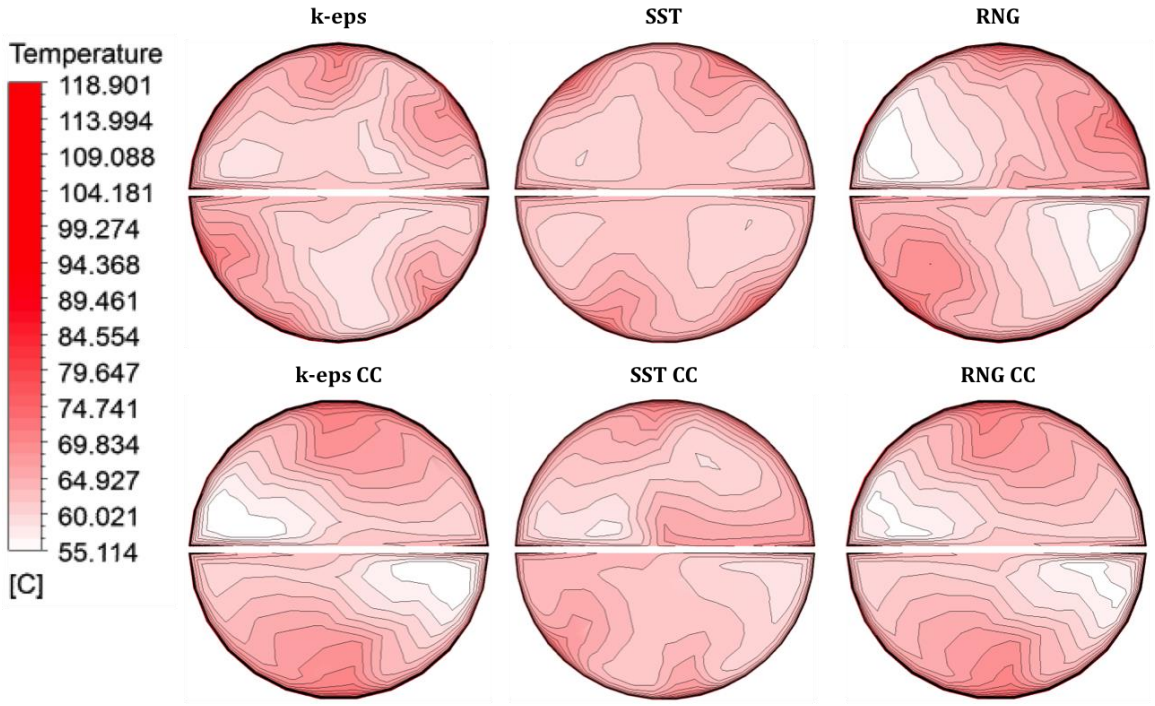


Figure 4.24: Comparison of temperature contours for various turbulence models at a plane near the exit region (Plane 3 in Table 4.6, Re=8x10$^4$, $q''$=1 MW/m$^2$)

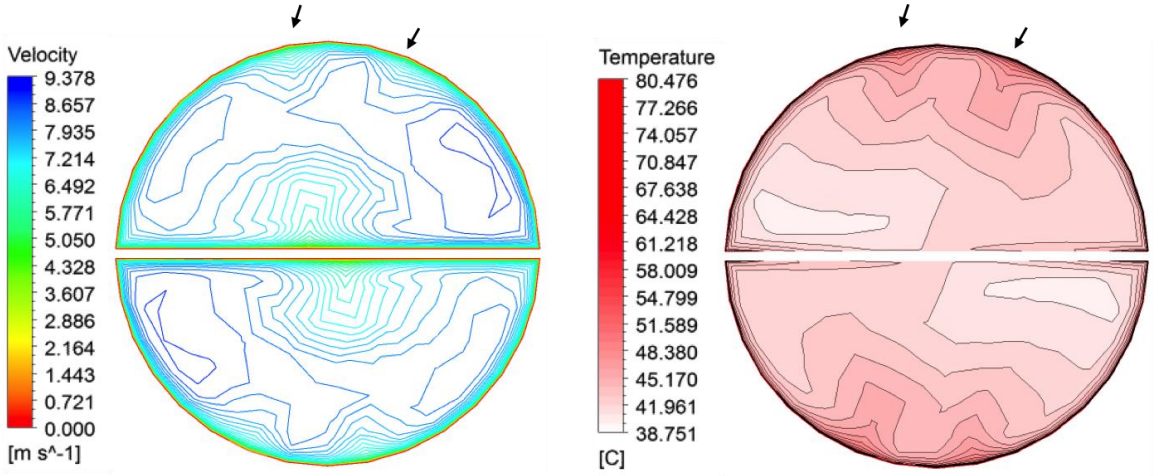


(a) (b)

Figure 4.25: (a) Total velocity and (b) temperature contours at a plane near the exit region (Plane 3 in Table 4.6, Re=1.5x10$^5$, $q''$=1 MW/m$^2$, k-eps)

The wall shear stress and wall heat flux are shown together in Figure 4.26 for Re=1.5x$10^5$, $q''$=1 MW/$m^2$, and the k-epsilon turbulence model. Similarly, the wall shear stress and heat transfer coefficient (HTC) are shown together in Figure 4.27, and the wall shear stress and surface temperature (Ts) are shown in Figure 4.28. In each figure, the results are plotted against the angular coordinate as defined in Figure 4.26. The dips in the wall shear stress correspond to dips in the wall heat flux, which leads to decreases in the HTC. The decreased HTC leads to increased values for the surface temperature as shown in Figure 4.28. Figures 4.26-4.28 support the assertion that these regions of low wall shear stress could be likely candidates for early burnout.

The wall heat flux, wall shear stress, HTC, and Ts were also investigated along the entire perimeter including the water-tube and water-tape interfaces. Figure 4.29 shows a comparison of those parameters for Re=1.5x$10^5$, $q''$=1 MW/$m^2$, and the standard turbulence models. The curvature correction models were excluded because they did not appear to have a significant effect on the global solutions. As seen in Figure 4.29 (a), the wall heat flux goes to nearly zero along the water-tape interface. The turbulence models calculate similar heat flux values with SST showing an opposite trend at the water-tape interface than the k-epsilon based models. The HTC is shown in Figure 4.29 (b). This reveals a negative HTC at the water-tape interface, which is due to heat transferring from the hot water to the cool tape. The SST model results in a more extreme HTC at the water-tape interface than the k-epsilon based models, which is evident by the spiking shown in Fig. 4.29 (b). As shown in Figure 4.29 (c), the greatest drops in the wall shear occur at the water-tape interface. There are differences in the wall shear variation across the turbulence models, but the magnitude is in a similar range for each. Lastly, the surface temperature is shown in Figure 4.29 (d). The lowest temperatures occur at the water-tape interface, while the peak temperatures correspond with dips in the wall shear and HTC. The SST model results in lower peak temperatures along the water-tube interface, while the k-epsilon based models predict a peak temperature roughly 10 degrees higher.

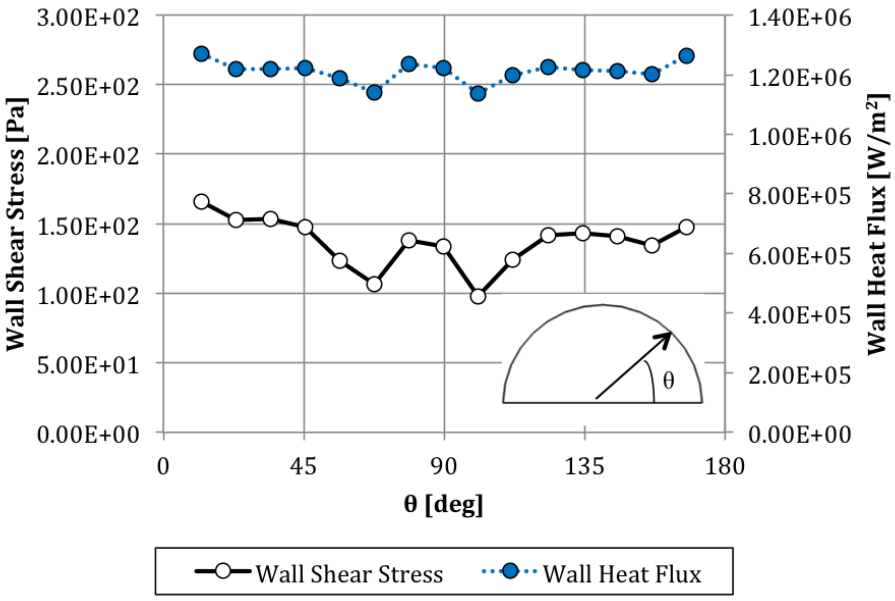


Figure 4.26: Comparison of wall shear stress and wall heat flux along the upper perimeter at a plane near the exit region (Plane 3 in Table 4.6, Re=1.5x10$^5$, $q''$=1 MW/m$^2$, k-eps)

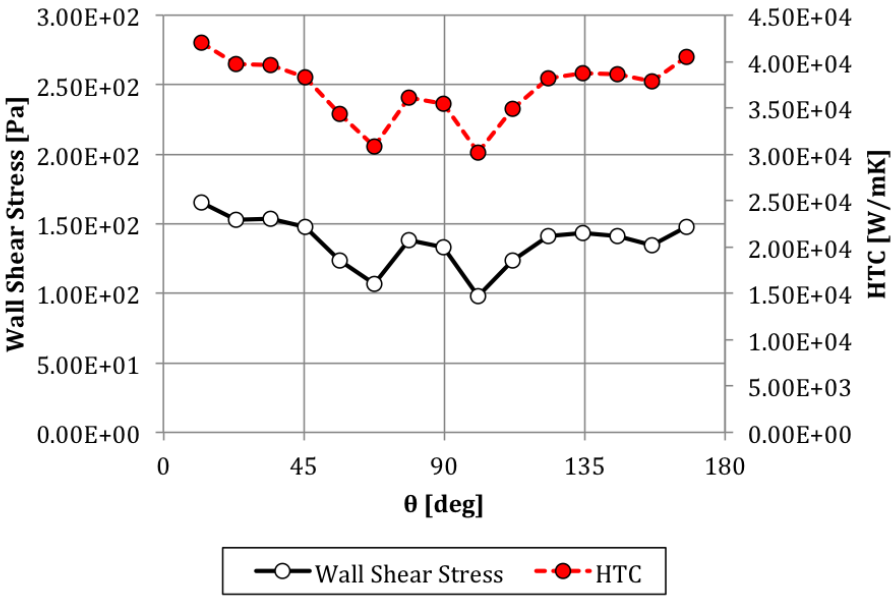


Figure 4.27: Comparison of wall shear stress and heat transfer coefficient along the upper perimeter at a plane near the exit region (Plane 3 in Table 4.6, Re=1.5x10$^5$, $q''$=1 MW/m$^2$, k-eps)

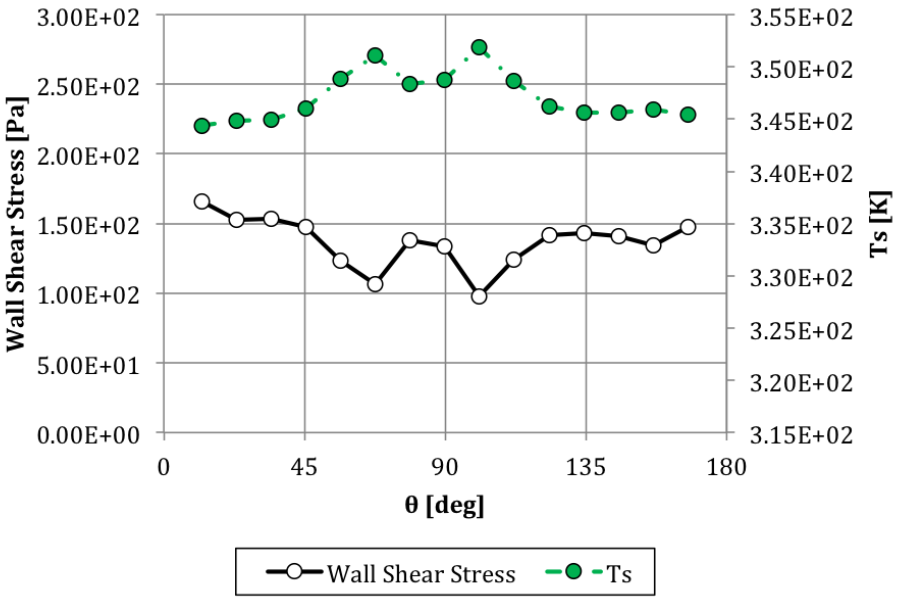


Figure 4.28: Comparison of wall shear stress and surface temperature along the upper perimeter at a plane near the exit region (Plane 3 in Table 4.6, Re=1.5x10$^5$, $q''$=1 MW/m$^2$, k-eps)

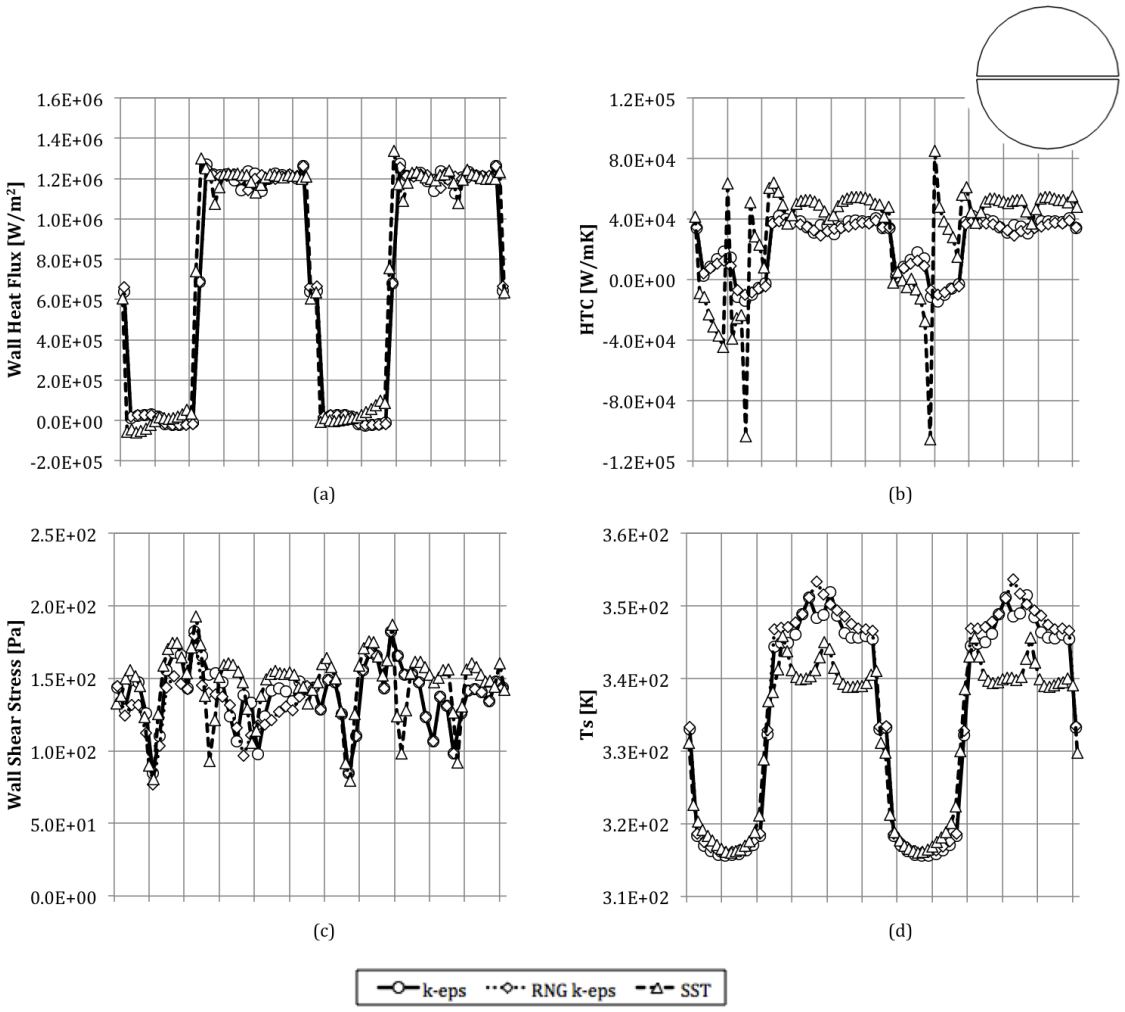


Figure 4.29: Comparison of (a) wall heat flux, (b) heat transfer coefficient, (c) wall shear stress, and (d) surface temperature for standard turbulence models at a plane near the exit (Plane 3 in Table 4.6, Re=1.5x$10^5$, $q''$=1 MW/$m^2$)

The local wall shear stress can be further visualized by viewing the contours on the water-tube and water-tape interfaces. Figure 4.30 shows the wall shear contours for all of the turbulence models investigated for Re=1.5x$10^5$ and $q''$=1 MW/$m^2$. The wall shear stress contours are shown for half of the water domain in the swirling region. For easier viewing, the geometry is cut into sections and only the first half of the geometry is shown in Figure 4.30. The cut planes are indicated by the outlined numbers, and the locations are provided in Table 4.7. Similarly to the adiabatic results in Section 4.3.1, the shear stress contours reveal striping that develops in twisted tape induced swirl flow. The inflow regions correspond to the "striping" of low wall shear stress, and this phenomenon is captured by all of the turbulence models investigated in this study.

## 4.4. Selection of Turbulence Model

The adiabatic and diabatic validations served for an investigation into the variability of the results due to different turbulence models. Before continuing on, a single turbulence model was chosen for the rest of the work. The results due to different models were weighed, and a turbulence model was chosen through the use of an evaluation matrix.

In both sections, it was determined that the curvature correction method, as it was implemented in this work, had little impact on the solution. Thus, it was excluded as an option moving forward. Qualitatively, the various turbulence models yielded similar local features. However, the exact flow patterns and temperature contours varied from one model to the next. Without more detailed flow visualization experiments, it is difficult to state which model provides the most accurate representation of the twisted tape induced swirl flow.

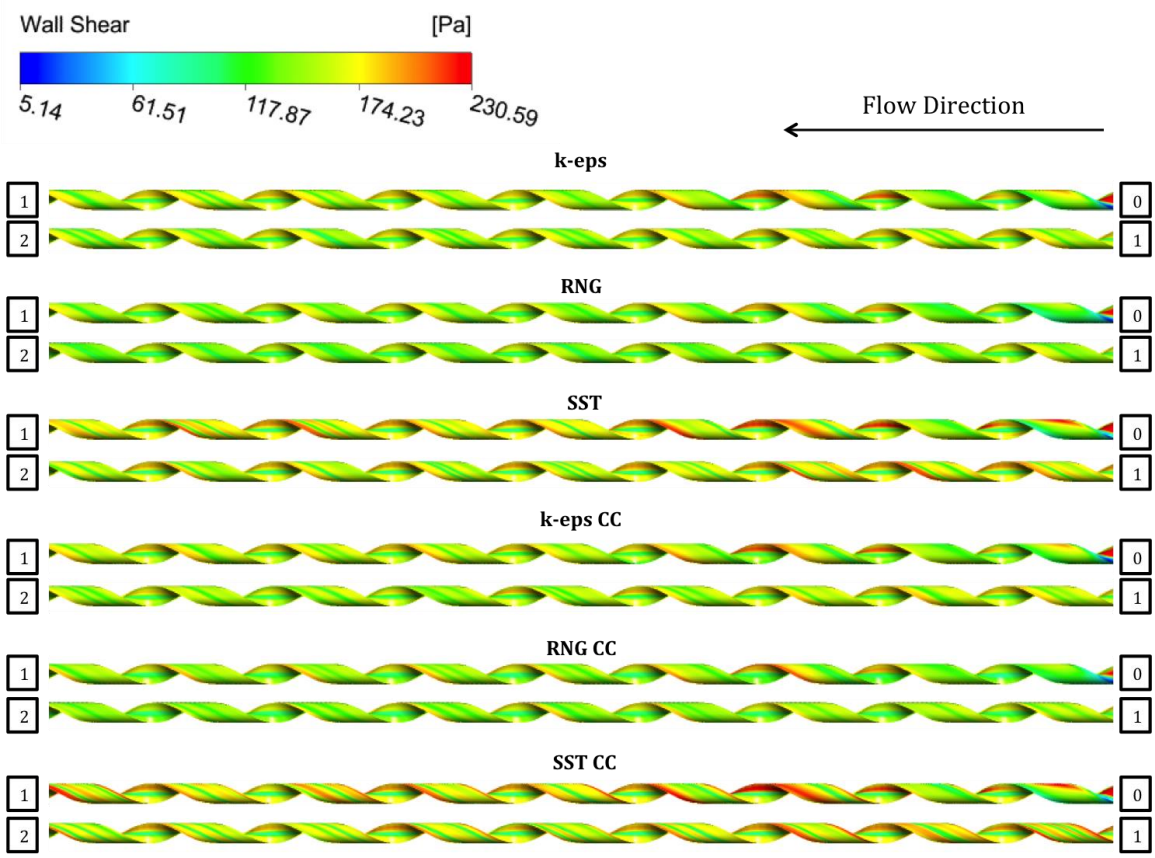


Figure 4.30: Diabatic wall shear stress contours for various turbulence models where cut plane locations are shown in Table 4.7 (Re=1.5x10$^5$, $q''$=1 MW/m$^2$)

There is more guidance available with the global parameters such as the Fanning friction factor and the Nusselt number. For a majority of the cases investigated, the friction factor was not greatly affected by the choice of turbulence model. The exception to that was the low Reynolds number case ($1x10^4$) in the adiabatic validation, where the SST model more closely matched the Manglik and Bergles correlation [15]. However, since fusion relevant experiments will be using much greater Reynolds numbers, this does not weigh heavily on the model selection. The Nusselt number calculations were more sensitive to the choice of turbulence model. The k-epsilon based models yielded results closer to the Manglik and Bergles correlation [15], where SST greatly overpredicted the correlation. The SST model also overpredicted the other legacy correlations investigated. While the k-epsilon based models were close to the Gambill et al. correlations [17].

An evaluation matrix was completed for the standard turbulence models (k-eps, RNG k-eps, and SST). The models were compared across seven categories including how the friction factor and Nusselt number results from each model compared to the Manglik and Bergles correlations [15] as well as the Gambill et al. correlation [17] for the Nusselt number. The Gambill et al. correlation [17] was included as a category because its experimental parameters were closer to those investigated in the validation portions. Other categories included near-wall resolution, freestream resolution, use in computational twisted tape literature, and computational cost. The standard k-epsilon turbulence model scored highest in the evaluation matrix. The score was impacted most by its similarity to the Gambill et al. correlation [17], freestream mesh resolution, and computational cost. The author originally expected that the SST model would outperform the k-epsilon based models because of its capability to refine down to the wall. However, the k-epsilon model yielded global results that were closest to the correlations at a much lower computational cost than SST. Furthermore, the k-epsilon model allowed for a more refined freestream mesh resolution than the RNG k-epsilon model. Thus, the k-epsilon model will be utilized moving forward.

## 4.5. Summary of Key Conclusions

The computational validation and local flow investigation yielded a wide range of results across the adiabatic and diabatic studies. The key conclusions from these sections are summarized below:

- Global parameter calculations, such as the Fanning friction factor and Nusselt number, were shown to be credible when compared to legacy twisted tape correlations for both adiabatic and diabatic investigations [13-17, 22]. Flow predictions were qualitatively similar to legacy flow visualization experiments with both air and water flow [22, 23].
- The friction factor was less sensitive to the choice of turbulence model at higher Reynolds number flows. Various turbulence models resulted in a wider range of friction factors at lower Reynolds numbers for the adiabatic cases, and the results were clustered together as the Reynolds number was increased. The diabatic results were in agreement with this. The diabatic friction factors were clustered together for the higher Reynolds numbers investigated.
- The Nusselt number was shown to be more sensitive to the choice of turbulence model than the friction factor. A large variation was noted across the different models investigated. However, in all cases, a better thermal performance was noted for higher Reynolds numbers and heat fluxes.
- The curvature correction method by Spalart and Shur appeared to have more of an effect at lower Reynolds number flows [47]. At higher Reynolds numbers, the addition of the curvature correction coefficient (as implemented in this work) did not appear to have a significant impact on the solution for both adiabatic and diabatic studies.
- Fully developed flow was not observed as the flow patterns continued to change downstream. This variation occurred for the adiabatic and diabatic investigations as well as the transient mesh refinement study. Furthermore, the flow patterns varied for each turbulence model investigated. Even though the same key qualitative features were captured, more detailed flow visualization experiments are needed to

determine which turbulence model provides the most accurate representation of the twisted tape induced swirl flow.

- A fully mesh independent solution was not achieved with the transient mesh refinement study. Key qualitative features were captured with the transient solutions, and the global parameter reached a constant value. However, the local flow information continued to change as the mesh was refined. This study revealed the need for a detailed transient study in which CFD best practices are developed for twisted tape induced swirl flow.
- The secondary circulation results in so-called "inflow" regions where the boundary layer fluid is reinjected into the freestream. These regions were noted in all cases investigated in the adiabatic and diabatic studies. Inflow regions were shown to correspond to regions of low wall shear, low heat transfer coefficients, and high surface temperatures. Thus, the inflow regions may be likely candidates for early burnout in twisted tape devices.
- Investigation of wall shear stress contours revealed apparent "striping" that develops in twisted tape induced swirl flow. This striping was observed in the adiabatic and diabatic investigations as well as the transient mesh refinement study. The so-called stripes represent the inflow regions along the water-tube interface. The number and location of the stripes shifts along the length of the test section.

To this author's knowledge, the connection between the inflow regions to potential burnout locations and the wall shear stress striping has not been cited in the twisted tape induced swirl flow literature.

# Chapter 5: Parametric Study for Various Twist Ratios

A parametric study was performed with the general twisted tape geometry to study the effect of various twist ratios on the diabatic solutions. The results were compared to both legacy correlations and experimental data for multiple twist ratios. Key local flow features, such as the inflow regions and wall shear striping, were further investigated with this study, and the effects of the twist ratio on the local flow information was discussed.

## 5.1. Model Geometry and Setup

The parametric study was performed with the model and setup used for the diabatic validation as discussed in Section 4.1.2. The study was performed for two moderate Reynolds numbers and heat fluxes as shown in Table 4.1 for four twist ratios: y=2, 3, 4.5, and 6 along with y=∞ which represents a straight tape. As discussed in Chapter 2, the twist ratio characterizes the severity of the pitch, and it represents the length to diameter ratio of one 180° twist. Portions of the twisted tape geometries are shown in Figure 5.1 to illustrate the difference between the various twist ratios (excluding y=∞). As seen in Figure 5.1, a smaller twist ratio results in a tighter twist. This results in more vigorous mixing and swirling with faster total velocities. By contrast, a larger ratio yields a more gradual twist, which results in comparatively less mixing and lower total velocities. The first twist ratio (y=2) was chosen because of its frequent use in the fusion community [3, 27, 53, 64, 65]. The ratios of y=3, 4.5, and 6 were selected to match the Manglik and Bergles experiments [19]. Lastly, the straight tape (y=∞) was included as a contrast to the swirling flow for the investigation of the flow patterns and wall shear stress. The straight tape global parameters were not directly compared to the rest of the twist ratios due to the phenomenological differences in the flow field.

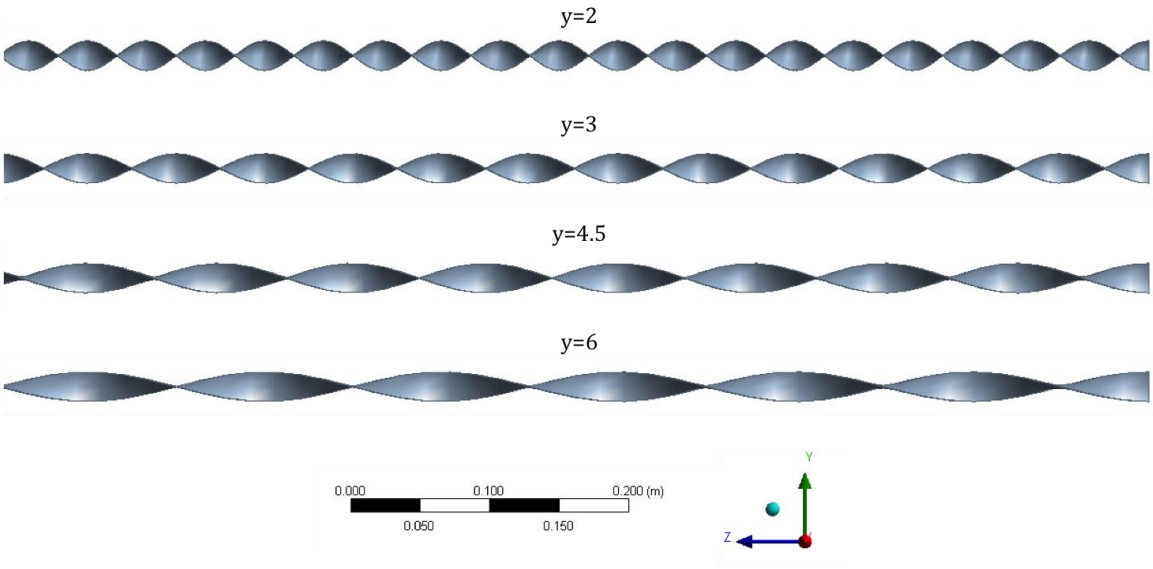


Figure 5.1: Twisted tape geometries at various twist ratios

## 5.2. Effect of Twist Ratio on Global Parameters

The global parameters including the Fanning friction factor and Nusselt number were investigated across the various twist ratios. The parameters were calculated in the same fashion as discussed in Section 4.2.2.

Figure 5.2 shows the effect of the twist ratio on the friction factor for various Reynolds numbers and applied heat fluxes. In general, the friction factor decreases with increasing twist ratios. Thus, the more gradual swirling motion induces a lower hydraulic resistance than the tighter twist. As seen in Figure 5.2, the higher Reynolds numbers yield slightly lower friction factors, which is similar to the results seen in Chapter 4. These reduced friction factors are not indicative of a lower pressure drop. Rather, they are due to a higher inlet axial velocity in the denominator. Furthermore, Figure 5.2 illustrates the limited impact of the Reynolds number and heat flux on the friction factor, which is in agreement with the diabatic results shown in Section 4.2.2.

The effect of the twist ratio on the Nusselt number is shown in Figure 5.3. Similarly to the friction factor, the Nusselt number decreases with an increasing twist ratio. Figure 5.3 also indicates that the thermal parameter is more sensitive to the twist ratio at higher Reynolds numbers, where a greater change in the Nusselt number is realized. Furthermore, Figure 5.3 is in agreement with the diabatic results discussed in Section 4.2.2 where the Nusselt number was more sensitive to the Reynolds number and heat flux compared to the friction factor.

## 5.3. Comparison of Global Parameters to Legacy Works

### *5.3.1. Comparison to Legacy Thermal-Hydraulic Correlations*

The global parameters were first compared to legacy correlations, and in general, the computational results were within the range of the legacy results. The Fanning friction factor was compared to the legacy correlations shown in Table 4.2, where the correlations were corrected to the diabatic condition using Equation 4.9.

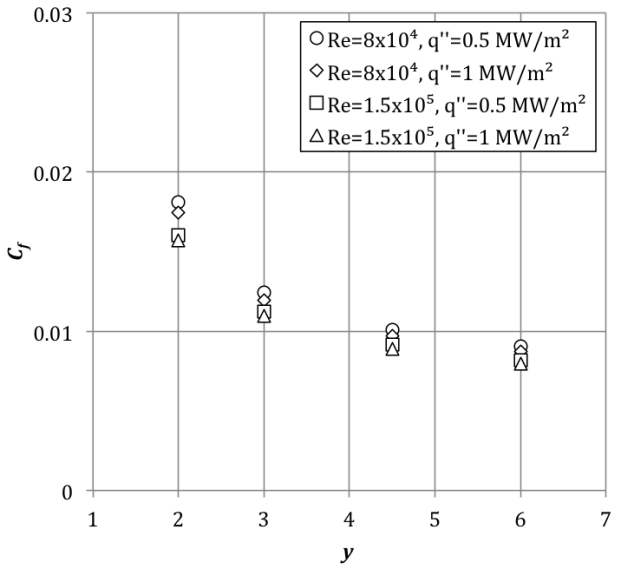


Figure 5.2: Effect of twist ratio on the Fanning friction factor for various Reynolds numbers and heat fluxes

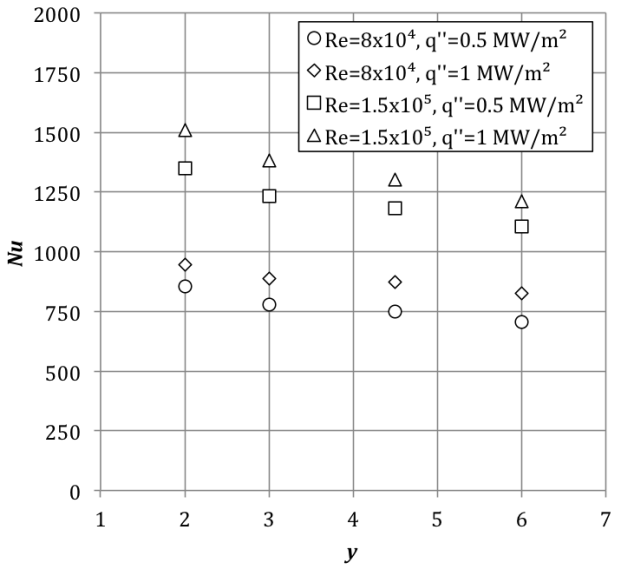


Figure 5.3: Effect of twist ratio on the Nusselt number for various Reynolds numbers and heat fluxes

Figure 5.4 shows the comparison between the simulations and the legacy correlations. The friction factor generally falls between the Manglik and Bergles and Ibragimov et al. correlations [15, 16]. The smallest twist ratio is closer to the Manglik and Bergles correlation, where the higher ratios are closer to the Ibragimov et al. correlation. Figure 5.4 also indicates that the Gambill and Bundy correlation [13] is not greatly affected by the twist ratio. As shown in Figure 5.5, the Nusselt number was compared to the correlations listed in Table 4.4. In general, the Nusselt number is in best agreement with the Gambill et al. correlation, and the simulations align closely with Gambill et al. [17] for the higher heat flux. For the lower heat flux, the computational results fall between the Manglik and Bergles correlation and Gambill et al. [15, 17].

### *5.3.2. Comparison to Legacy Experimental Data*

The effect of the twist ratio was further investigated with comparison to experimental data from two legacy experiments in the twisted tape literature. Gambill et al. investigated single-phase heat transfer coefficients as part of their experiments. The authors presented the ratio of the "experimental mean vortex" and the "equivalent mean axial-flow" heat transfer coefficients as a function of the twist ratio squared ($y^2$). The coefficients were evaluated at the same mean temperature and mass flow rate. The authors state that this ratio is equivalent to the Nusselt number ratio [17]. Figure 5.6 shows the comparison of the Nusselt number ratio between the computational and experimental results. The "mean vortex" Nusselt number ($Nu_s$) was calculated using Equation 4.5, and the "equivalent mean axial-flow" Nusselt number ($Nu_a$) was calculated using the Colburn equation for axial flow as suggested by Gambill et al. such that

$$Nu_a = 0.023 Re_D^{4/5} Pr^{1/3} \tag{5.1}$$

where the Reynolds number was based on the empty tube diameter and all fluid properties were calculated at the length averaged mean temperature [58].

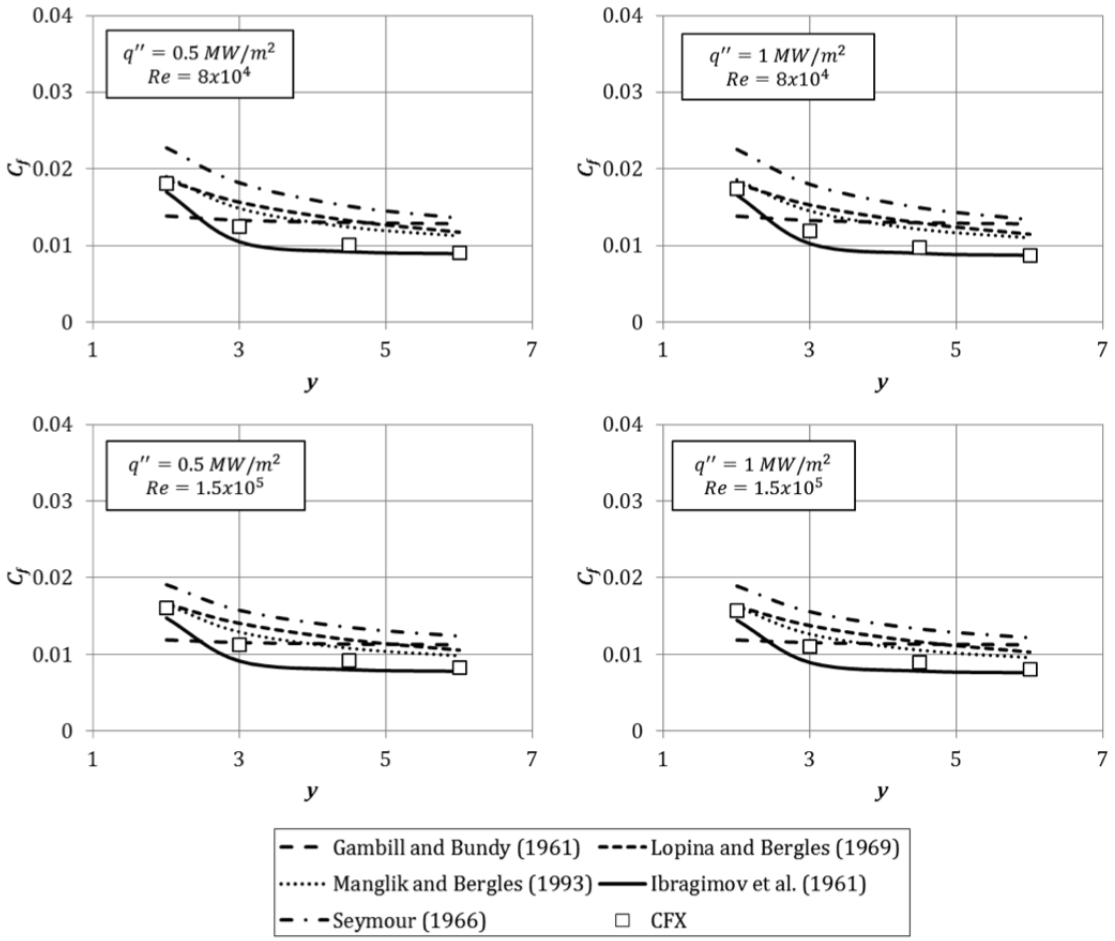


Figure 5.4: Fanning friction factor comparison of simulation results to legacy correlations [13-16, 22] for various twist ratios across multiple heat fluxes and Reynolds numbers

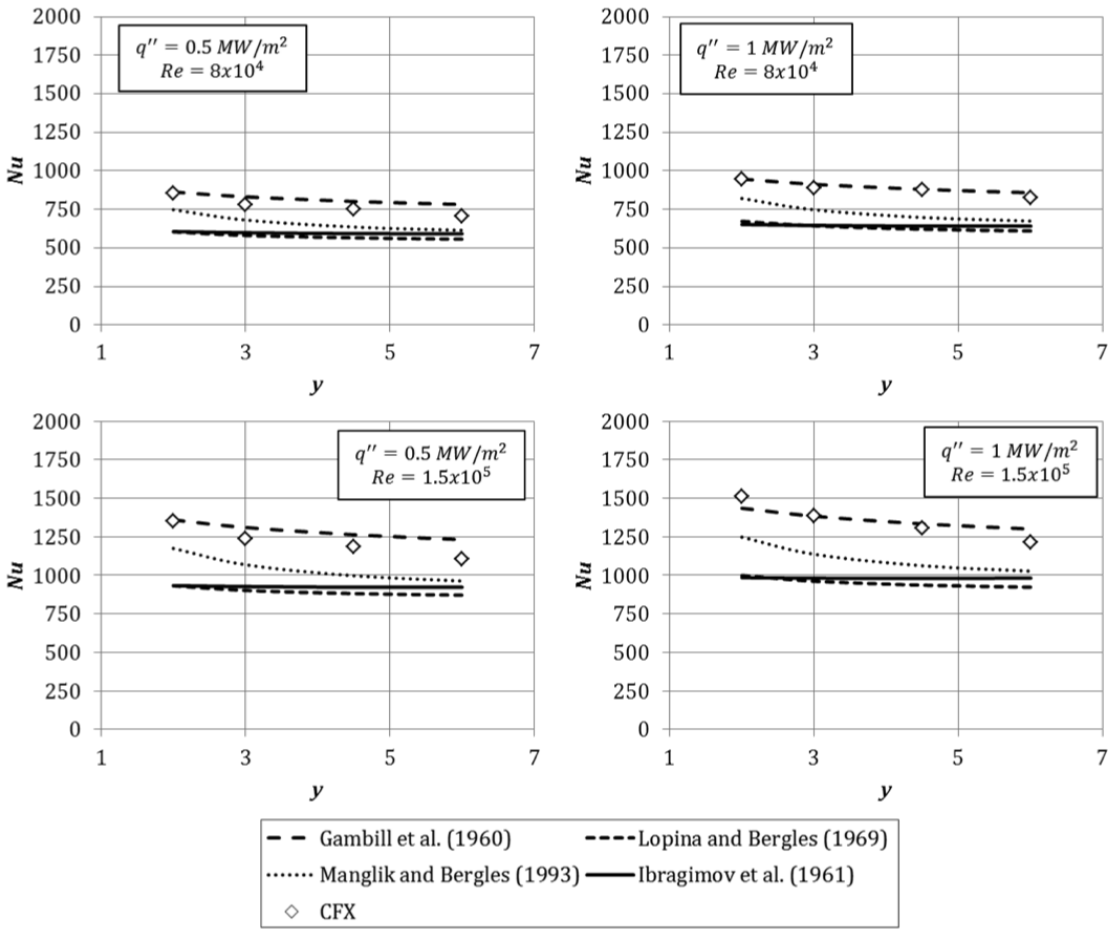


Figure 5.5: Nusselt number comparison of simulation results to legacy correlations [14-17] for various twist ratios across multiple heat fluxes and Reynolds numbers

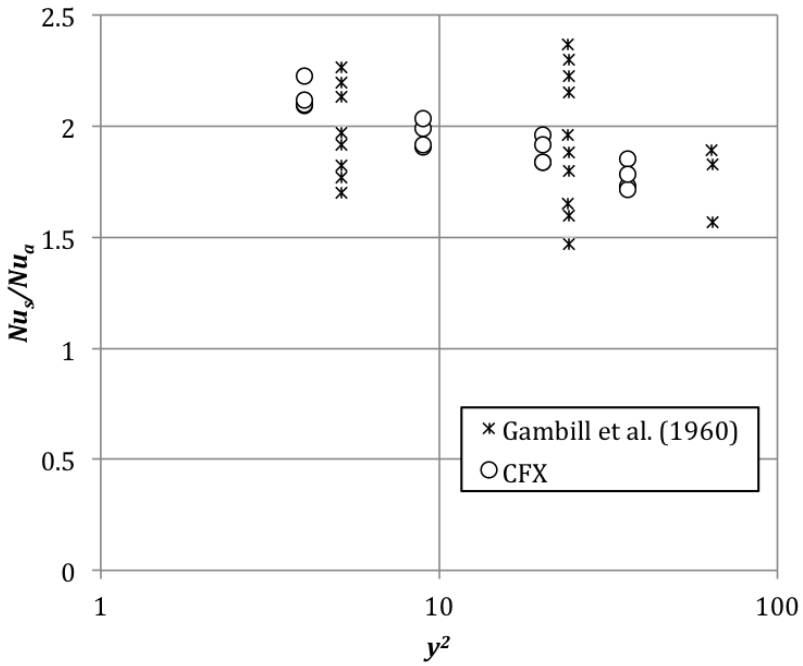


Figure 5.6: Ratio of the swirl to the equivalent axial Nusselt number compared to the experimental data of Ref. [17]

Fluid properties were calculated using the IAPWS-IF97 formulation as discussed in Ref. [54]. The experimental data was extracted from Ref. [17] and was plotted along with the Nusselt number ratio for the computational results. As can be seen in Figure 5.6, the Nusselt number ratio is in agreement with the experimental data. While the twist ratios vary, the computational results are within the experimental range represented in Ref. [17].

Lopina and Bergles investigated the isothermal swirl flow friction factor by plotting the ratio of the swirl friction factor to the axial flow friction factor [14]. In their work, the empty tube heated data was corrected to the isothermal condition by the factor $(\mu_b/\mu_w)^{0.35}$. Furthermore, the Lopina and Bergles data was presented as a function of the hydraulic diameter rather thn the empty tube diameter.

In order to compare to the Lopina and Bergles data, the computational results had to be corrected to the isothermal condition, and the swirl flow friction factor was calculated with the hydraulic diameter. The isothermal swirl flow friction factor ($C_{f_{s,iso}}$) was calculated using Equations 4.1 and 4.8, where the empty tube diameter was replaced with the hydraulic diameter such that

$$\left(C_{f_{s,iso}}\right)_h = \left(C_{f_s}\right)_h \left(\frac{\mu_b}{\mu_w}\right)^{0.35(d_h/d)} \tag{5.2}$$

$$\left(C_{f_s}\right)_h = \frac{\Delta P}{\left(\frac{L}{d_h}\right)(2\rho_m v_{in}^2)} \tag{5.3}$$

The axial flow friction factor (see Equation 5.5) was calculated with the Petukhov correlation as cited in Ref. [58] and was corrected to the isothermal condition using the factor suggested by Lopina and Bergles [14].

$$C_{f_{a,iso}} = C_{f_a}\left(\frac{\mu_b}{\mu_w}\right)^{0.35} \tag{5.4}$$

$$C_{f_a} = 0.25\left(0.790\ln\left(Re_{D,m}\right) - 1.64\right)^{-2} \tag{5.5}$$

Lopina and Bergles presented their results along with those of six other experimental studies as a function of the twist ratio squared. The experimental data was extracted for all

studies from Ref. [14], and the ratio for the computational results was plotted against the experimental results as shown in Figure 5.7. The computational results are plotted for all cases as shown in Table 4.1. Overall, there is good agreement between the computational and experimental results. The friction factor ratio generally falls within the range of the experimental data as given in Ref. [14].

## 5.4. Investigation into Local Flow Information

### *5.4.1. Flow Patterns and Temperature Contours*

The impact of various twist ratios was further investigated at the local level with flow patterns and temperature contours. The contours were investigated at three axial locations near the start, middle, and end of the twisted tape where the tape was in a horizontal orientation. Because different twist ratios were implemented, the horizontal orientation did not occur at the same axial location for each case. Table 5.1 shows the axial locations corresponding to the start, middle, and end positions for each twist ratio. Figure 5.8 shows the total velocity contours at the three positions for Re=8x10$^4$ and $q''$=1 MW/m$^2$ for the various twist ratios. For this Reynolds number, there are inflow regions and secondary flow observed at some point along the test section for all twist ratios (excluding the straight tape). Fully developed flow was not reached for these cases. The straight tape case (y=∞) shown in Figure 5.8 serves as a contrast to the swirling flow patterns. As expected, there is no swirling motion, and the flow appears to reach a fully developed state. Figure 5.8 also illustrates the difference between the twist ratios at each plane. The inflow regions near the exit appear to be less pronounced for the smallest twist ratio and more pronounced for larger twists.

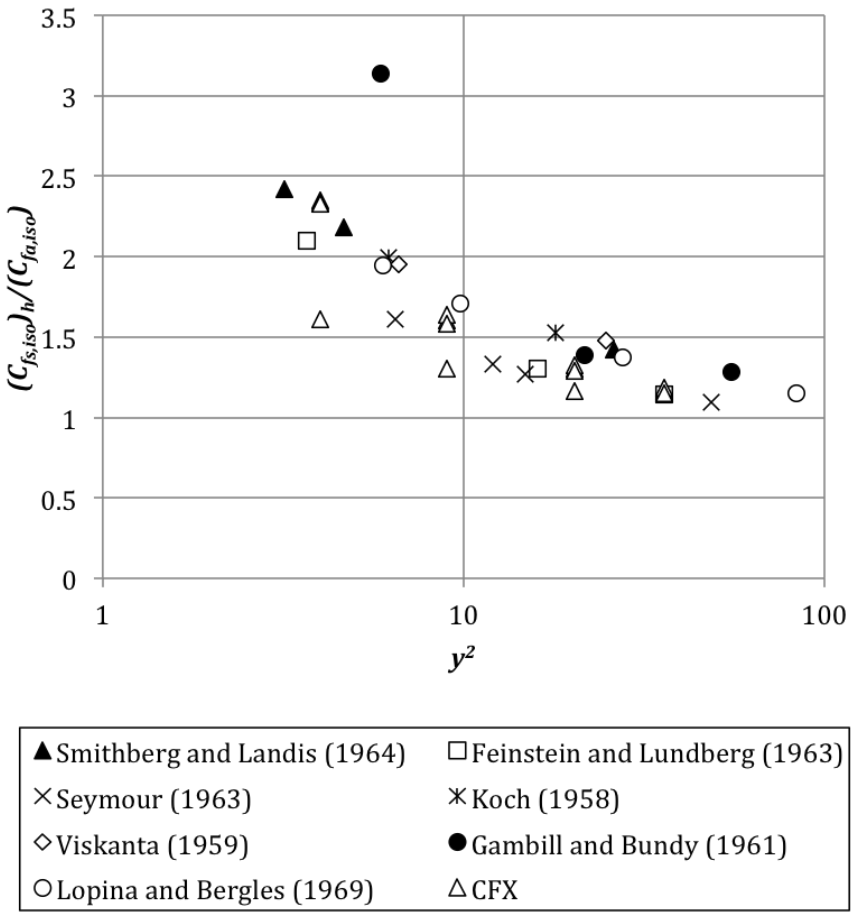


Figure 5.7: Ratio of the isothermal swirl flow friction factor to the axial friction factor compared to experimental data as cited in Ref. [14] [13, 14, 22, 23, 66, 67]

Table 5.1: Axial locations selected for the local flow investigation

| Test Section Location | Plane | y=2 Axial Location [m] | y=3 Axial Location [m] | y=4.5 Axial Location [m] | y=6 Axial Location [m] | y=∞ Axial Location [m] |
|---|---|---|---|---|---|---|
| **Start** | 1 | 1.54614 | 1.55673 | 1.57262 | 1.58850 | 1.55673 |
| **Middle** | 2 | 3.07110 | 3.08169 | 3.09758 | 3.11346 | 3.08169 |
| **End** | 3 | 4.55370 | 4.54311 | 4.52723 | 4.51134 | 4.54311 |

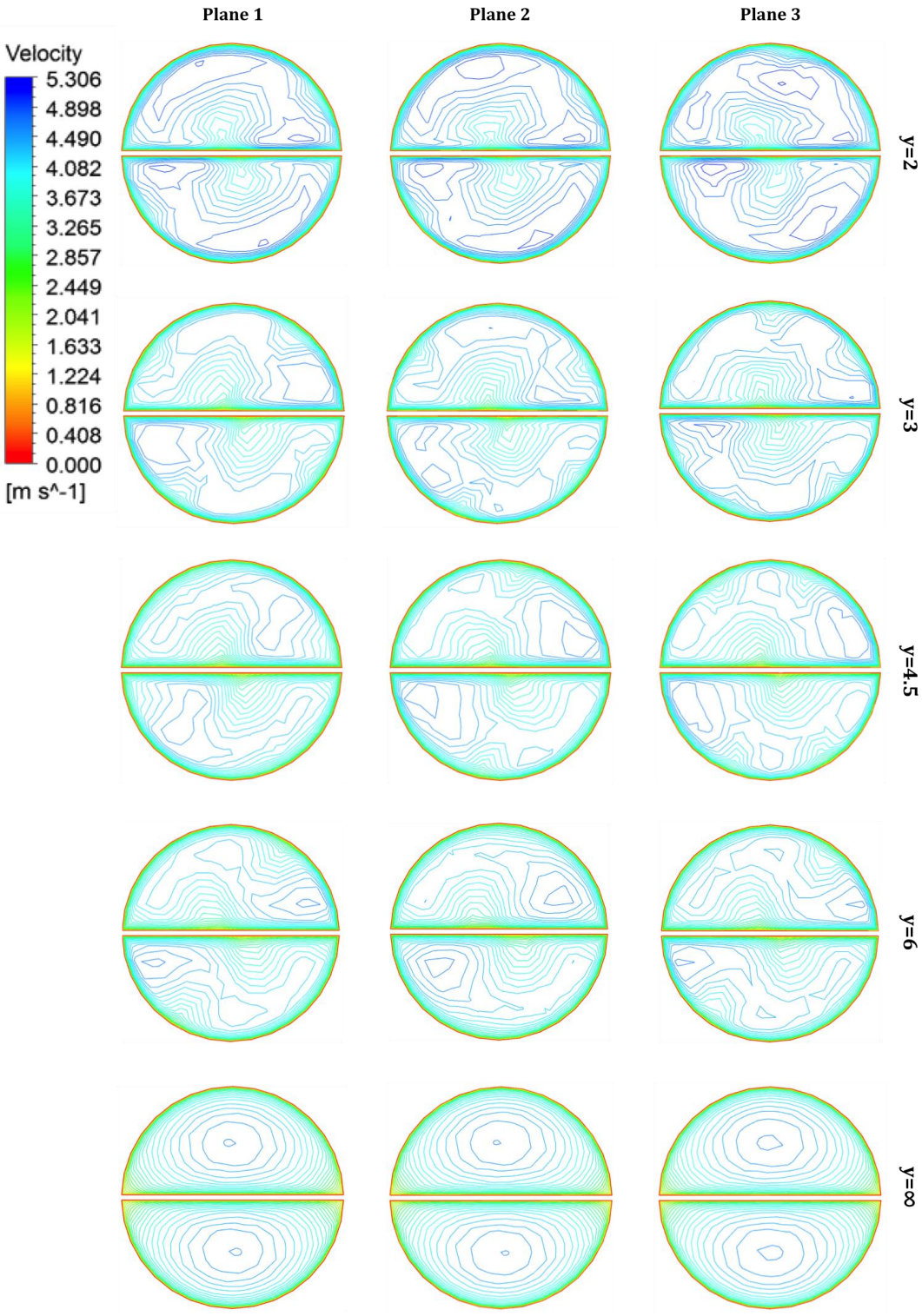


Figure 5.8: Comparison of diabatic total velocity contours as the flow moves downstream for various twist ratios (Re=8x10$^4$, $q''$=1 MW/m$^2$)

The local temperature contours were also investigated at multiple axial locations and across various twist ratios. The temperature contours were investigated at two axial locations near the middle and end of the test section (as shown in Table 5.1). The contour is not presented for the start of the test section because the temperature was nearly constant at that position. Figure 5.9 shows the temperature contours for Re=8x$10^4$ and $q''$=1 MW/$m^2$ for a twist ratio of y=2. As expected, the temperature increases as the fluid moves downstream. Similarly to the initial diabatic investigation (see Section 4.3.2), the maximum temperature is greater than saturation (Tsat≈100°C) for this Reynolds number and heat flux combination. This occurs near the end of the test section.

In fusion relevant geometries, the test section would be much shorter, and thus, boiling would not be induced for this case. Furthermore, higher pressures would be implemented at fusion relevant conditions, which would increase the saturation temperature and suppress boiling. Figure 5.10 shows the variation in the temperature contours across different twist ratios. Similar to the flow patterns shown in Figure 5.8, the temperature contours vary across each twist ratio investigated.

### *5.4.2. Further Investigation of Inflow Regions*

The secondary circulation in the twisted tape induced swirl flow results in inflow regions which were shown to correspond to regions of low wall shear stress, low heat transfer coefficients, and high surface temperatures in Chapter 4. The impact of the twist ratio on this phenomenon is further investigated in this section.

The effect of the twist ratios can be qualitatively viewed by comparing the velocity and temperature contours at a particular axial location. The velocity and temperature contours were previously compared for a twist ratio of y=3 (see Figure 4.10). This comparison revealed that hot spots appeared to correspond to inflow regions. The connection was further investigated for various twist ratios in this study. Figure 5.11 shows the contours for Re=1.5x$10^5$ and $q''$=1 MW/$m^2$ at a plane near the exit region for various twist ratios. As shown in Figure 5.11, the connection between the inflow regions and hot spots still occurs across various twist ratios (as indicated by arrows).

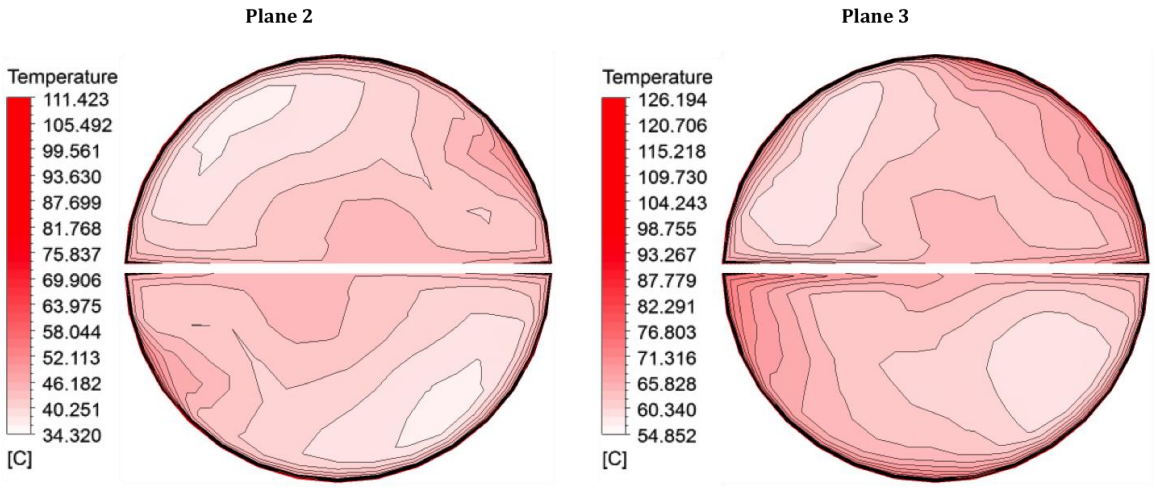


Figure 5.9: Comparison of temperature contours as the flow moves downstream (Re=8x10$^4$, $q''$=1 MW/m$^2$, y=2)

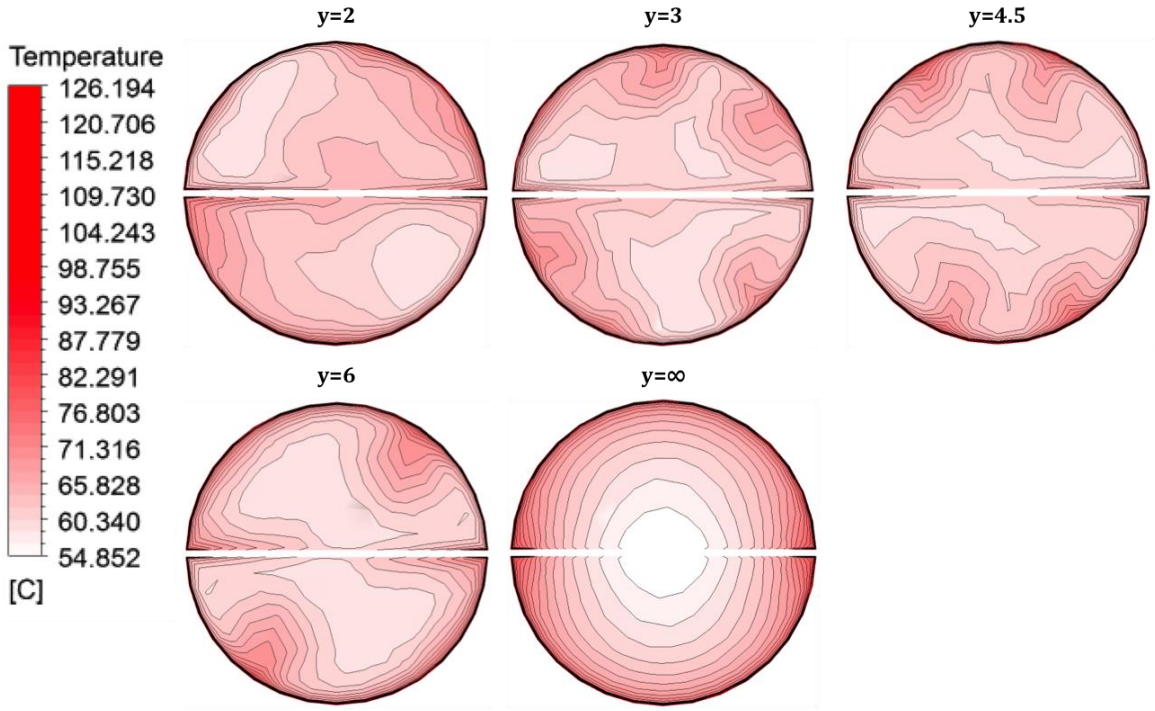


Figure 5.10: Comparison of temperature contours for various twist ratios at a plane near the exit region (Plane 3 in Table 5.1, Re=8x10$^4$, $q''$=1 MW/m$^2$)

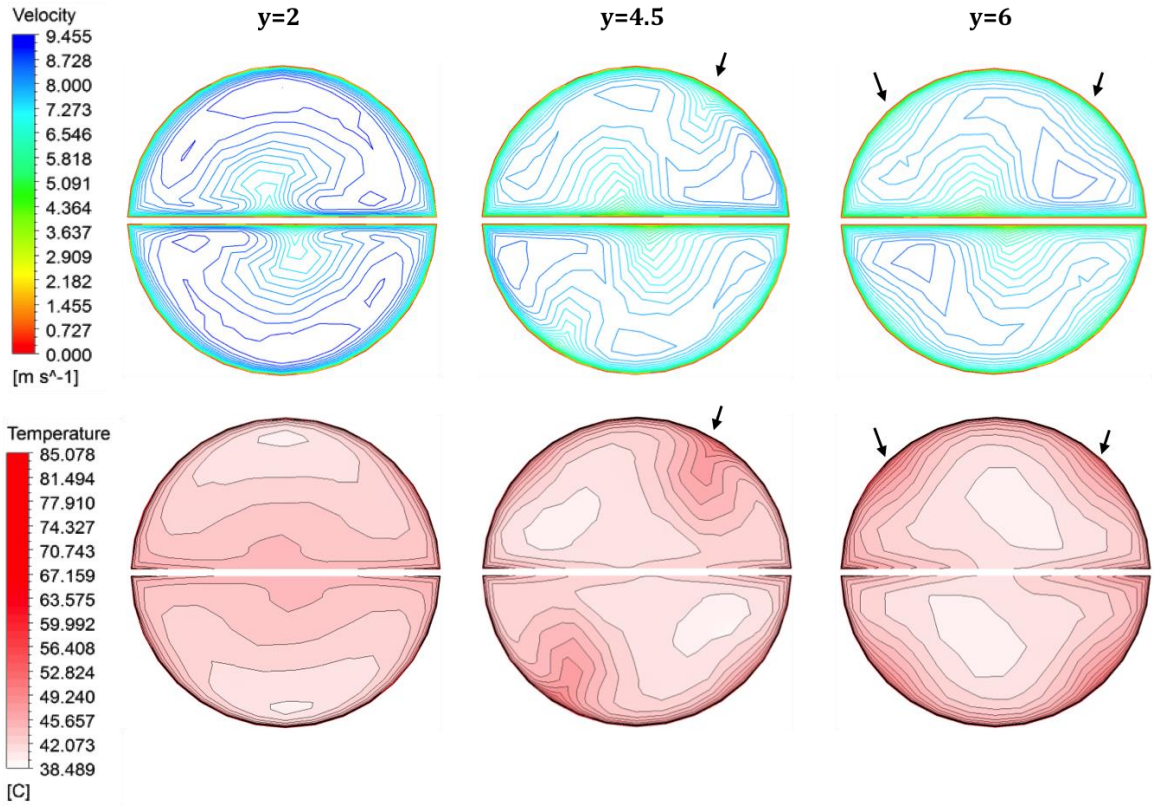


Figure 5.11: Total velocity (top) and temperature (bottom) contours at a plane near the exit region (Plane 3 in Table 5.1, Re=1.5x$10^5$, $q''$=1 MW/$m^2$)

The connection between the wall shear stress and potential burn out locations was investigated further across various twist ratios. The wall shear stress, wall heat flux, and surface temperature were exported along the full perimeter, including the water-tape and water-tube interfaces, at a plane near the exit region (as indicated by Table 5.1). The wall heat flux, heat transfer coefficient, wall shear stress, and surface temperature were plotted against the entire perimeter (including water-tube and water-tape interfaces) as shown in Figure 5.12. The wall heat flux is shown in Figure 5.12, which reveals that the heat flux goes to nearly zero along the water-tape interface. A similar general trend is seen across all twist ratios with y=3 and y=4 showing greater decreases in the wall heat flux along the water-tube interface.

Figure 5.13 shows the comparison of the HTC for different twist ratios. A negative HTC occurs at some point along the water-tape interface for the different twist ratios. This negative HTC is due to heat transferring from the hot water to the cool tape. There is a stark contrast between the straight tape and the twisted tapes at the water-tape interface, where the HTC has significant valleys for the straight case. The magnitude of the HTC varies with the twist ratios. Aside from the straight tape, the highest magnitudes at the water-tape interface occur with the y=3 twist ratio, while the lowest magnitudes occur with the smallest twist ratio (y=2). The inflow regions along the outer perimeter are indicated by dips in the HTC. As shown in Figure 5.13, the straight tape case shows no indication of inflow regions (as expected), while the other cases show varying levels of decreased HTC along the water-tube interface.

Figure 5.14 shows the wall shear stress along the full perimeter. There is a wide variation for the shear stress across the various twist ratios, and the straight tape provides a stark contrast to the twisted tapes. In the case of the straight tape, the wall shear stress dips at the corners rather than the water-tape or water-tube interfaces, and it experiences a gradual increase in the stress between the corner locations. For the twisted tapes, the greatest decreases in the wall shear stress occur at the water-tape interface.

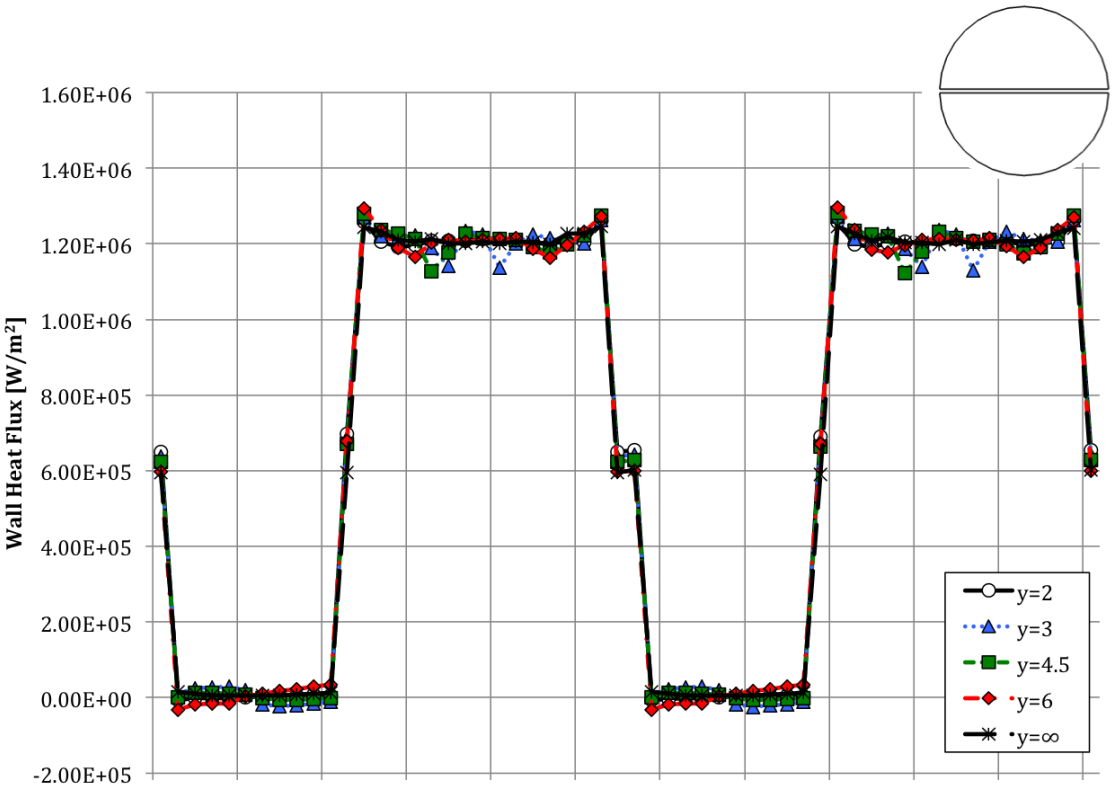


Figure 5.12: Wall heat flux for various twist ratios at a plane near the exit region (Plane 3 in Table 5.1, Re=1.5x$10^5$, $q''$=1 MW/$m^2$)

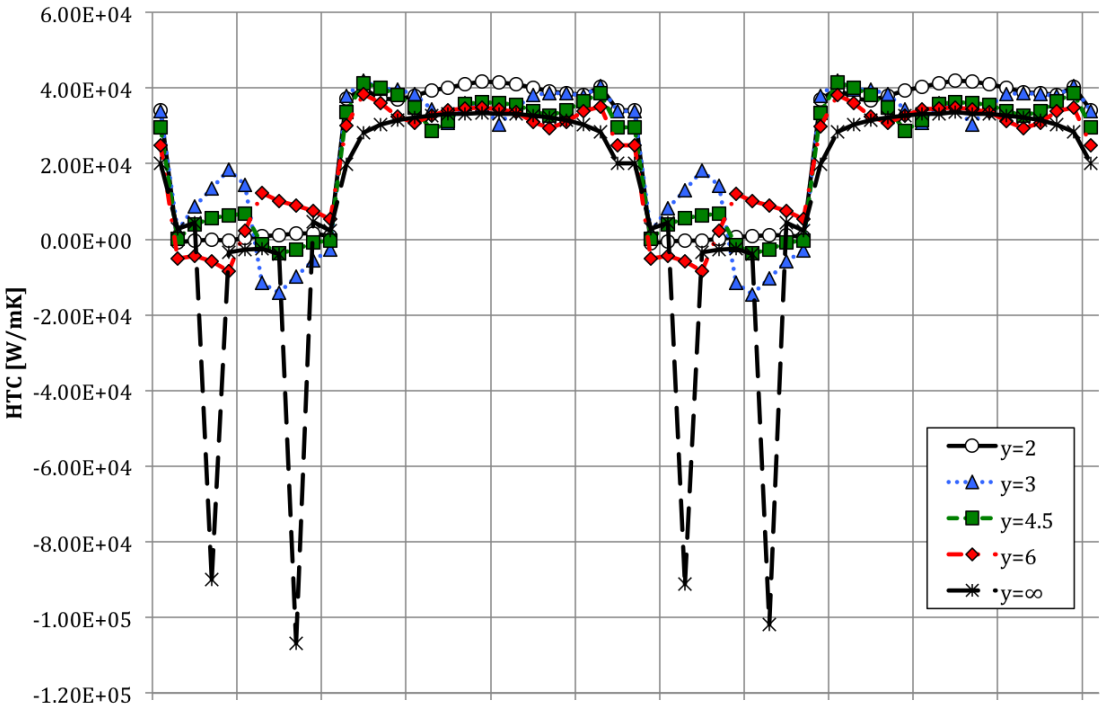


Figure 5.13: Heat transfer coefficient for various twist ratios at a plane near the exit region (Plane 3 in Table 5.1, Re=1.5x$10^5$, $q''$=1 MW/$m^2$)

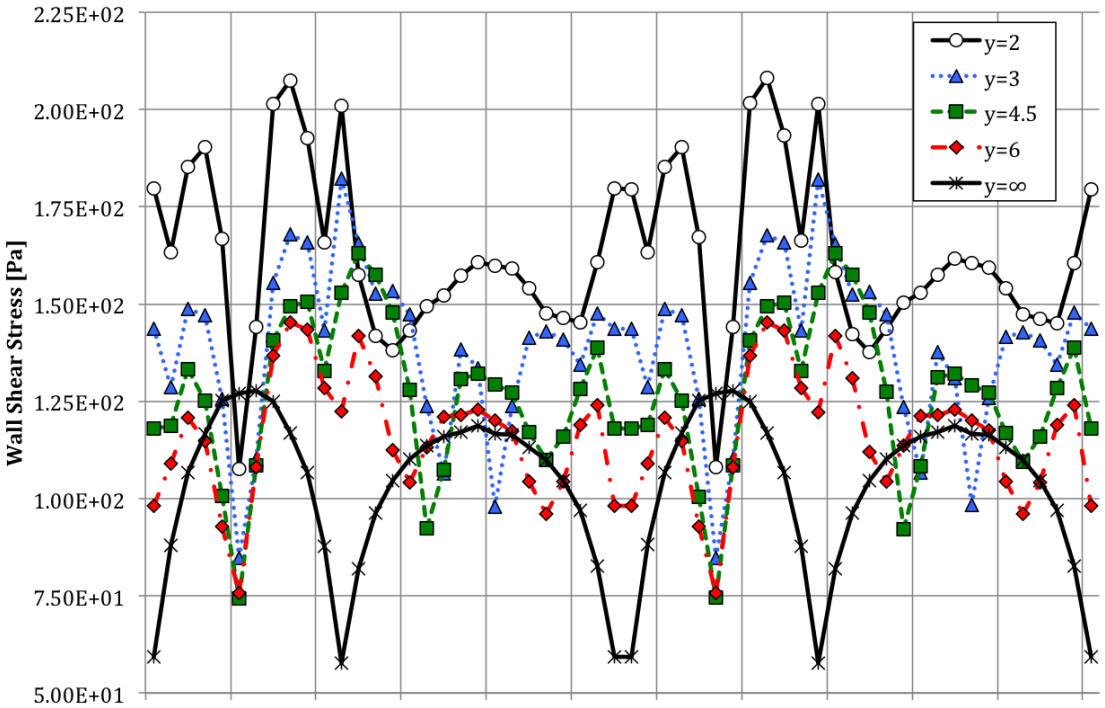


Figure 5.14: Wall shear stress for various twist ratios at a plane near the exit region (Plane 3 in Table 5.1, Re=1.5x$10^5$, $q''$=1 MW/$m^2$)

Generally, the stress appears to decrease as the tape twist increases with the smallest twist ratio (y=2) having the overall largest wall shear stress magnitude and the largest twist ratio (y=6) showing the lowest magnitudes (although not at every point). Along the water-tube interface, the smallest twist ratio has the smoothest curve, which is in agreement with the flow pattern shown in Figure 5.11. Similarly, the medium ratios (y=3 and y=4.5) appear to have more pronounced inflow regions at the water-tube interface in Figures 4.10 and 5.11. This is confirmed by Figure 5.14 where the dips in the wall shear stress are more pronounced for those twist ratios. Lastly, the surface temperature is shown in Figure 5.15. In general, the lowest temperatures occur at the water-tape interface, while the peak temperatures correspond with dips in the wall shear stress and HTC for the twisted tapes. In contrast, the straight tape case yields peak temperatures at the corners. Overall, the smallest twist ratio (y=2) yields lower surface temperatures along the water-tube interface and slightly higher temperatures at the water-tape interface. There is little difference between the other twist ratios at the water-tape interface. However, at the water-tube interface, the largest twist ratio (y=6) appears to yield mostly higher surface temperatures.

The local wall shear stress can be further visualized by plotting the contours on the water-tube and water-tape interfaces. Figure 5.16 shows the wall shear stress contours for all of the twist ratios investigated for Re=1.5x$10^5$ and $q''$=1 MW/$m^2$. The contours are shown for half of the water domain in the swirling region. For easier viewing, the geometry is cut into sections; the cut planes and locations are indicated in Table 4.7. Figure 5.16 reveals the striping that occurs in twisted tape induced swirl flow. The striping along the water-tube interface occurs in all cases at some point in the geometry, and it is also clearly indicated on the water-tape interface. As the flow moves downstream, the wall shear stress appears to smooth out along the water-tube interface for the smallest and largest twist ratios (y=2 and 6). Furthermore, the contours give an indication for the wall shear stress magnitudes across different twist ratios. The shear stress magnitudes increase as the twist ratio decreases. Figure 5.17 shows a portion of the straight tape case as a contrast to the swirling flow. Note that the lowest wall shear stress occurs at the corners. This ultimately corresponds to hot spots at the corners for the straight tape case.

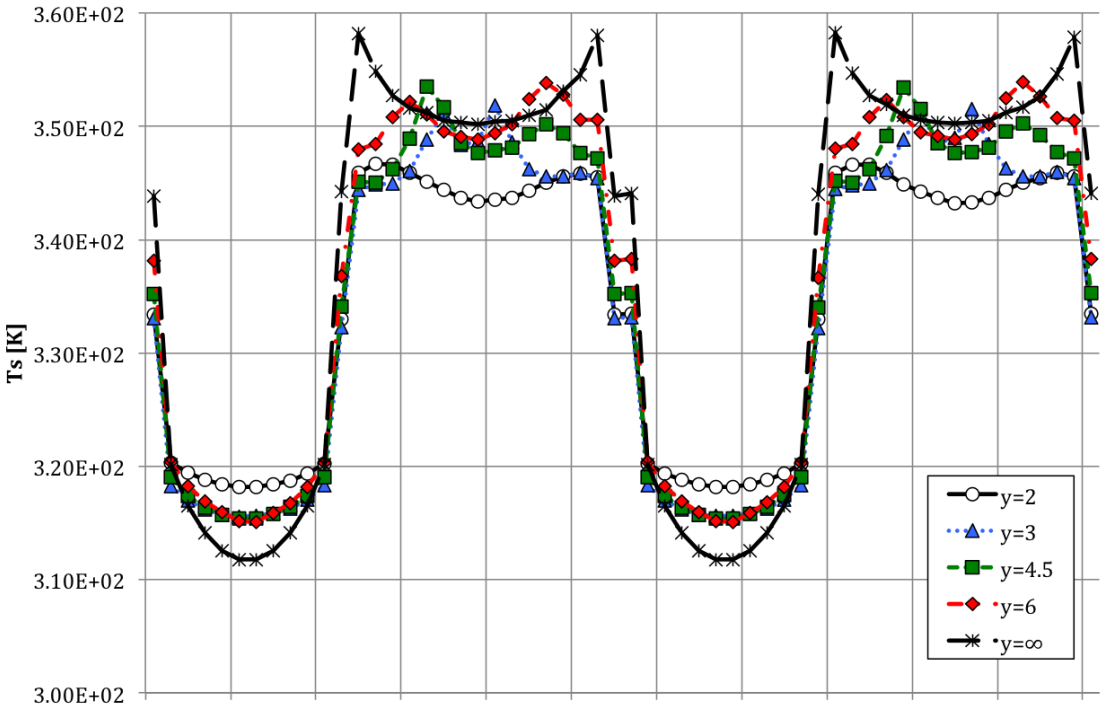


Figure 5.15: Surface temperature for various twist ratios at a plane near the exit region (Plane 3 in Table 5.1, Re=1.5x$10^5$, $q''$=1 MW/$m^2$)

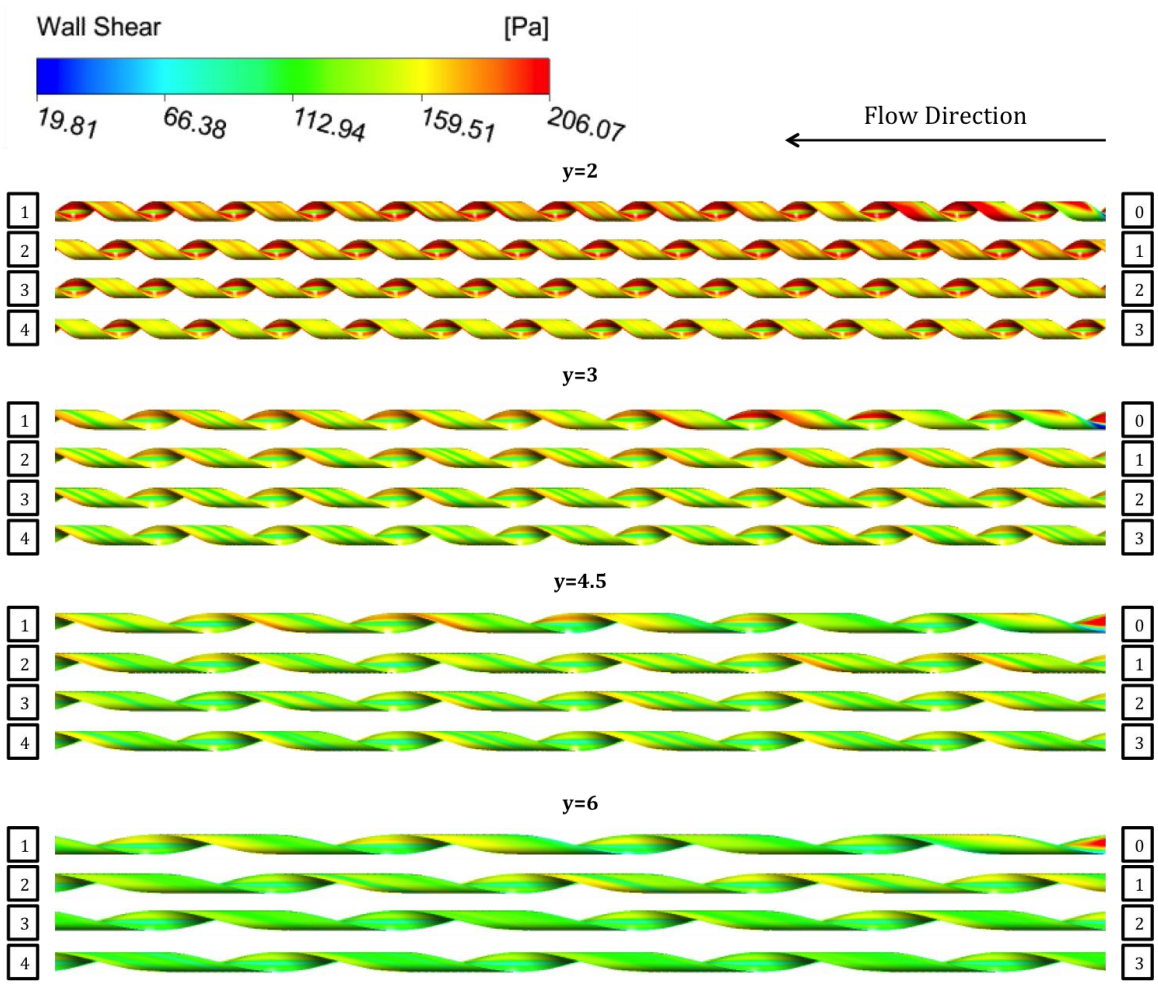


Figure 5.16: Wall shear stress contours for various twist ratios where cut plane locations are shown in Table 4.7 (Re=1.5x$10^5$, $q''$=1 MW/$m^2$)

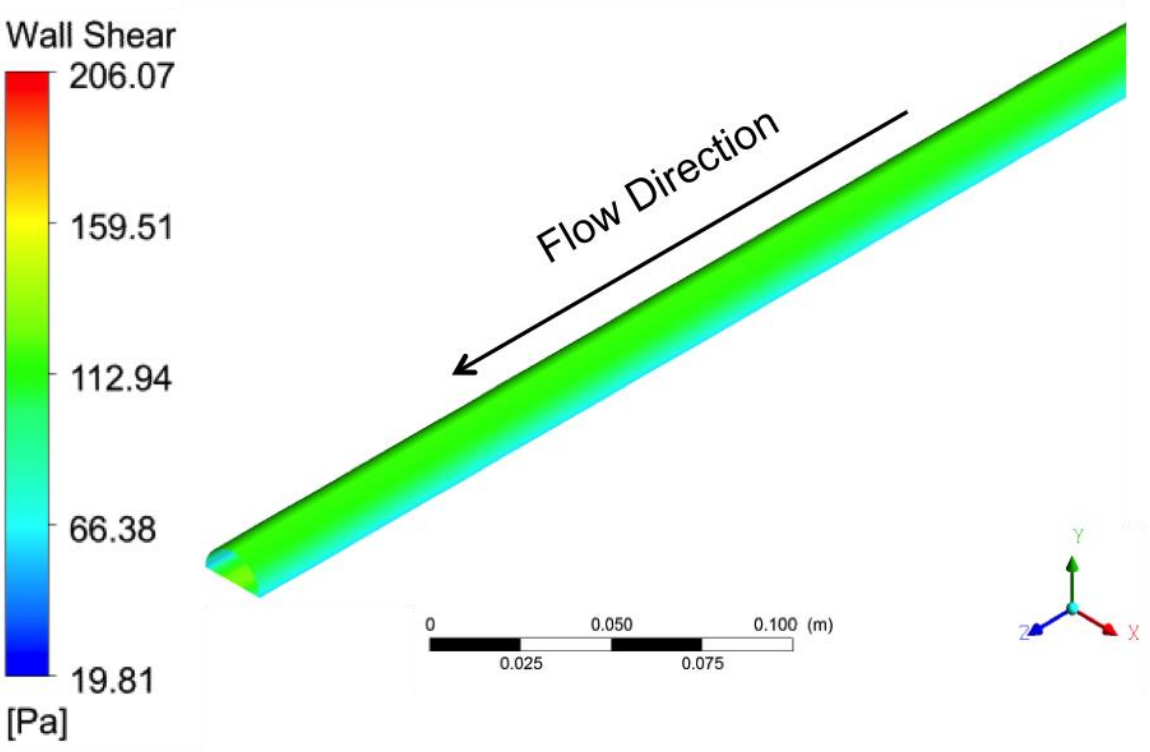


Figure 5.17: Wall shear stress contour for the straight tape case near the exit region (Re=1.5x$10^5$, $q''$=1 MW/$m^2$)

## 5.5. Summary of Key Conclusions

The parametric study revealed a variety of results across a range of twist ratios. The key conclusions are summarized below:

- The global parameters, such as the Fanning friction factor and Nusselt number, were shown to be in good agreement with the legacy twisted tape correlations [13-17, 22]. Likewise, Nusselt number and friction factor ratios fell within experimental ranges when compared to legacy data [14, 17].
- The friction factor decreased with increasing twist ratios. Thus, a more gradual swirling motion resulted in a lower hydraulic resistance as opposed to a tighter twist. Additionally, the Reynolds number and applied heat flux had a minimal impact on the friction factor.
- A better thermal performance was noted for smaller twist ratios as the Nusselt number was shown to decrease with increasing twists. An improved performance was also seen for higher Reynolds numbers and higher heat fluxes. Furthermore, the Nusselt number was determined to be more sensitive to the thermal-hydraulic parameters when compared to the friction factor.
- Fully developed flow was not reached for the twist ratios investigated as the flow continued to change downstream. Similar qualitative features were captured for each twist ratio. However, the inflow regions near the exit appeared to be less pronounced for the smallest twist ratio and more pronounced for the larger twists.
- For the swirling flow, inflow regions were shown to correspond to regions of low wall shear stress, low heat transfer coefficients, and high surface temperatures. There were slight variations due to the different twist ratios. Generally, the wall shear stress appeared to decrease as the twist ratio increased. The smallest twist ratio had the largest overall wall shear stress magnitude, while the largest twist yielded the lowest magnitude. This corresponded to generally lower surface temperatures for the small twist ratio and higher temperatures for the large twist ratio.

- The straight tape was investigated for contrast to the swirling flow. As expected, there were no inflow regions for this case. The decreases in wall shear stress occurred at the corners rather than the water-tape or water-tube interfaces, which led to peak temperatures at these locations.
- Investigation of the wall shear stress contours revealed a striping pattern at some point in the geometry for all twist ratios. As the flow moved downstream, the wall shear stress appeared to smooth out along the water-tube interface for the smallest and largest twist ratios.

# Chapter 6: Computational Investigation at Fusion Relevant Conditions

*Portions of this work have been submitted for publication in the following peer-reviewed manuscript in which the author performed all analysis:*

*E. Clark, A. Lumsdaine, J. Boscary, H. Greuner, and K. Ekici, "Thermal-hydraulics modeling for prototype testing of the W7-X high heat flux scraper element," Submitted to Fusion Engineering and Design, 2017.*

## 6.1. Monoblock Plasma Facing Components

Esssentially, the monoblock concept consists of armor tiles with a hole drilled through them. A cooling tube is inserted into the hole and joined to the tiles. Monoblocks have widespread implementation in the fusion community and are often employed in multiple regions in magnetic confinement devices such as the divertor and the first wall. They are planned for use in ITER, W7-X, JT60-SA, and WEST, to name a few [3, 5, 68-70]. A mock-up of a monoblock PFC prototype intended for use in the W7-X divertor region is shown in Figure 6.1.

The armor material varies across magnetic confinement devices, but two materials are most prevalent in the field: carbon-carbon fiber composite (CFC) and tungsten. Tungsten is currently the most popular armor material in magnetic confinement devices and has been chosen for machines such as ITER and WEST [68, 70]. It is often chosen over CFC because carbon is prone to tritium retention, which leads to radiological considerations [71, 72]. Thus, for machines that intend to run deuterium-tritium (D-T) campaigns, tungsten has become the material of choice. However, some magnetic confinement experiments plan to run only deuterium-deuterium (D-D) campaigns, where the issue of tritium retention is not a factor. CFC armor is often used in these experiments and has been chosen for machines such as W7-X and JT60-SA [3, 5].

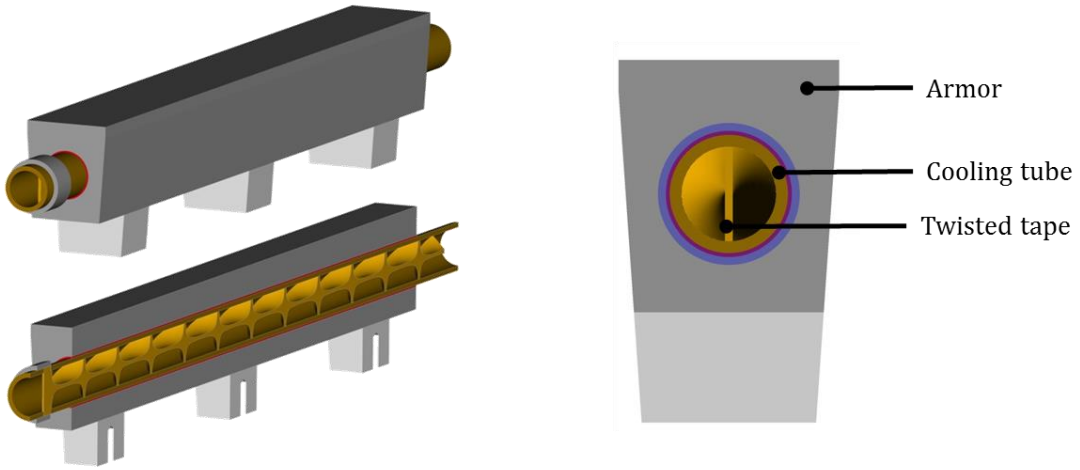


(a) (b)

Figure 6.1: Computer-aided drawing (CAD) of a W7-X monoblock plasma facing component prototype with (a) side and (b) axial viewpoints

In this chapter, the thermal-hydraulic parameters will be ramped up to fusion relevant conditions from the moderate ones utilized in Chapters 4 and 5. Because this work was generously funded by the Office of Fusion Energy Sciences for collaboration with the W7-X project, the fusion relevant investigation will focus on conditions that align with the interests of the W7-X experiment.

## 6.2. Computational Model

### *6.2.1. Monoblock Model Geometry*

The monoblock model was developed to match W7-X prototype testing of a single monoblock "finger" or "unit." Boscary et al. performed experiments on a single monoblock finger for the W7-X high heat flux scraper element [53]. As discussed in Ref. [3, 27, 53], the so-called scraper element was created to reduce heat loads on sensitive divertor regions. Currently, one scraper element is planned for each ten discrete divertor locations as seen in Figure 6.2. Each scraper element is made up of 24 monoblock units and is actively cooled with water. Previous studies were performed to determine the optimum flow configuration for the scraper elements. It was determined that the best design consisted of parallel flow into six different modules, which are composed of four monoblock units each [27]. The scraper element flow sequence is illustrated in Figure 6.3.

Each of the 24 monoblock units have armor made of carbon fiber reinforced carbon composite (CFC NB31). The CFC monoblocks are joined to a copper alloy (CuCrZr) tube by an active metal casting (AMC®) copper interlayer, which is 0.4 mm thick. The monoblock units have a total length of 247 mm, while the tubes are 307 mm long. The CuCrZr tubes have an inner diameter of 12 mm and a thickness of 1.5 mm, and they are equipped with a copper twisted tape insert. The twisted tape has a twist ratio of y=2, a tape thickness of 1 mm, and a length of 297 mm. Further specifications on the manufacturing of the monoblock geometry can be found in Ref. [53]. Figure 6.4 shows the monoblock model geometry from the side and axial viewpoints. The various components such as the CFC, AMC® interlayer, pipe, and water are indicated in the axial viewpoint.

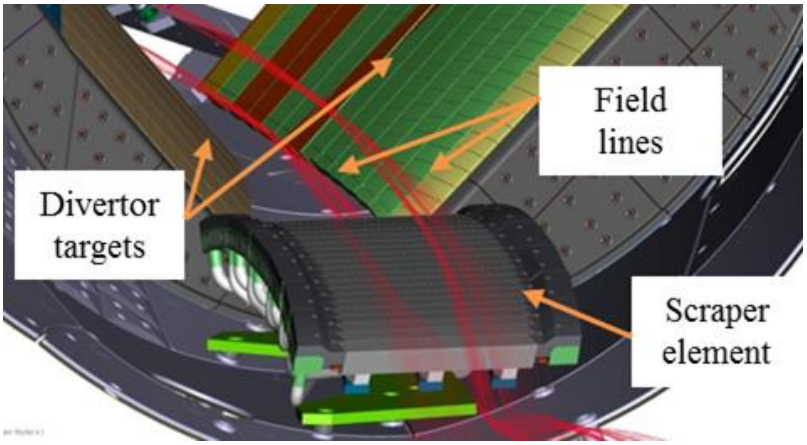


Figure 6.2: W7-X divertor region with scraper element [3]

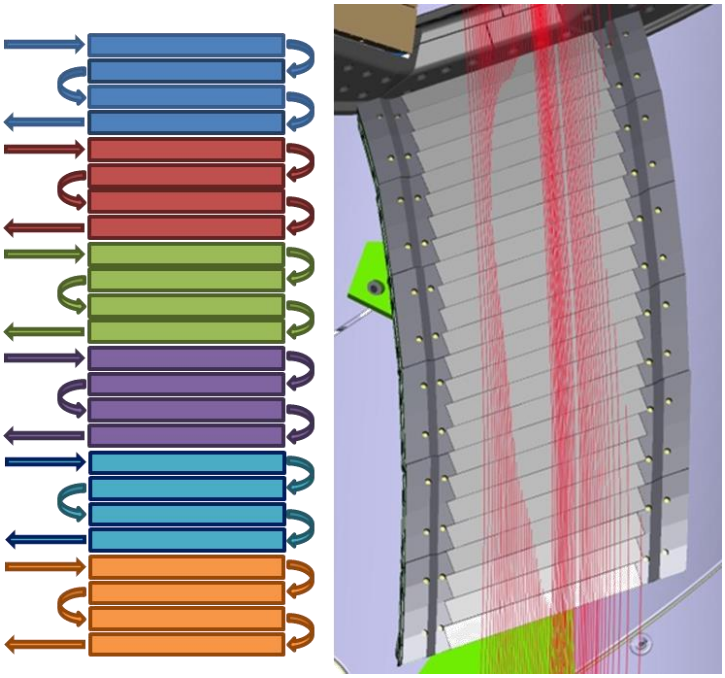

Figure 6.3: Scraper element flow sequence illustration [3]

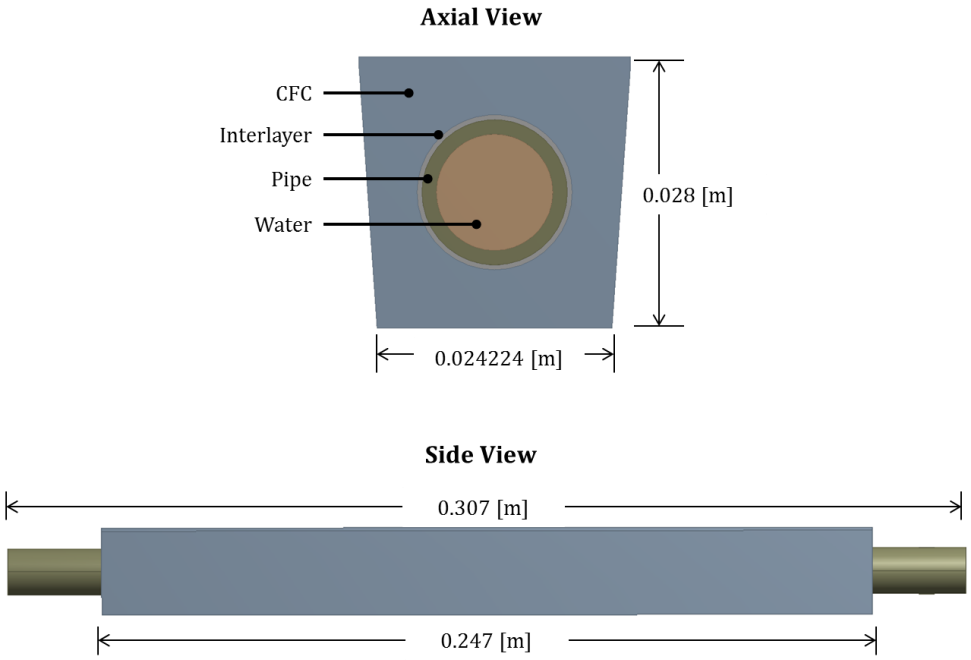


Figure 6.4: CFC monoblock geometry implemented in CFX

The prototype testing for the scraper element PFCs was performed in the Garching Large Divertor Sample (GLADIS) high heat flux test facility at the Max Planck Institute for Plasma Physics located in Garching, Germany [53, 73]. An initial computational investigation into the thermal-hydraulic performance of the prototypes was performed by this author, and the results can be seen in Figures 5 and 6 of Ref. [53]. In the initial investigation, discrepancies were noted between the simulations and the measured data. The discrepancies were investigated further by this author, and the work was summarized in a recently submitted paper denoted by Ref. [74]. The investigation of the discrepancies has been included in the dissertation for completeness and will be discussed in Section 6.6.

The computational models used in the previous studies [53, 74] were repurposed to investigate the local flow information at fusion relevant conditions for this dissertation. Previous monoblock studies [53, 74] were performed by this author with the SST turbulence model because it was presumed to be superior to the other models. However, following the investigation in Chapter 4, the turbulence model was changed to k-epsilon to maintain consistency with Chapters 4 and 5 of this dissertation.

### *6.2.2. Fusion Relevant Conditions*

The conditions for the model setup were chosen to match the experimental parameters investigated in Ref. [53]. The GLADIS test facility is equipped with two sources, which impose a Gaussian loading distribution [73]. The prototypes were placed normal to the beam, and they were cooled with water at a velocity of 12 m/s (including the increased speed due to the twisted tape). The static pressure was 1 MPa, and three peak heat fluxes (PHFs) were investigated: 10.5, 15, and 20 $MW/m^2$ [53].

In the computational setup, a uniform inlet axial velocity was applied for the water at 10.727 m/s. Including the increased velocity due to the twisted tape, this leads to a velocity of 12 m/s. For comparison to the studies in Chapters 4 and 5, the inlet Reynolds number was $1.25x10^5$. The inlet temperature and exit pressure were set to 20°C and 1 MPa, respectively. A Gaussian heat flux profile was applied at the three peak heat fluxes (10.5, 15, and 20 $MW/m^2$). The surface heat flux distribution for the 10.5 $MW/m^2$ case is shown

in Figure 6.5. Note that the peak heat flux is not centered on the CFC monoblock. Instead, the peak is specified to occur at 0.1615 m down the length of the CFC. This specification was made in accordance with the prototype testing [53, 75].

Conjugate heat transfer was modeled from the CFC surface through the solid regions (including the AMC® interlayer and CuCrZr tube) and into the water. Heat transfer was also modeled throughout the solids and the water along with the water-tape interfaces. There was no gap included between the tape and the tube. Instead, the tape-tube interfaces were considered to be adiabatic so that fin effects were not captured in this model. Furthermore, radiation effects were considered to be negligible and were not considered for this work.

Temperature and pressure dependent water properties were implemented with the IAPWS IF-97 formulation [54]. Orthotropic and temperature dependent thermal conductivity values were implemented for the CFC according to equations given in Ref. [76-78]. Figure 6.6 shows the temperature dependent thermal conductivity used for the CFC material. The rest of the solid materials were implemented with constant properties as shown in Table 6.1 [75, 79, 80]. The prototype tests were completed with a copper twisted tape, but the simulations were performed with a stainless steel (SS316) tape. However, this should not have an impact on the solution because the heat transferred to the tape does not make up a significant portion of the heat exchanged in the system.

Simulations for the three PHFs were performed with the k-epsilon turbulence model. A mesh study was performed for the 20 $MW/m^2$ case, and the mesh was refined successively until the maximum temperature in the solids, the average water temperature at the outlet, and the pressure drop changed less than 1% from case to case. The meshing criterion was chosen such that an average volume non-dimensional wall coordinate of $y^+ \approx > 30$ was generated for the highest PHF. The mesh refinement was performed only for the highest PHF because it would result in the most extreme temperatures. Lower temperatures, and thus lower non-dimensional wall coordinates, would be expected for lower PHFs. The same mesh was used for all peak heat fluxes investigated.

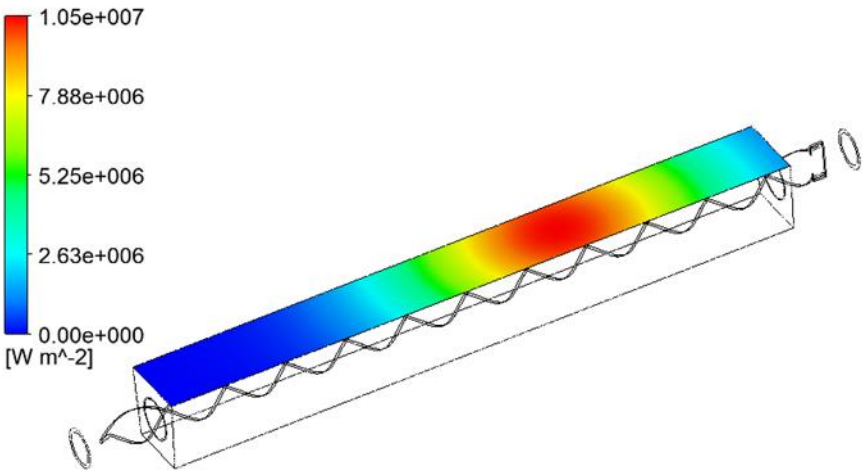


Figure 6.5: Gaussian heat flux profile applied to a monoblock finger [74]

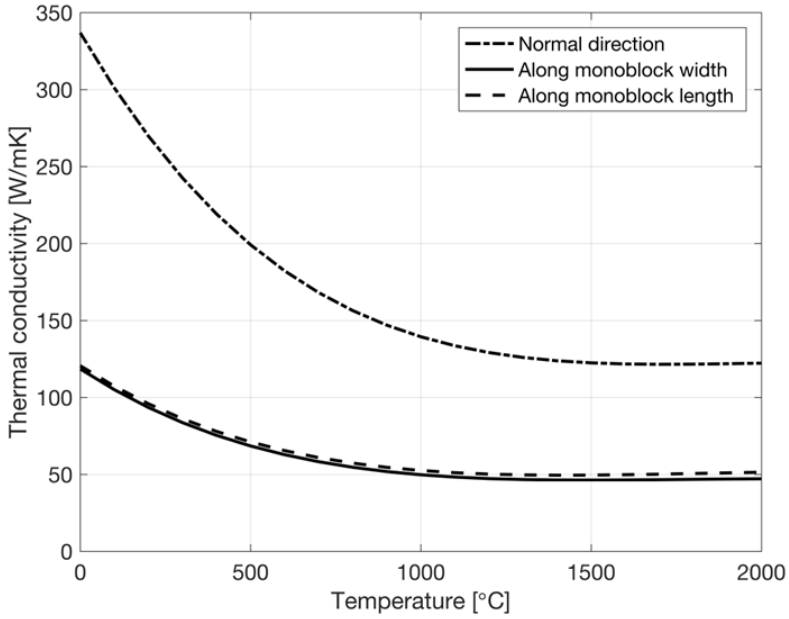


Figure 6.6: Temperature dependent thermal conductivity of CFC NB31 [74]

Table 6.1: Material properties implemented for solid components [75-80]

| Material | Density [kg/m$^3$] | Specific Heat Capacity [J/kgK] | Thermal Conductivity [W/mK] |
|---|---|---|---|
| **AMC® Copper [75, 79]** | 8933 | 385 | 150 |
| **CuCrZr [80]** | 8900 | 390 | 326 |
| **SS316 [80]** | 8031 | 465 | 14 |
| **CFC NB31 [76-78]** | 1959 | 1031 | See Figure 6.6 |

The mesh for this study is shown in Figure 6.7. Inflation layers were implemented on the water-tube and water-tape interfaces. The tube element sizing was chosen to match the water sizing for an acceptable mesh aspect ratio at the water-tube interface. The AMC® interlayer sizing was chosen such that the thickness was resolved by at least two elements, and the CFC sizing was selected to match the element sizing on the tube. The volume-averaged non-dimensional wall coordinate for the water was $y^+ \approx 29$, 32, and 35 for a PHF of 10.5, 15, and 20 MW/m$^2$, respectively.

### *6.2.3. Post-Processing Method*

As shown in Figure 6.8, the experimental data from the prototype testing was taken from infrared images of the CFC surface at the location of PHF. The data was taken at three points: the monoblock center and two edge locations. For comparison to the experiments, three points were created at the same locations along the CFC surface as shown in Figure 6.9. Data was pulled from these locations in the post-processor and will be compared to the experimental results in Section 6.3.

Furthermore, circumferential distributions were investigated at various axial locations. These distributions were created in a similar fashion to those discussed in Chapters 4 and 5. The data was extracted along the water-tube interface at a plane of interest. However, the calculation of the angular coordinate was slightly more complicated due to the monoblock geometry and the origin location. Figure 6.10 shows the angular coordinate on the monoblock geometry along with the origin and center point location. The angle ($\theta$) was calculated based on the x- and z-coordinates by factoring in the offset from origin.

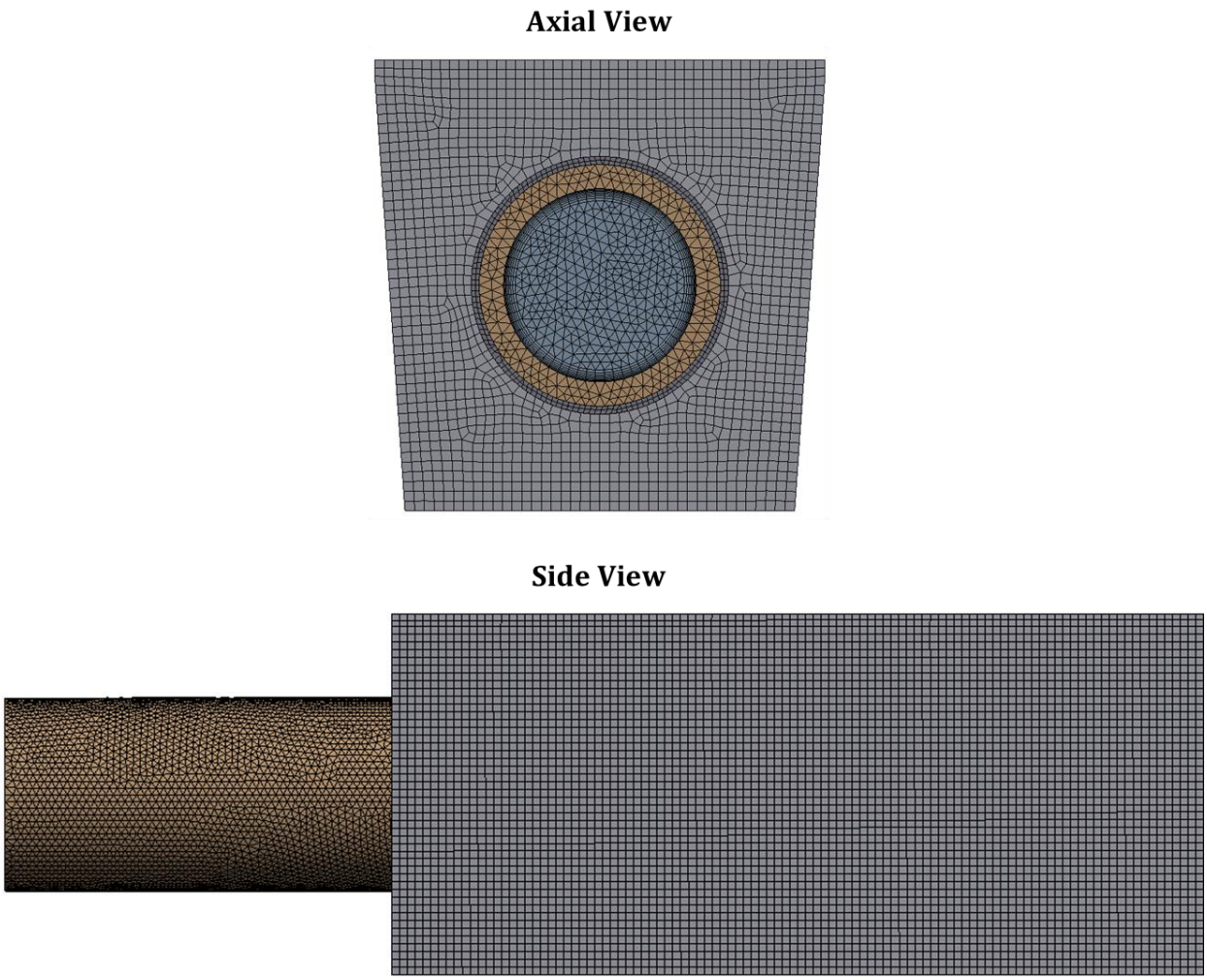


Figure 6.7: Axial and close-up side view of the implemented mesh for the CFC monoblock geometry

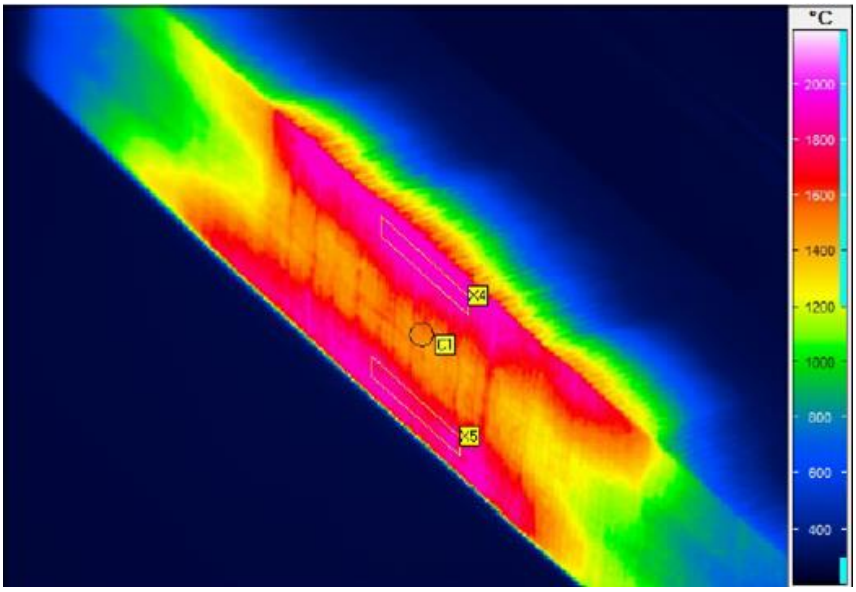


Figure 6.8: Infrared image of the monoblock prototype at PHF of 20 MW/m$^2$ as seen in Ref. [53]

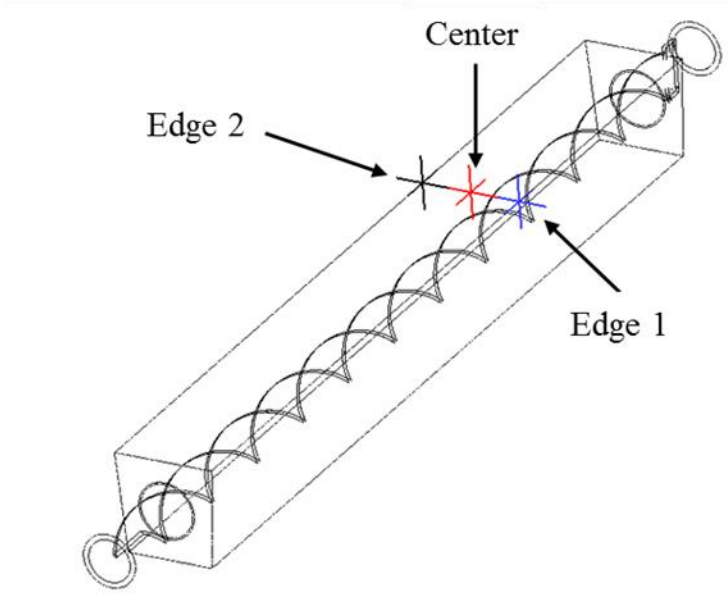


Figure 6.9: Points for post-processing simulations [74]

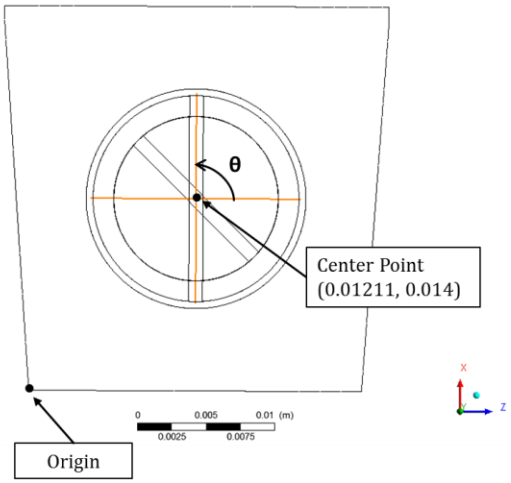


Figure 6.10: Angular coordinate for monoblock geometry circumferential distributions

## 6.3. Comparison to Prototype Testing

### *6.3.1. Initial Comparison*

The computational results were compared to the experimental data collected from the GLADIS high heat flux testing as seen in Ref. [53]. Figures 6.11 and 6.12 show the comparisons at the center and edges of the monoblock, respectively. In the experiments, a discrepancy was revealed between the temperature values at the two edges. Thus, Ref. [53] provides the results for both edge locations. However, there was no notable asymmetry at the edges in the simulations. The computational results shown in Figure 6.12 were taken at the Edge 1 location as shown in Figure 6.9. Such discrepancies between the simulations and the measurements will be further discussed in Section 6.6.

As seen in Figure 6.11, the computational results are lower than the experimental data at PHF of 10.5 and 15 MW/m$^2$. However, at a PHF of 20 MW/m$^2$, the simulations fall within the experimental range. The computational results are closer to the experiments at the edges. Figure 6.12 reveals that the simulations yield results that are near the bottom range of the experimental data for a PHF of 10.5 MW/m$^2$, and they fall within the experimental range at a PHF of 15 MW/m$^2$. Note that the experimental data at a PHF of 20 MW/m$^2$ along the edges was thrown out by the authors; further insight into this decision can be found in Ref. [53].

### *6.3.2. Further Investigation of Results*

Aside from the comparison to the experimental data, the thermal performance was investigated further by viewing the temperature contours for various computational domains. Figure 6.13 shows the temperature contours for the computational domains of interest such as the CFC, AMC® copper interlayer, CuCrZr tube, and the water for a PHF of 10.5 MW/m$^2$. The twisted tape was not included because only a limited amount of heat was transferred between the water and the tape.

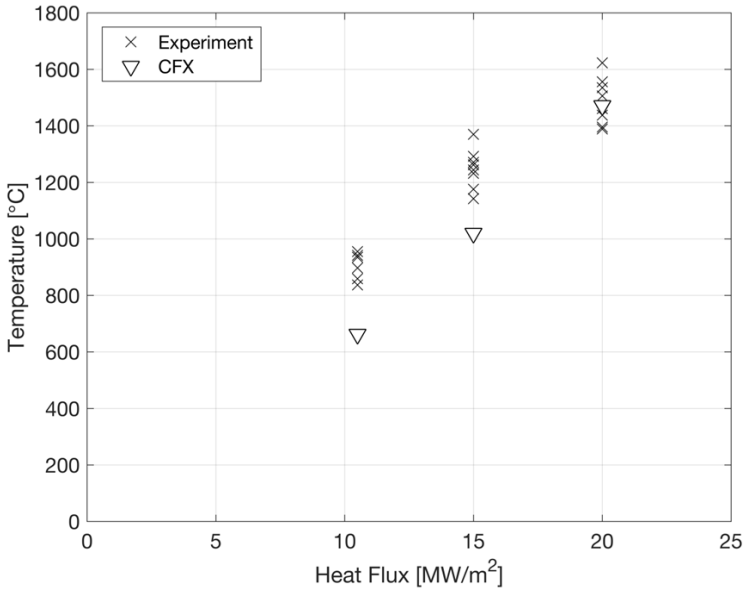


Figure 6.11: Comparison of experimental [53] and CFX results at the center of the monoblock

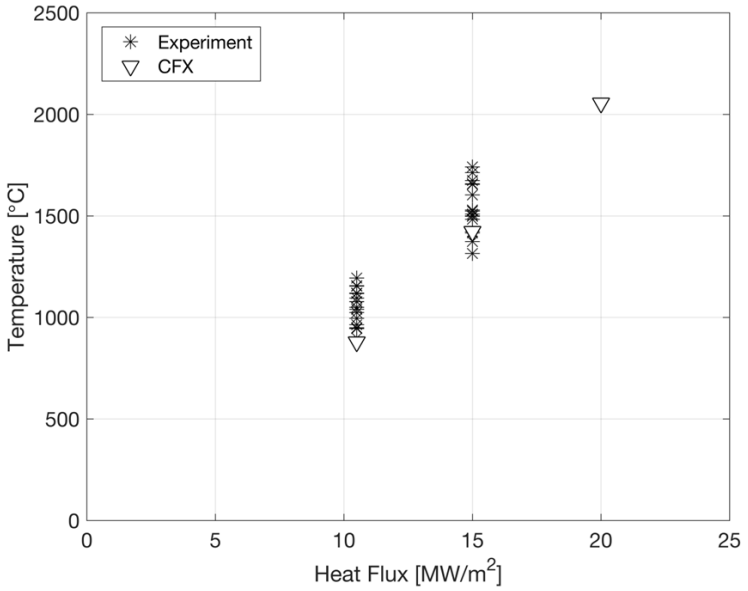


Figure 6.12: Comparison of experimental [53] and CFX results at the edges of the monoblock

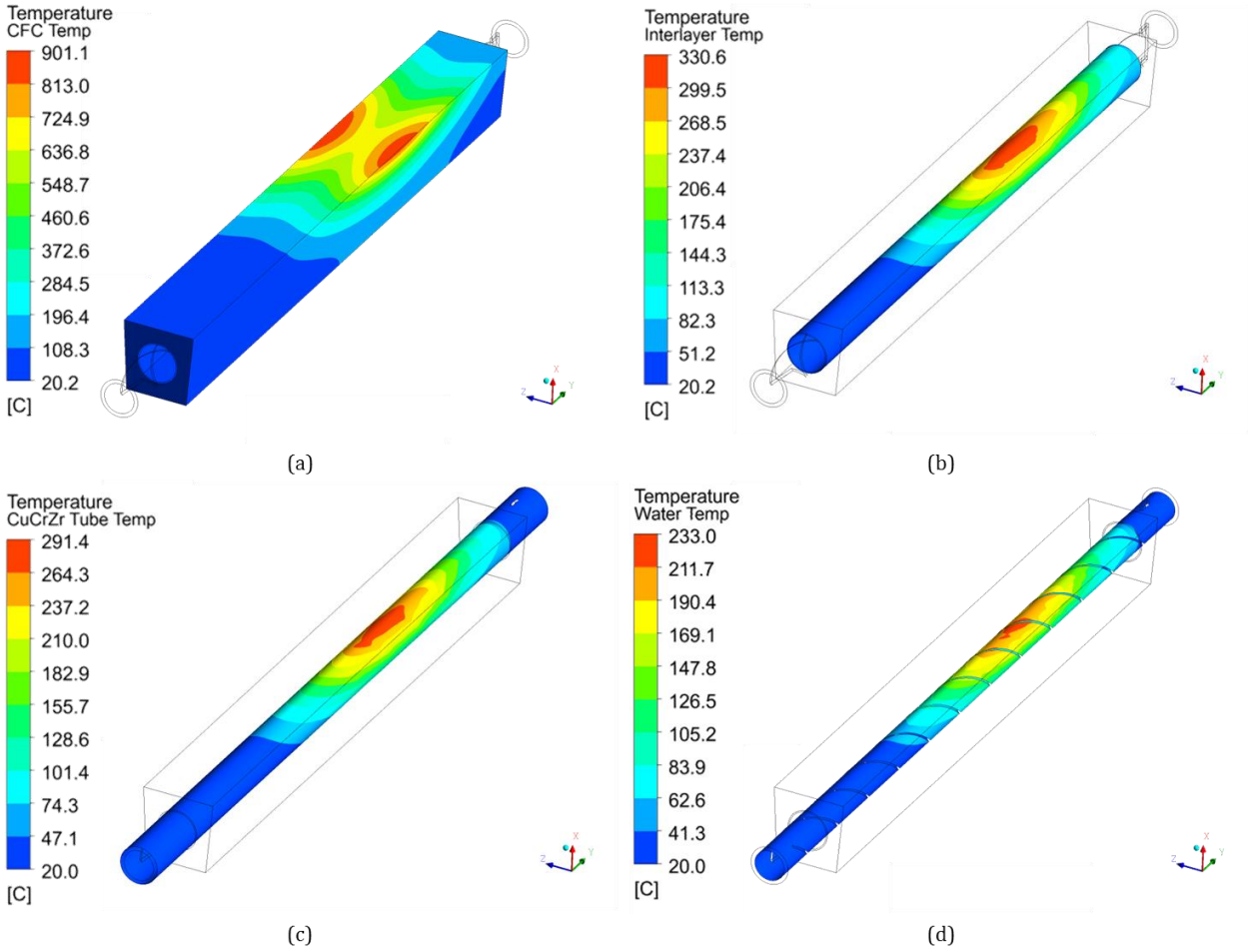


Figure 6.13: Temperature contours of computational domains including the (a) CFC, (b) AMC® copper interlayer, (c) CuCrZr tube, and (d) water for a PHF of 10.5 MW/m$^2$

It should be noted that, even for the lowest PHF case, the temperatures are still extreme. At 1 MPa, the saturation temperature is Tsat≈180°C, and as seen in Figure 6.13, the water temperature is greater than saturation underneath the region of PHF. The peak temperature values for each computational domain of interest are shown in Table 6.2. In each case, the peak water temperature is greater than saturation. This indicates that one would expect to see boiling for these cases. Furthermore, the temperature values in the CFC are extreme. According to Ref. [3], the design limits for the W7-X scraper element require the CFC surface temperature to be below 1200°C. In the cases of 15 and 20 MW/m$^2$ PHF, the peak CFC temperature exceeds this design criterion.

Figure 6.13 also highlights the variation of the temperature distributions due to a one-sided Gaussian heat flux application. The circumferential temperature distribution was created under the location of PHF using the post-processing method discussed in Section 6.2.3. The temperature distribution around the water-tube interface is shown in Figure 6.14. Again, in all cases the water temperature exceeds the saturation temperature. Because of the one-sided heat flux application, the upper surface of the water-tube interface is hotter than the lower side. Furthermore, this distribution indicates that subcooled boiling would be expected to occur on the top surface while convection would occur on the bottom surface.

These results qualitatively agree with those found in the literature. Boscary et al. performed an investigation of the critical heat flux of subcooled water in twisted tape enabled tubes under one-sided heating. As part of their study, the authors performed a finite element investigation of the temperature distribution in the monoblock armor and at the water-tube interface. For the water-tube interface, they concluded that the subcooled boiling regime occurred at the upper portion whereas the convection was dominant in the lower portion of the water [64]. Figure 6.15 shows the comparison between the monoblock armor temperature distributions for the current study and Ref. [64]. The distribution for the current study is shown at the location of PHF for 10.5 MW/m$^2$. As seen in Figure 6.15, the results are qualitatively similar. The isotherms show a similar pattern throughout the monoblock.

Table 6.2: Peak temperature values in domains of interest for all PHF

| Domain | Peak Temperature [°C] | | |
|---|---|---|---|
| | PHF=10.5 [MW/m²] | PHF=15 [MW/m²] | PHF=20 [MW/m²] |
| CFC Armor | 901 | 1457 | 2094 |
| AMC® Copper Interlayer | 331 | 445 | 570 |
| CuCrZr Tube | 291 | 388 | 492 |
| Water | 233 | 301 | 374 |

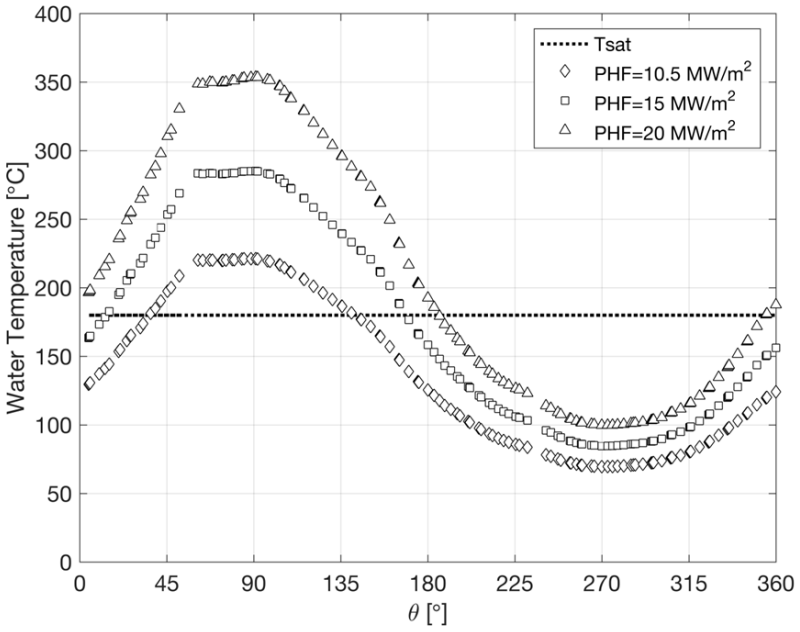


Figure 6.14: Circumferential temperature distributions for various PHF on the monoblock geometry

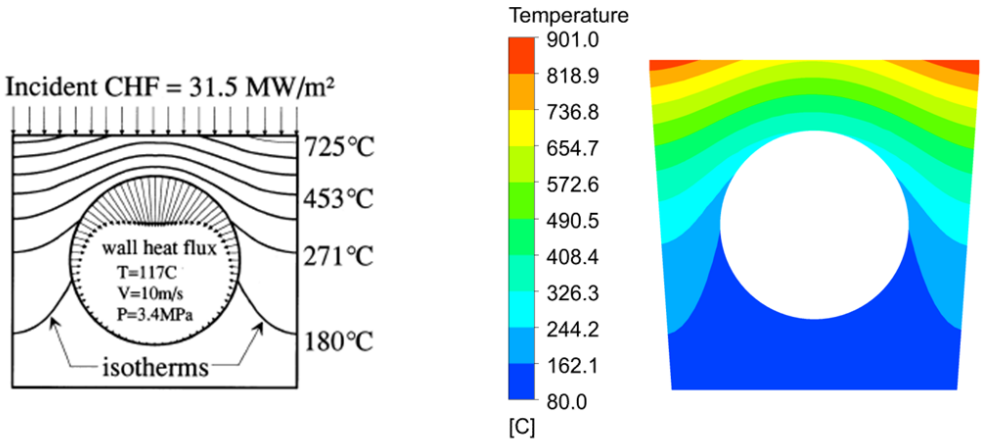


(a) (b)

Figure 6.15: Monoblock temperature distributions for (a) Ref. [64] and (b) the current study at the location of PHF for 10.5 MW/m$^2$

Lastly, the expected boiling regions were investigated in the post-processor. Regions where the water temperature was greater than saturation are shown for each PHF investigated in Figure 6.16. The expected boiling regions cover a notable portion of the water domain, especially for the PHF of 15 and 20 MW/m$^2$. The assumptions and governing parameters of the single-phase model begin to break down as the water temperature approaches and surpasses the saturation temperature. These results highlight the need for the inclusion of the second phase in fusion relevant simulations. Inclusion of the boiling process would result in overall lower temperatures because the phase change would create increased heat transfer at the water-tube interface. This would actually increase the gap between the computational results and the experimental data gathered from the prototype testing in Ref. [53].

It should be noted that higher pressures could be used in fusion relevant experiments, which could mitigate some of the boiling due to increased saturation temperatures. For example, recent ITER experiments have cited pressure values as high as 4 MPa where the saturation temperature is Tsat≈250°C [70]. At that pressure, the water temperature distribution would remain below saturation for a PHF of 10.5 MW/m$^2$. However, as seen in Clark et al. [3], the W7-X divertor scraper element is design to handle pressures up to about 2.5 MPa where the saturation temperature is Tsat≈224°C. In this case, the peak water temperatures seen in this study are still greater than saturation for all PHF investigated.

## 6.4. Analysis of Local Flow Information

In Chapters 4 and 5, local flow information was investigated for a general geometry at moderate, uniform heating conditions. The investigation revealed that the secondary circulation resulted in so-called “inflow regions” where the boundary layer fluid was reinjected into the freestream. These inflow regions were shown to correspond to regions of low wall shear, low heat transfer coefficients, and high surface temperatures. Thus, inflow regions were proposed as likely candidates for early burnout in twisted tape devices.

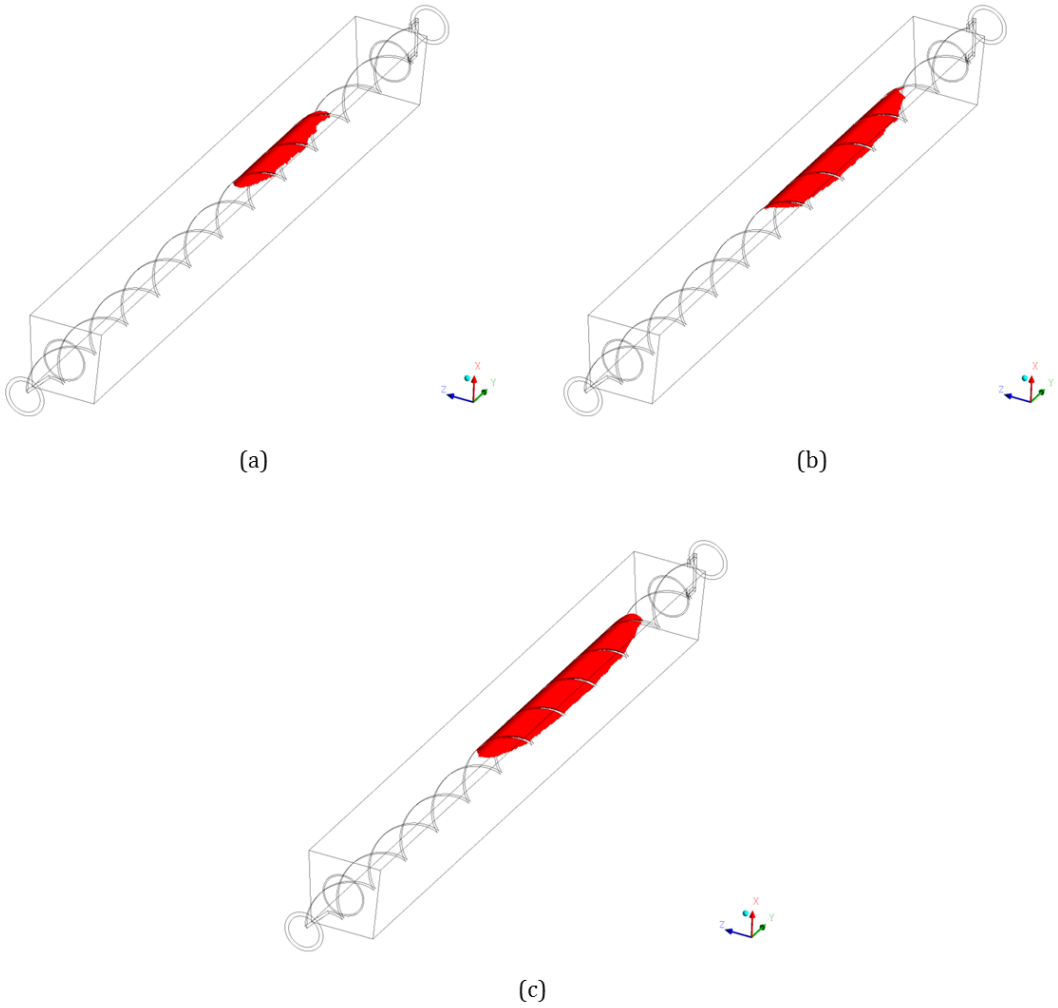


Figure 6.16: Expected boiling regions for PHF of (a) 10.5 MW/m$^2$, (b) 15 MW/m$^2$, and (c) 20 MW/m$^2$

Furthermore, examination of the wall shear stress exposed an apparent "striping" that developed in the twisted tape induced swirl flow. The so-called stripes represent the inflow regions along the water-tube interface; the number and location of the stripes shifts along the test section.

To this author's knowledge, the connection between the inflow regions to possible burnout locations and the wall shear stress striping has not been identified in the twisted tape induced swirl flow literature. In this chapter, a similar investigation into the local flow information will be performed at fusion relevant conditions. The main objectives will be to investigate if the inflow regions and wall shear stress striping still occur at fusion relevant conditions. Furthermore, the connection between the wall shear stress, heat transfer coefficient, and surface temperature will be examined to see if these relationships between these variables still have a significant impact at fusion relevant heating values.

### *6.4.1. Flow Patterns and Temperature Contours*

The flow patterns and temperature contours were investigated for the monoblock geometry at fusion relevant conditions. Figure 6.17 (a) shows the total velocity contour for a PHF of 10.5 MW/m$^2$, while Figure 6.17 (b) shows the tangential velocity vectors at a plane near the exit. The results are qualitatively similar to those seen in Chapter 4 at the moderate heating conditions and in the adiabatic flow visualization experiments [22, 23]. Inflow regions still occur in this case near the exit region, where the secondary flow causes a thickening of the boundary layer (as denoted by arrows).

The flow patterns were investigated at various axial locations for all fusion relevant cases (as provided in Table 6.3). Note that the origin is located at the bottom left corner of the monoblock armor in the model geometry. The locations were chosen such that the tape was in a horizontal orientation near the beginning, middle, and end of the test section. Figure 6.18 shows the total velocity contours at three axial locations for a PHF of 10.5 MW/m$^2$. The hydraulic solution was the same for each PHF investigated.

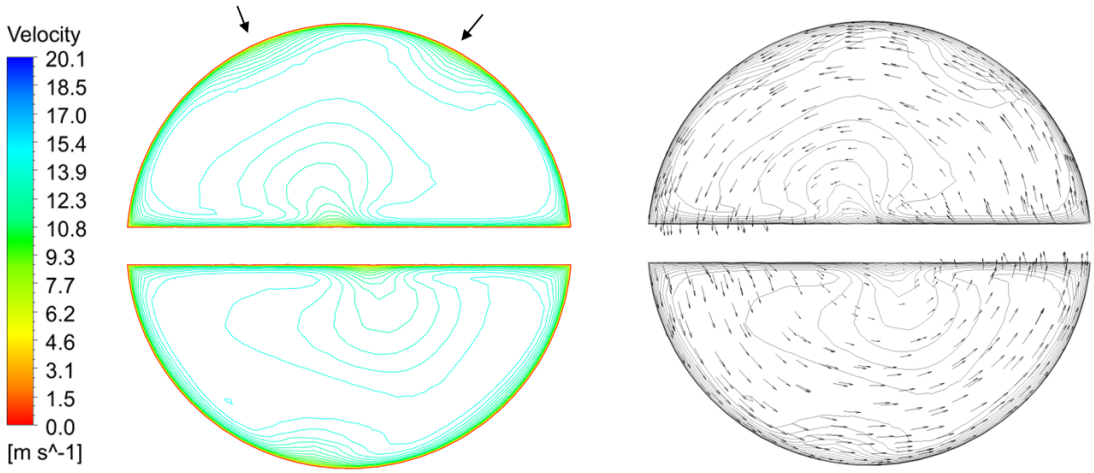


(a) (b)

Figure 6.17: (a) Total velocity contour and (b) tangential velocity projection for PHF=10.5 MW/m$^2$

Table 6.3: Axial locations selected for the fusion relevant local flow investigation

| Plane | Axial Location [m] | Test Section Location |
|---|---|---|
| **1** | 0.01 | Start |
| **2** | 0.13 | Middle |
| **3** | 0.25 | End |
| **CB** | 0.1615 | Center Beam* |

*Center beam location lies directly below the PHF

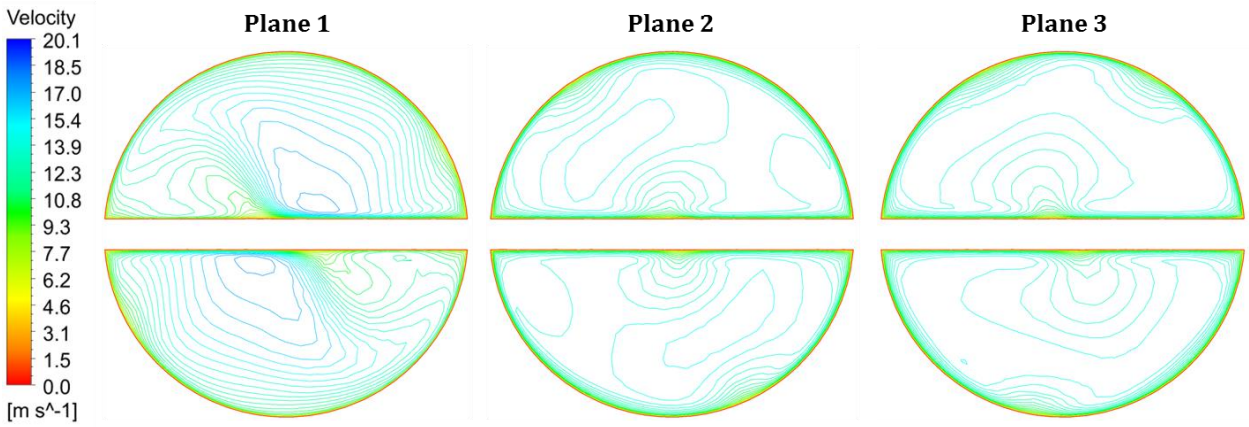


Figure 6.18: Comparison of total velocity contours as the flow moves downstream for the monoblock geometry (PHF=10.5 MW/m$^2$)

Fully developed flow was not noted in the monoblock geometry. This is not surprising due to the short tube geometry included in the model. As seen in Figure 6.18, the secondary flow appears to be developing near the beginning (Plane 1), and inflow regions can be seen near the middle and exit locations.

The local temperature contours were also investigated at two axial locations for the PHF of 10.5 MW/m$^2$. Figure 6.19 shows the comparison between the total velocity contours and the temperature contours for two axial locations: under the PHF location and near the exit. In both locations, the inflow regions appear to have a qualitative connection to the local temperature contour (as indicated by the arrows). However, under the location of PHF (at Plane CB), there is an extreme temperature gradient in the flow field. This large gradient makes it difficult to glean information from the contour. The water-tube interface values will provide a better insight into the possible connection between inflow regions and the surface temperature. Figure 6.19 also reveals the large temperature difference between the two axial locations. The maximum temperature at the location of PHF is over five times higher than the peak temperature near the exit region.

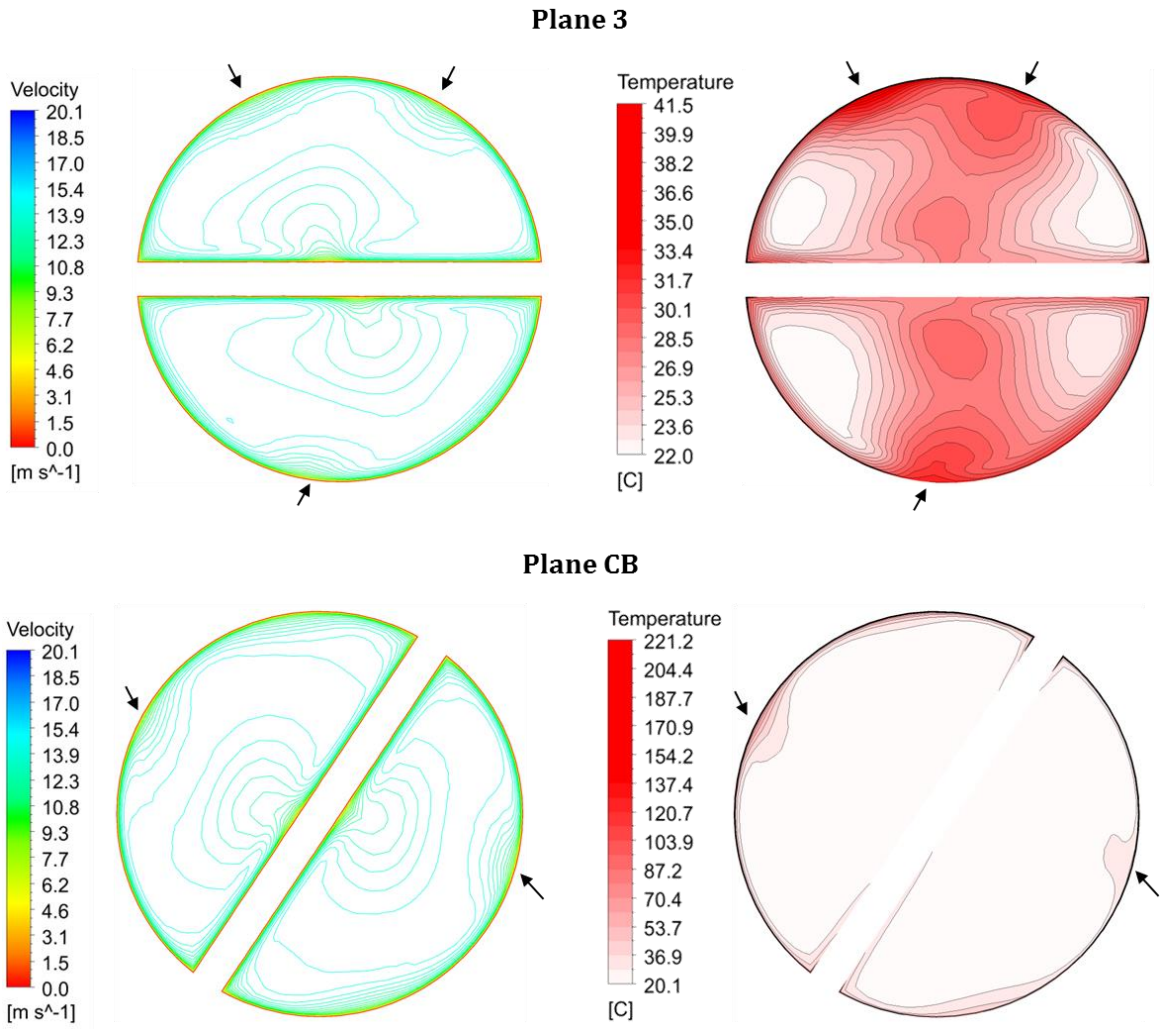


Figure 6.19: Comparison of total velocity and temperature contours under the location of PHF (Plane CB) and near the exit (Plane 3) for the monoblock geometry (PHF=10.5 MW/m$^2$)

### *6.4.2. Further Investigation of Inflow Regions*

As discussed in Chapter 4, the secondary flow causes thickening of the boundary layer at the inflow regions, and this local boundary layer thickening was shown to result in a lower wall shear stress, which corresponded to a lower heat transfer coefficient and thus, a higher surface temperature in those regions. Furthermore, the inflow regions were shown to correspond to an apparent "striping" of low wall shear stress when viewing the full contours. These relationships will be investigated further in this section to determine if they are still prevalent at fusion relevant conditions.

The wall shear stress can be visualized by viewing the contours along the water-tube interfaces. Figure 6.20 shows the wall shear stress contours for all of the PHF investigated for the monoblock geometry. As seen in Figure 6.20, the shear stress contours reveal a striping pattern, which suggests that this phenomenon is still prevalent at fusion relevant conditions.

The wall shear stress, wall heat flux, and surface temperature were exported along the perimeter for two axial locations: under the PHF and near the exit. The heat transfer coefficient (HTC) was calculated at each surface point using Eq. 4.6 along with the mean temperature as shown by Eq. 4.7. Due to the different tape orientations, the results were compared along the water-tube interface. All the data was extracted for a PHF of 10.5 $MW/m^2$ and was plotted against the angular coordinate as shown in Figure 6.10.

The wall shear stress and wall heat flux at the location of PHF are shown together in Figure 6.21. Similarly, the wall shear stress and HTC are shown together in Figure 6.22, and the wall shear stress and surface temperature (Ts) are shown in Figure 6.23. Figure 6.21 reveals the connection between the wall shear stress and the wall heat flux, which is similar to the uniform heating results seen in Chapter 4. There does appear to be a connection between the wall shear stress and the wall heat flux. However, it does not appear to be as strong as the connection viewed in Chapter 4. Locations of low wall shear correspond to slight decreases or flattening of the curve.

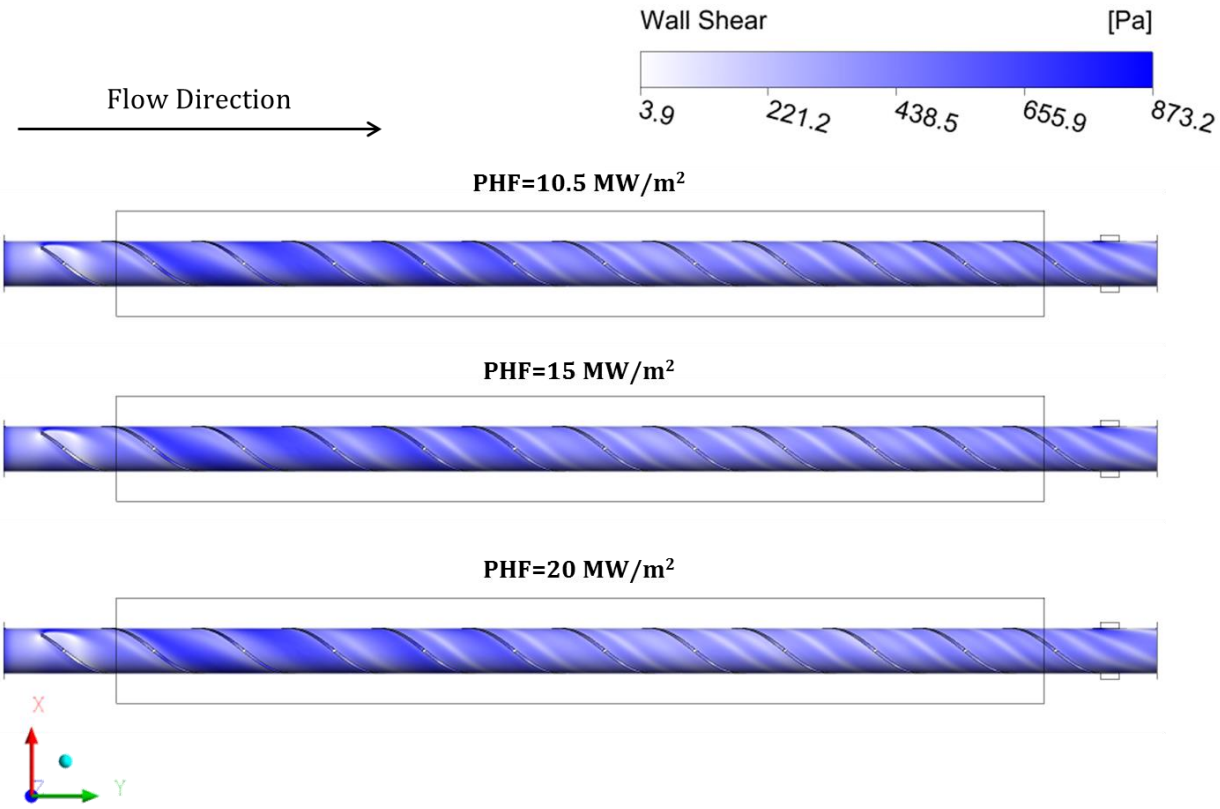


Figure 6.20: Wall shear stress contours for the monoblock geometry

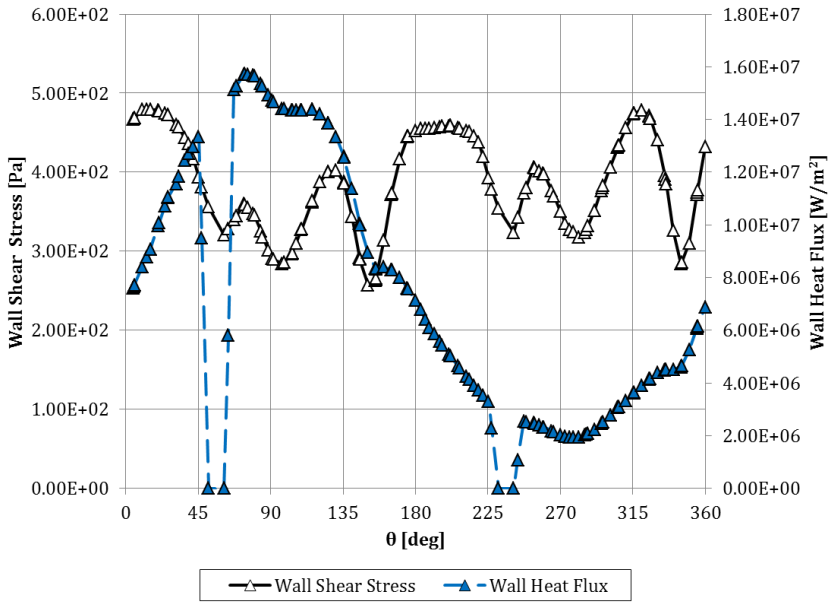


Figure 6.21: Comparison of wall shear stress and wall heat flux along the water-tube interface at the location of PHF (Plane CB in Table 6.3, PHF=10.5 MW/m$^2$)

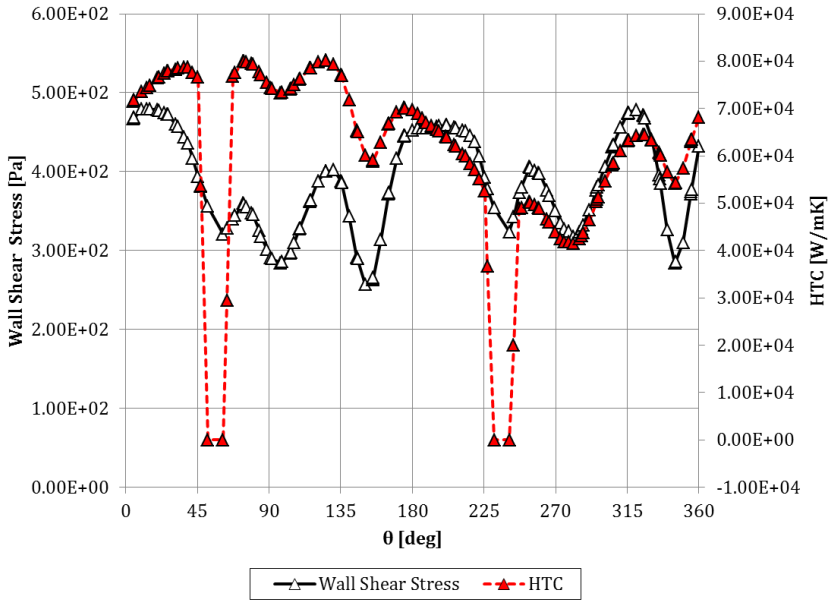


Figure 6.22: Comparison of wall shear stress and HTC along the water-tube interface at the location of PHF (Plane CB in Table 6.3, PHF=10.5 MW/m$^2$)

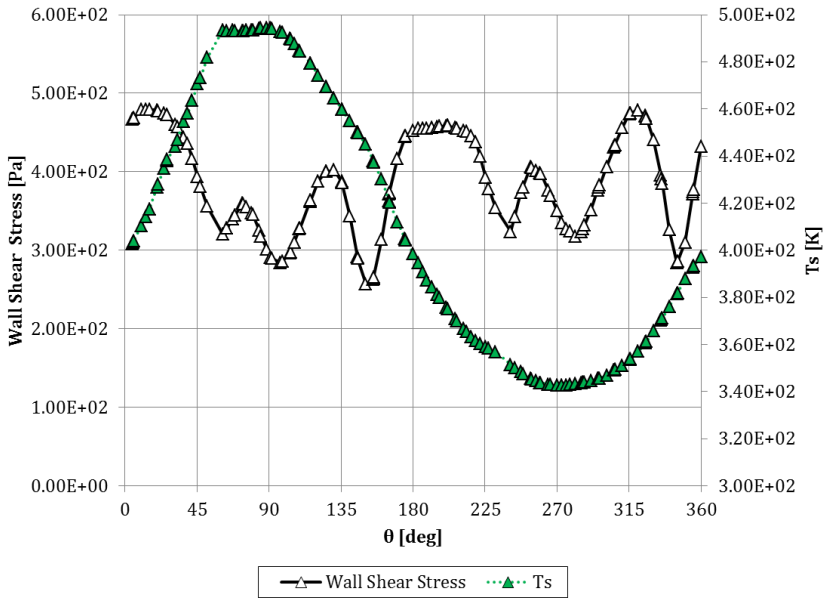


Figure 6.23: Comparison of wall shear stress and surface temperature along the water-tube interface at the location of PHF (Plane CB in Table 6.3, PHF=10.5 MW/m$^2$)

The connection between the wall shear stress and the HTC is shown in Figure 6.22. The relationship is more pronounced here where dips in the wall shear stress result in clear dips in the HTC. Conversely, the connection between the wall shear stress and the surface temperature is not apparent in this case as can be seen in Figure 6.23. The dips in the wall shear stress no longer noticeably correspond to peaks in the surface temperature. As discussed in Section 6.3.2, the general trend of the surface temperature is as expected in the literature [64]. However, locally, it does not appear to be affected by the wall shear stress. This is further illustrated by a zoomed in view of the peak surface temperature as shown in Figure 6.24.

Figure 6.25 shows the comparison between the wall shear stress and the surface temperature at a plane near the exit region. A similar behavior was observed, where the temperature gradient is much lower than the location of PHF. Even with the moderate gradient seen in Figure 6.25, the wall shear stress did not appear to have a great impact on the surface temperature.

## 6.5. Discussion of Local Relationships at Fusion Relevant Conditions

The lack of a prevalent connection between the surface temperature and wall shear stress results at fusion relevant conditions necessitated further investigation into the relationship. A few items were explored including the global effect on full contours, IAPWS water properties, near wall behavior, and the connection at lower peak heat fluxes.

### *6.5.1. Full Contour Comparison*

The full monoblock contours were viewed to investigate the relationship between the wall shear stress, wall heat flux, and temperature. Figure 6.26 shows the comparison between the three variables for the whole water domain from a top down viewpoint. From this perspective, the wall shear striping appears to have a noticeable effect on the wall heat flux (as indicated by the arrows). However, there looks to be a very small effect on the temperature.

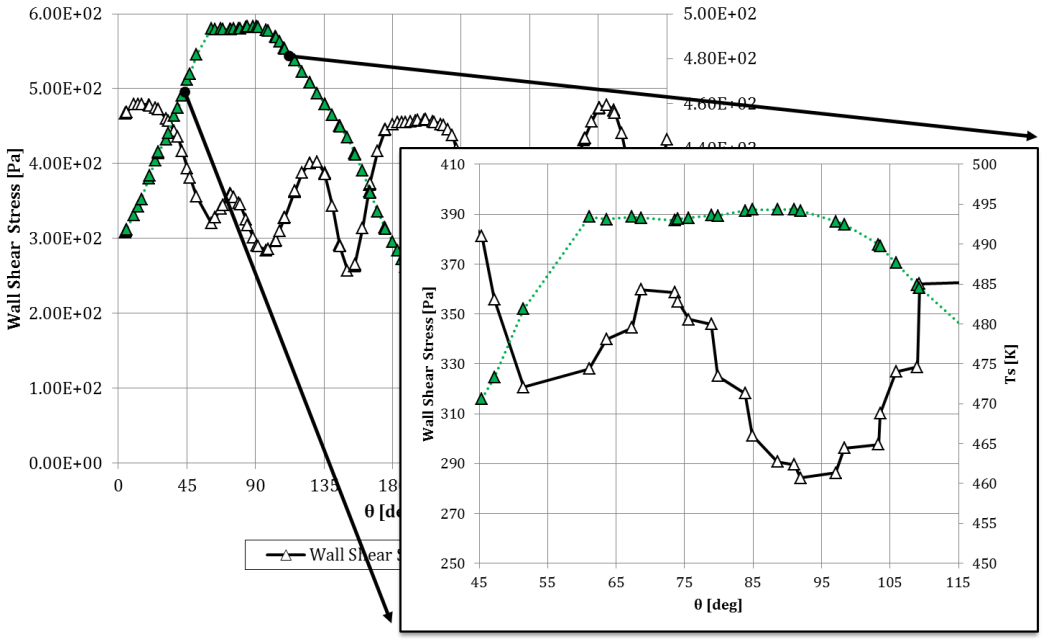


Figure 6.24: Close-up view of the peak surface temperature along the water-tube interface at the location of PHF (Plane CB in Table 6.3, PHF=10.5 MW/m$^2$)

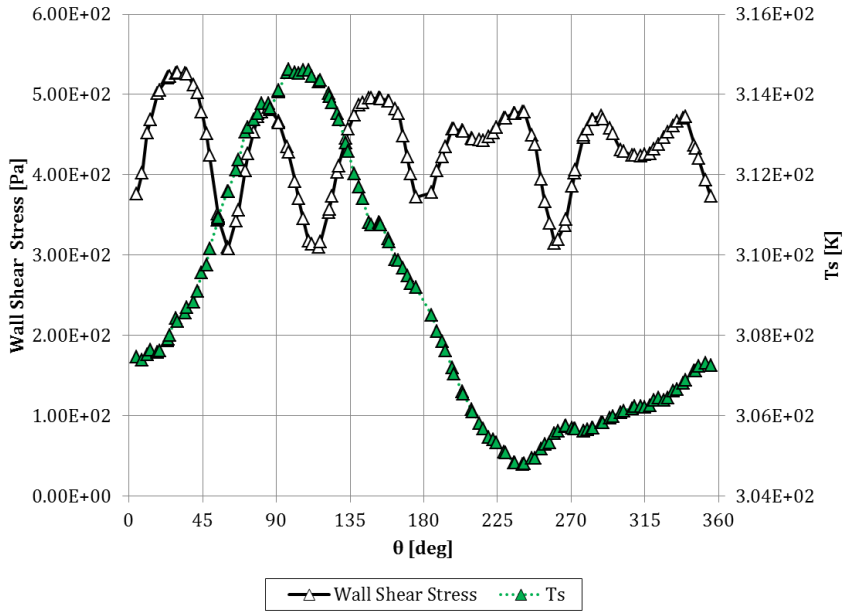


Figure 6.25: Comparison of wall shear stress and surface temperature along the water-tube interface near the exit region (Plane 3 in Table 6.3, PHF=10.5 MW/m$^2$)

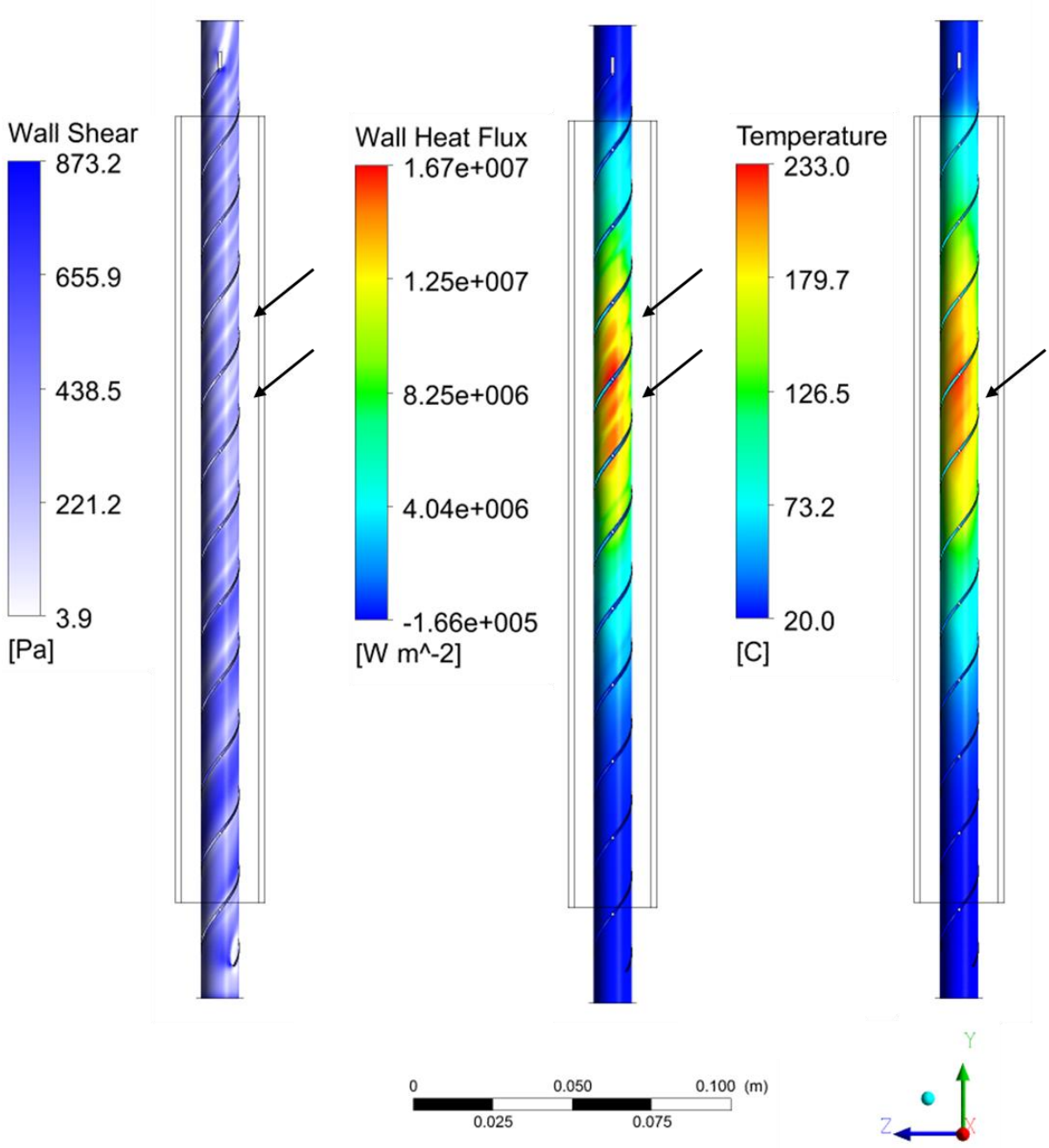


Figure 6.26: Comparison of wall shear stress, wall heat flux, and surface temperature for the full water domain from the monoblock geometry (Top down viewpoint)

### *6.5.2. Investigation of IAPWS Water Properties*

As discussed in Section 6.3, the peak temperatures from the computational solutions were greater than the saturation temperature. However, the computational model is constricted to single-phase, which could potentially lead to unrealistic property values from the IAPWS library. The phase diagram for the IAPWS equations implemented in ANSYS CFX is shown in Figure 6.27 where the numbered regimes represent the following phases [42, 54]:

1. Subcooled water
2. Supercritical water/steam
3. Superheated steam
4. Saturation data
5. High temperature steam

Regimes 1-4 are included in CFX, and this author's calculations were performed with IAPWS equations from Regime 1 only. The peak water temperatures are shown again in Table 6.4. Comparison between the phase change diagram and the peak water temperatures reveals that PHF of 10.5 and 15 MW/m$^2$ fall within the temperature and pressure ranges of Regime 1. However, the temperature exceeds the subcooled water regime for a PHF of 20 MW/m$^2$ by roughly 25°C. With a pressure of ≈1 MPa, this places the PHF of 20 MW/m$^2$ in Regime 4.

The behavior of the water properties was investigated for the subcooled water regime. Figure 6.28 shows the density (ρ), specific heat capacity ($c_p$), dynamic viscosity (μ), and thermal conductivity (k) over a range of temperatures at 1 MPa. These figures reveal sharp changes in the water properties at approximately 320°C. Thus, the fusion relevant investigation is stretching the limits of the single-phase model and the IAPWS properties implemented in it.

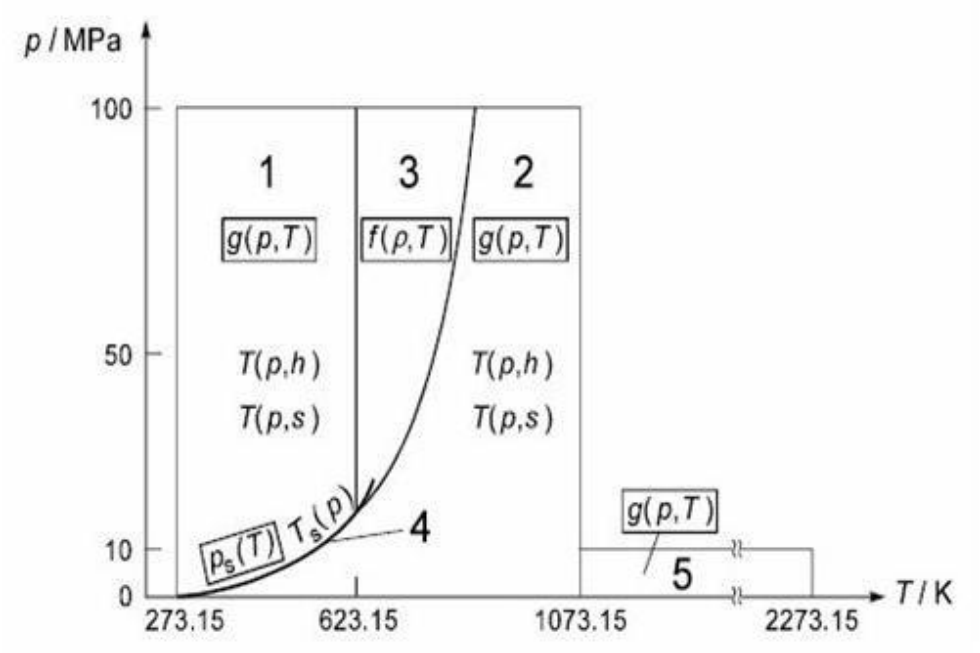


Figure 6.27: Water property regimes for the IAPWS IF-97 formulation as implemented in ANSYS CFX [42, 54]

Table 6.4: Peak water temperature for the monoblock model

| PHF | Peak Water Temperature [K] |
|---|---|
| **10.5** | 506 |
| **15** | 575 |
| **20** | 647 |

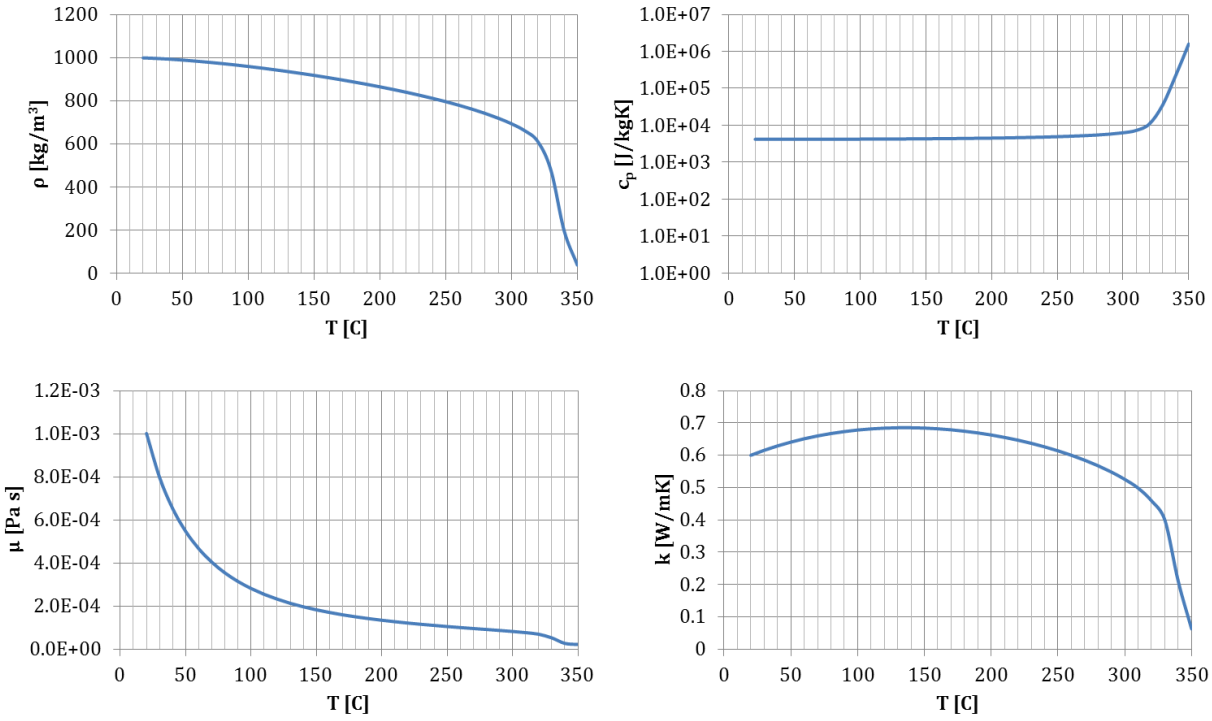


Figure 6.28: IAPWS water properties in the subcooled water regime

### *6.5.3. Investigation of Near Wall Behavior*

The near wall behavior was investigated for a PHF of 10 MW/m$^2$ at three axial locations including Plane 2, Plane 3 and Plane CB as seen in Table 6.3. The velocity and temperature profiles were investigated near the wall at the top of the tube—where the heat flux is applied. For this analysis, a line was created near the wall from two points as shown in red in Figure 6.29, and fifteen points were sampled along the line (Note: there are only nine mesh points along this line). The total velocity and temperature profiles were plotted against the distance from the wall as shown in Figures 6.30 and 6.31. Figure 6.31 reveals extreme temperature gradients at locations where significant heat is applied (Plane 2 and Plane CB). However, large temperature gradients are to be expected for twisted tape devices. As discussed by Manglik and Bergles, passive heat transfer enhancement techniques tend to generate "well-mixed" flows with considerably sharper wall temperature gradients than normal [8]. Such large temperature gradients could be used as justification for the use of a low Reynolds number approach for the turbulence modeling where the model has the capability to resolve the flow near the wall (such as SST or Reynolds stress models).

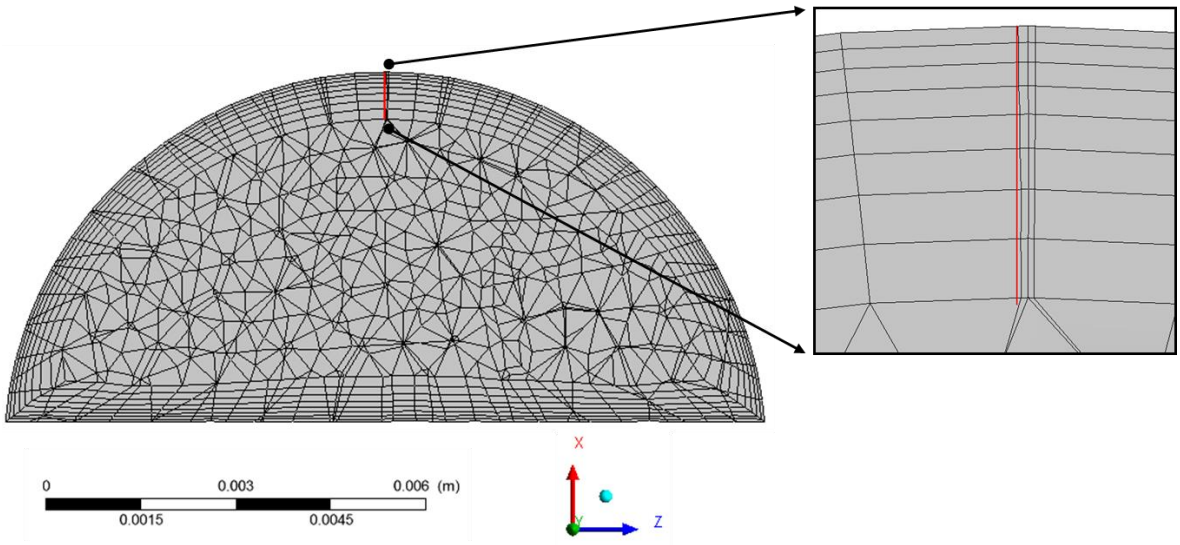


Figure 6.29: Sampling line utilized in near wall investigation

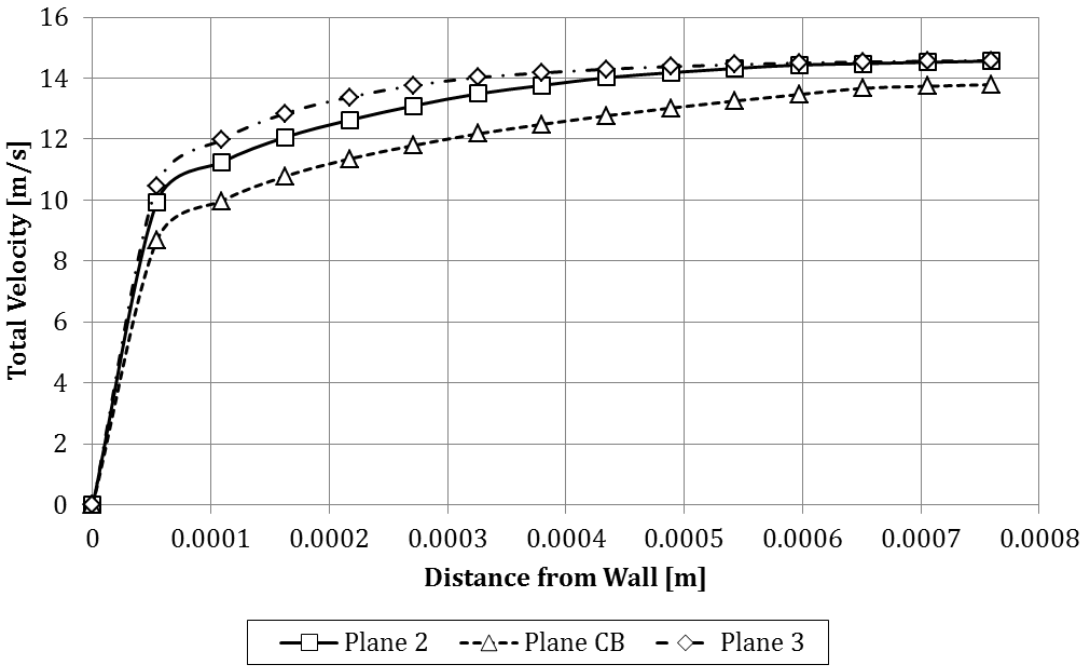


Figure 6.30: Total velocity profiles in the near wall region at three axial locations as given in Table 6.3

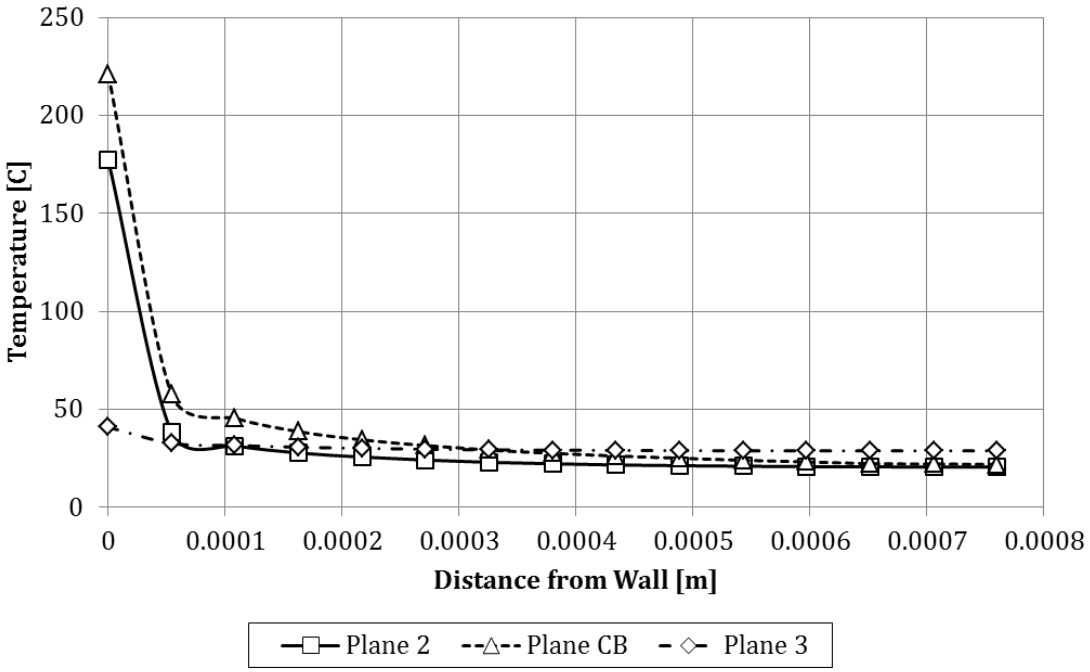


Figure 6.31: Temperature profiles in the near wall region at three axial locations as given in Table 6.3

The non-dimensional velocity and temperature profiles were also determined as part of the near wall investigation. The profiles were created following the guidance of Ref. [39] as discussed in Chapter 3. The water properties and the axial velocity were exported along the line shown in Figure 6.29. Points were created at the top of the line at the water-tube interface for the variables at the wall. The dimensionless velocity ($u^+$) was calculated from Eq. 3.8 and 3.10, while the dimensionless temperature ($T^+$) was determined from Eq. 3.15 and 3.16. The non-dimensional velocity and temperature were plotted against the dimensionless wall coordinate ($y^+$) as given by Eq. 3.9.

The dimensionless velocity and temperature profiles are shown in Figures 6.32 and 6.33, respectively. These profiles reveal that the first node away from the wall has a non-dimensional wall distance in the range of $y^+ \approx 50\text{-}60$. The location of peak heat flux (Plane CB) has a higher $y^+$ due to the increased temperature in that region.

The near wall behavior was discussed in detail in Chapter 3. Review of this discussion suggests that a dimensionless wall distance of $y^+ \approx 50$ places the first mesh point outside of the buffer region in the log law or overlap layer. This falls in line with the assumptions of the wall function approach, which was utilized due to the implementation of the k-eps model for these simulations. The use of wall functions prevents a full resolution of the near wall behavior, and thus, the viscous sublayer and buffer layer are not represented in Figures 6.32 and 6.33. For a full resolution of the boundary layer, a low Re approach with an appropriately refined mesh should be implemented. While the viscous sublayer and buffer layer are not shown here, the data reveals similar behavior to the velocity profiles shown in Ref. [39, 44]. The overlap layer is represented by the linear portion of the curve, and the defect layer is represented by curved portion. For example, consider Plane 3 in Figure 6.32. The overlap or log law region is represented by the linear trend from $y^+ \approx 50\text{-}110$. The defect layer follows at $y^+ > 110$. While not as distinct, this transition can be seen at the other planes as well. The transition is not as clear in the dimensionless temperature profile for Planes 2 and CB because of the higher temperature gradients at those planes.

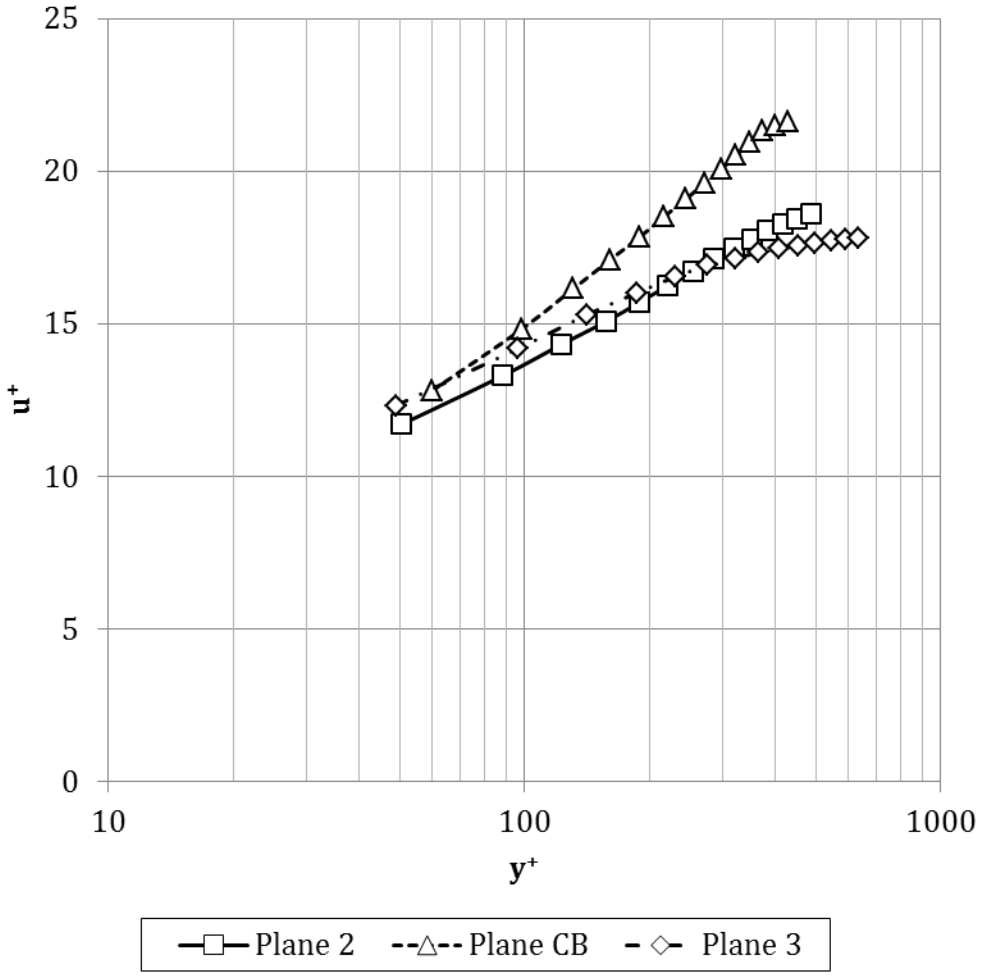


Figure 6.32: Non-dimensional velocity profile in the near wall region

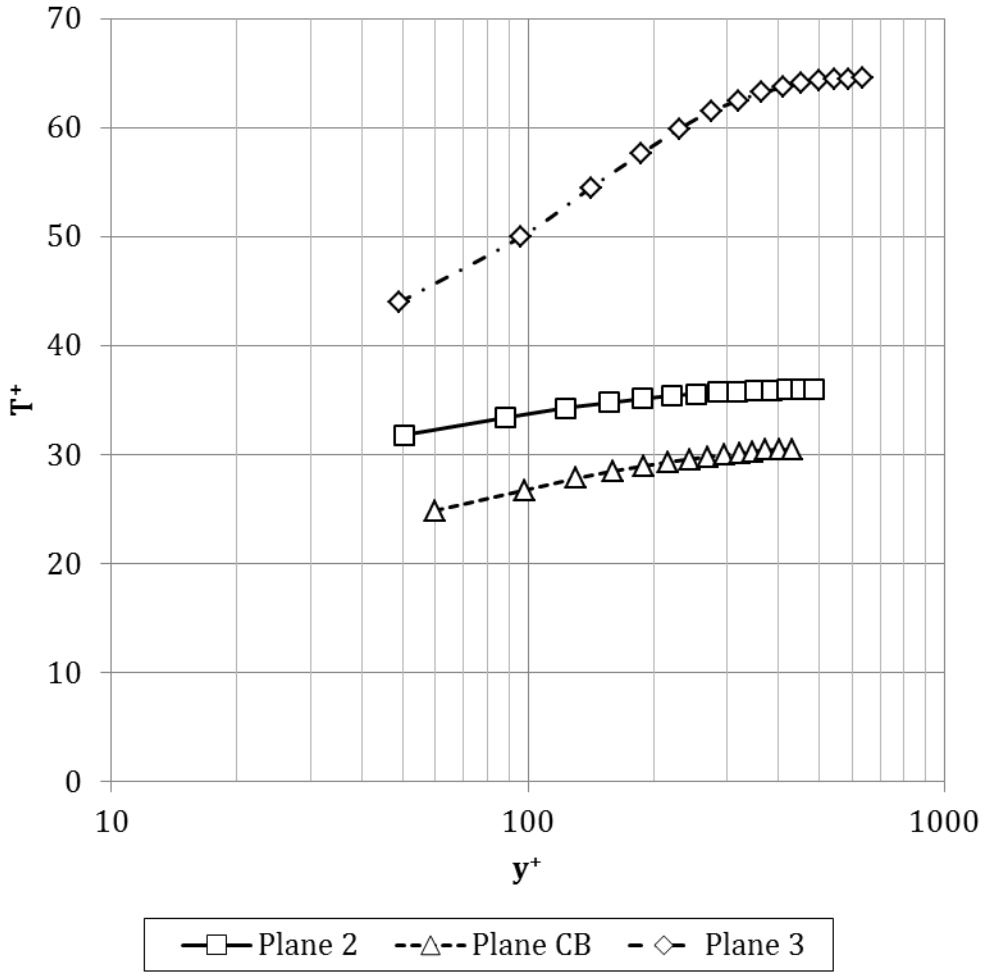


Figure 6.33: Non-dimensional temperature profile in the near wall region

As discussed in Chapter 3, the inner layer connects with the log law region at a dimensionless wall coordinate of $y^+ \approx 30$. This inspired the selection of the mesh criteria for this study, which included an average volume $y^+$ of approximately 30 (as seen in Section 6.2.2). Figures 6.32 and 6.33 reveal the local variation in the $y^+$ at different locations. This difference is especially clear at regions of higher temperatures where there are higher $y^+$ values. In retrospect, this local variation could have been taken into account for the meshing strategy. One could envision a more refined mesh overall where the criteria was a dimensionless wall distance of $y^+ \approx 30$ at the location of peak heat flux.

### *6.5.4. Analysis of Local Flow Information at Lower Peak Heat Fluxes*

Solutions were completed with lower peak heat fluxes to determine if the connection between the wall shear stress and the surface temperature was more prevalent at less extreme conditions. The model setup and conditions discussed in Section 6.2 were utilized in these solutions. The only change was the applied peak heat fluxes, which were reduced to 1 and 5 MW/m$^2$.

The water temperature contours for these solutions are shown in Figure 6.34. Neither solution reaches the saturation temperature of $T_{sat} \approx 180°C$. The wall shear stress, wall heat flux, and surface temperature were exported along the perimeter at the location of PHF. The HTC was calculated using Eq. 4.6 along with the mean temperature as given by Eq. 4.7. The data was extracted for the lowest PHF of 1 MW/m$^2$ and was plotted against the angular coordinate as shown in Figure 6.10.

The wall shear stress and wall heat flux are shown together in Figure 6.35. Similarly, the wall shear stress is compared to the HTC and the Ts in Figures 6.36 and 6.37, respectively. Figure 6.35 reveals similar results to those seen in Section 6.3. There is an apparent connection between the wall shear stress and the wall heat flux. Locations of low wall shear stress correspond to slight decreases or flattening of the curve. Again, the relationship between the wall shear stress and the HTC is more pronounced as seen in Figure 6.36. However, as can be seen in Figure 6.37, the connection between the shear stress and the surface temperature is still not apparent—even at much lower applied heat fluxes.

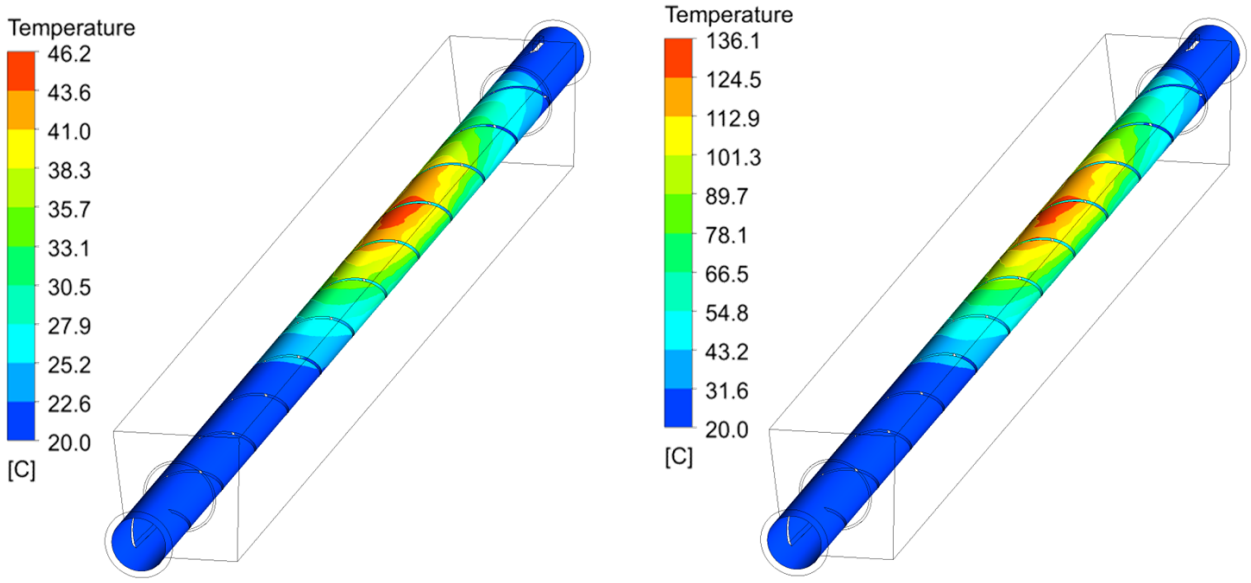


(a) (b)

Figure 6.34: Water temperature contours for lower applied PHF of (a) 1 MW/m$^2$ and (b) 5 MW/m$^2$

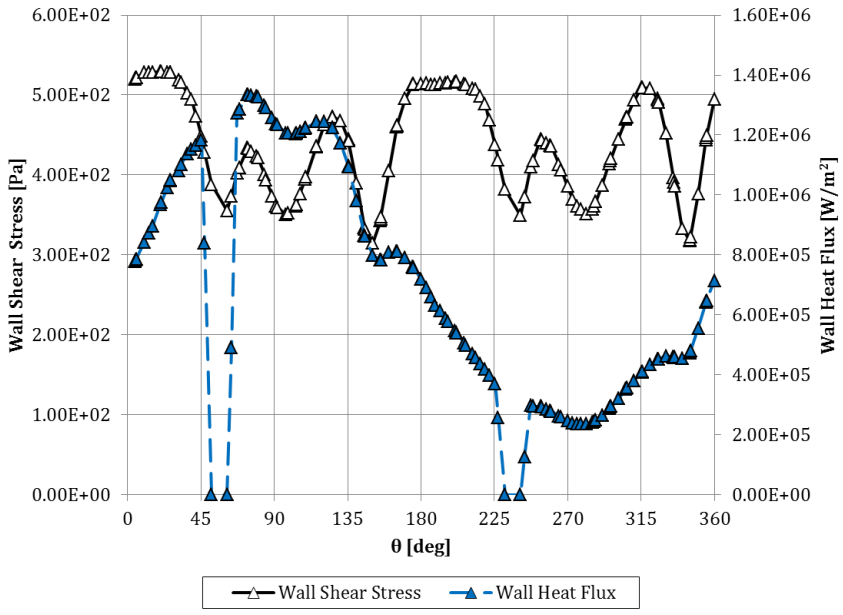


Figure 6.35: Comparison of wall shear stress and wall heat flux along the water-tube interface at the location of PHF (Plane CB in Table 6.3, PHF=1 MW/m$^2$)

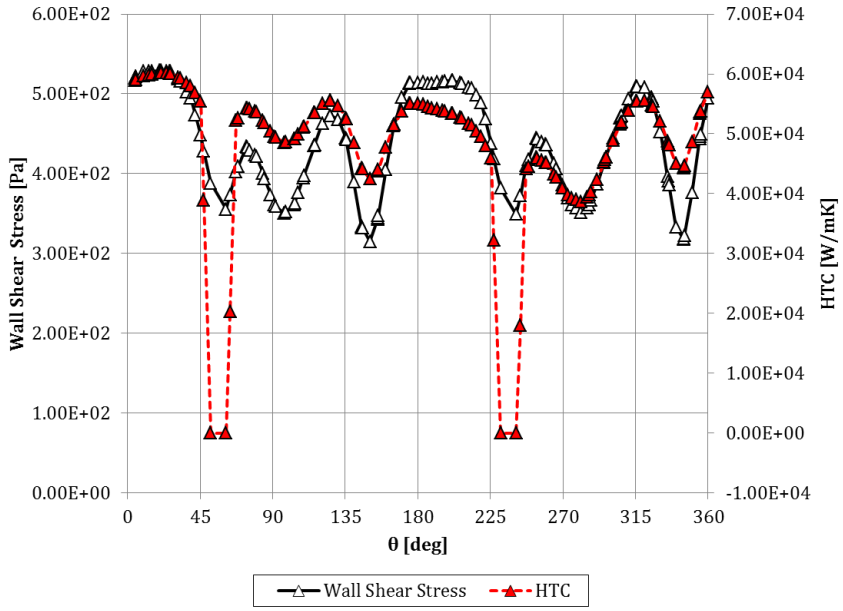


Figure 6.36: Comparison of wall shear stress and HTC along the water-tube interface at the location of PHF (Plane CB in Table 6.3, PHF=1 MW/m$^2$)

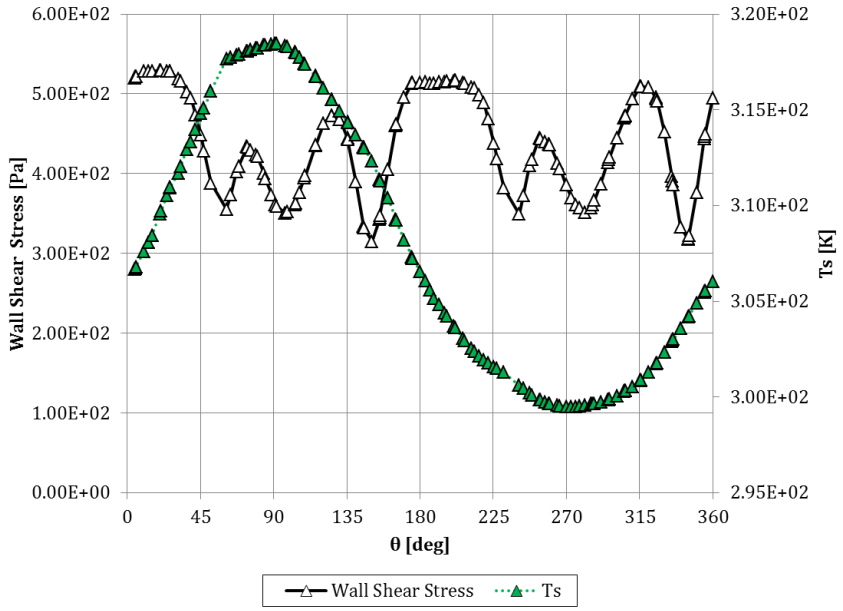


Figure 6.37: Comparison of wall shear stress and surface temperature along the water-tube interface at the location of PHF (Plane CB in Table 6.3, PHF=1 MW/m$^2$)

This suggests that the effect of the wall shear stress striping on the surface temperature is minimal for one-sided non-uniform heating conditions. The change in temperature due to the depressed wall shear stress is minimal compared to the change in temperature due to the applied heat flux. Consideration of the results seen in Chapters 4 and 5 would suggest that this phenomenon is more important for uniform, moderate heating applications.

## 6.6. Investigation of Discrepancies from CFC Prototype Testing

As discussed in Section 6.3.1, comparison of computational and experimental results from the prototype testing revealed discrepancies between the simulations and measurements. The discrepancies were investigated further by this author, and the work was summarized in a recently submitted paper denoted by Ref. [74]. The investigation of the discrepancies has been included in the dissertation for completeness and will be discussed in this section.

Potential explanations for the differences between the simulations and measurements could lie in the manufacturing process of the monoblock prototypes. One uncertainty is in the circumferential casting process, which could result in a better thermal connection at the top and bottom as opposed to the sides of the tube. Another source of the discrepancy could be a slight misalignment of CFC fibers in the off-normal direction. The orthotropic CFC thermal properties depend on the orientation of the fibers, where the direction of peak thermal conductivity is generally aligned parallel with the direction of the applied heat flux (often the normal direction) [74, 76-78]. Slight misalignment of the fibers during manufacturing would result in an offset in the thermal properties, and the direction of peak thermal conductivity would align to a direction slightly off-normal [74]. While not investigated here, it should be noted that a few other explanations have been raised to resolve the discrepancies such as potential degradation of the CFC properties due to high heat loads or possible property variation in different CFC batches due to the manufacturing process. Future work could include investigations into these topics.

Parametric studies were performed to investigate the effects of a non-uniform thermal contact resistance and misaligned CFC fibers in the monoblock geometry. The model setup, conditions, and post-processing were utilized from Section 6.2 for these studies with one

exception. The turbulence model utilized in this study was the SST model, which differs from the model utilized in the preceding chapters. Previous monoblock studies [53, 74] were performed by this author with the SST turbulence model because it was presumed to be superior to the other models. The results shown in Chapters 4 and 5 of this work suggest that the turbulence models yield different global values, but they capture the same general features in the flow field. In this section, the global values are not the focus, but rather the effect of the different manufacturing features on the solution. Thus, it was determined that the same behaviors could be viewed in these solutions regardless of the turbulence model implemented.

The use of the SST turbulence model for this work necessitated a different mesh than the one highlighted in Figure 6.7. The SST model requires a refined mesh with a suggested non-dimensional wall coordinate of $y^+<1$. A similar approach was taken to refine the mesh as discussed in Section 6.2.2. A mesh study was performed for the highest peak heat flux (20 MW/m$^2$), and the mesh was refined successively until the maximum temperature in the solids, the average water temperature at the outlet, and the pressure drop changed less than 1% from case to case. The same mesh was used for all peak heat fluxes investigated. The meshing criterion was chosen such that an average volume non-dimensional wall coordinate of $y^+\approx<1$ was generated for the highest PHF. This required the use of a smaller first wall height and a more refined overall mesh on the solid portions than was shown in Figure 6.7, which resulted in a larger mesh and higher computational runtimes.

### *6.6.1. Investigation of Non-Uniform Thermal Contact Resistance*

Two parametric studies were completed to study the effect of a non-uniform thermal contact resistance (TCR) between the CFC and the AMC® interlayer. The first was a "baseline" case in which a constant TCR was implemented. A circumferentially varying TCR was created for the second case in order to simulate the potential variation that could occur as a result of the circumferential bonding process. Equation 6.1 was created for the contact conductance (cc) on the armor-interlayer interface; the cc was set to vary from

$1x10^4$ to $1.5x10^6$ W/m$^2$K from the sides to the top and bottom of the tube, respectively [74].

$$cc = 7.45 \times 10^5 \cos(2\theta - \pi) + 7.55 \times 10^5 \quad (6.1)$$

The angular coordinate in Eq. 6.1 is shown in Figure 6.10. The TCR was entered into ANSYS CFX as the inverse of the cc. The applied TCR is presented in Figure 6.38, where the resistance is higher at the sides compared to the rest of the tube.

The computational results from the parametric studies were compared to the prototype experimental data as discussed in Section 6.3.1 and Ref. [53]. Figures 6.39 and 6.40 show the comparisons at the center and edges of the monoblock, respectively. Because the computational solutions revealed no notable asymmetry at the edge, the results shown in Figure 6.40 were taken at the Edge 1 location as shown in Figure 6.9. Similarly to Section 6.3.1, the computational results at the center of the monoblock are lower than the experimental data at PHF of 10.5 and 15 MW/m$^2$. However, at a PHF of 20 MW/m$^2$, the simulations yield results near the bottom of the experimental range. The results are once again closer to the experiments at the edge locations as seen in Figure 6.40. The simulations are near the bottom range of the experimental data for a PHF of 10.5 MW/m$^2$, and they fall within the range of experimental data at a PHF of 15 MW/m$^2$. Note that the experimental data at a PHF of 20 MW/m$^2$ along the edges was thrown out by the authors; further insight into this decision can be found in Ref. [53].

The circumferential temperature distributions for the two TCR cases are shown in Figure 6.41. These distributions highlight the difference between a uniform and non-uniform TCR. Note that the temperature remains below saturation for a PHF of 10.5 MW/m$^2$ in these studies, which is in contrast to the results seen in Figure 6.14. The lower temperatures seen in Figure 6.41 are due to the implementation of the SST turbulence for these particular solutions.

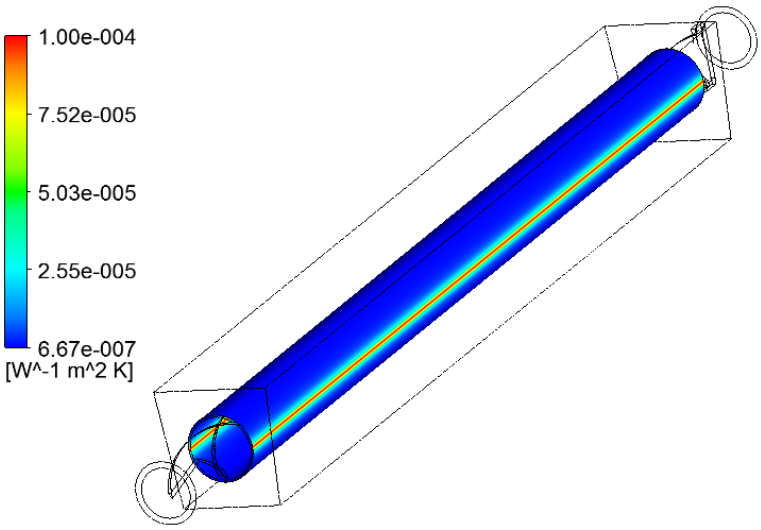


Figure 6.38: Implemented non-uniform TCR on the armor-interlayer interface [74]

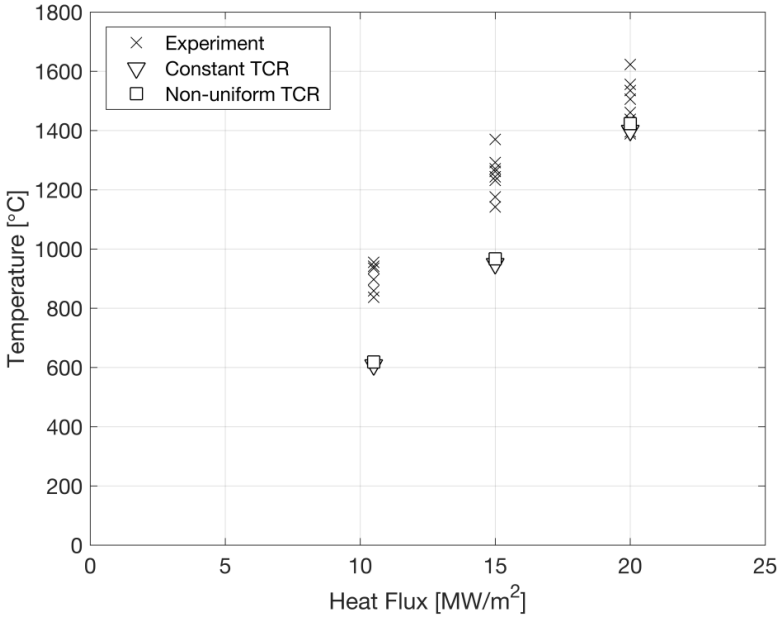


Figure 6.39: Comparison of experimental [53] and CFX results at the center of the monoblock for a parametric investigation of the TCR [74]

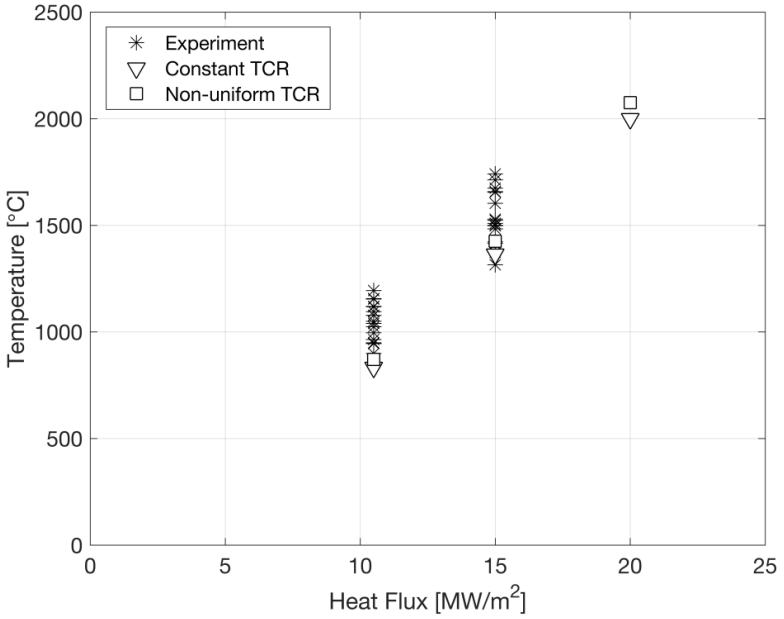


Figure 6.40: Comparison of experimental [53] and CFX results at the edges of the monoblock for a parametric investigation of the TCR [74]

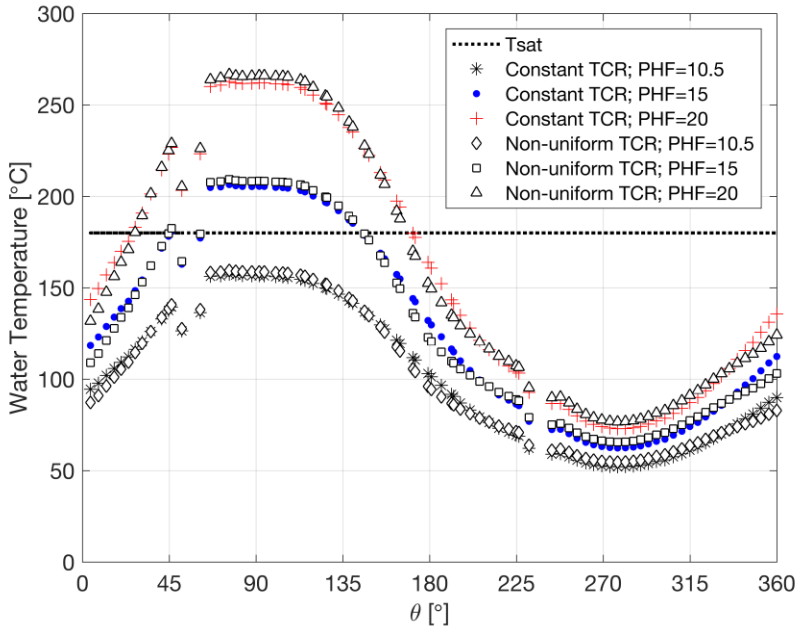


Figure 6.41: Circumferential temperature distributions at the location of peak heat flux for a parametric investigation of the TCR [74]

As shown in Chapter 4, the SST model yielded higher Nusselt number values and lower temperatures when compared to the k-eps model (which was used to generate Figure 6.14). Generally, there appears to be a minimal effect due to the circumferentially varying TCR. As expected, the sides of the tube show the largest difference in the temperature distribution where the TCR was higher, but there looks to be a limited effect along the rest of the circumference.

### *6.6.2. Investigation of CFC Fiber Misalignment*

The data from the prototype experiments revealed a notable difference between the surface temperature at the two edge locations [53], which was not noted in the computational results. One explanation behind this temperature difference could be the misaligned fibers in the CFC. A minor misalignment of the fibers during the manufacturing process could lead to misaligned thermal properties.

The CFC thermal conductivity was implemented as orthotropic and temperature dependent according to Ref. [76-78]. To simulate a potential misalignment of CFC fibers, the thermal properties were defined based on a rotated coordinate frame in CFX as shown in Figure 6.42. The study was performed for a PHF of 10.5 MW/m$^2$ and a non-uniform TCR as shown in Figure 6.38. The coordinate frame for the thermal properties was rotated by three angles ($\phi$=1.7, 3, and 8.5°) to create a new reference frame ($y', x'$). In these cases, the peak thermal conductivity was no longer acting in the normal direction (-$x$), but instead was imposed $\phi$° off normal.

The rotated CFC properties yielded asymmetries in the surface temperature similar to those seen in the experiments. Figure 6.43 shows the surface temperature contour for the largest rotation angle investigated. A comparison between the edge temperature difference ($\Delta T_{edges}$) from the experiments [53] and the simulations is presented in Figure 6.44.

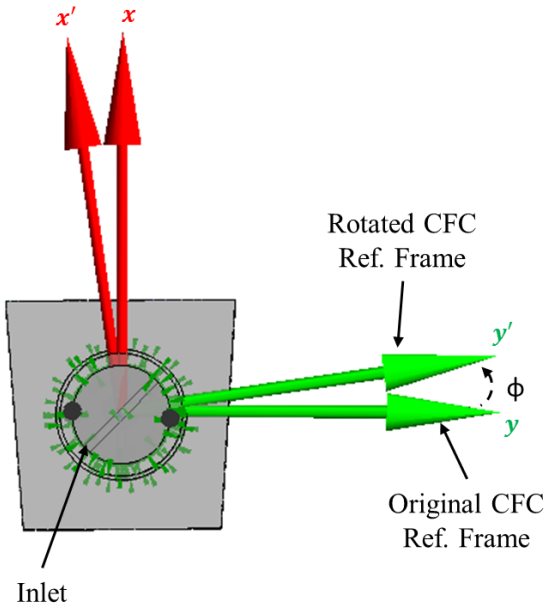


Figure 6.42: Rotated coordinate frame for CFC thermal properties in investigation of fiber misalignment [74]

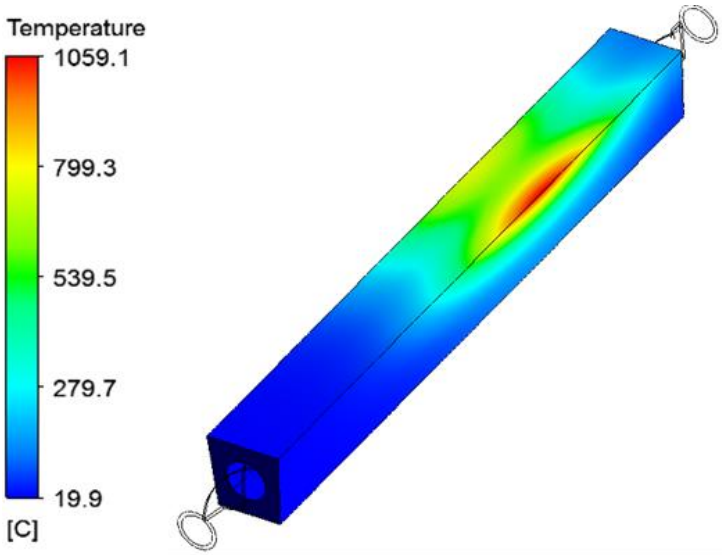


Figure 6.43: Surface temperature for rotated CFC fibers (ϕ=8.5°) with a PHF of 10.5 MW/m$^2$ [74]

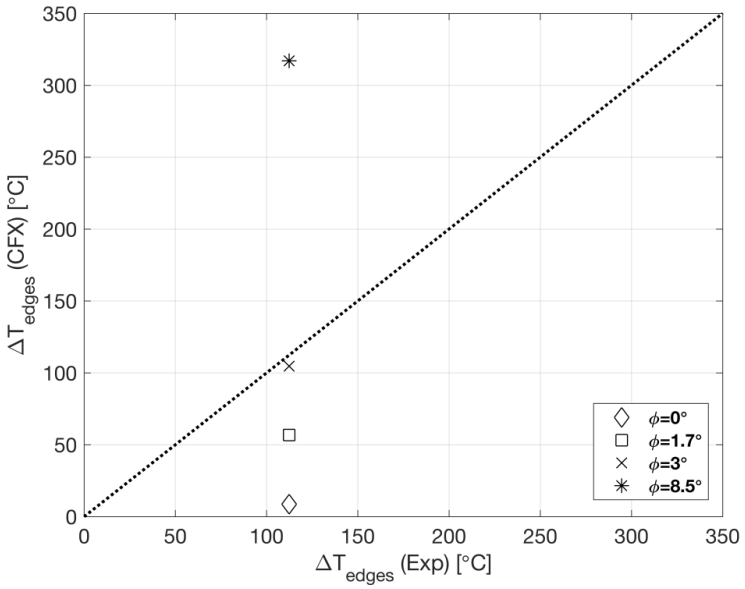


Figure 6.44: Comparison of edge temperature differences ($\Delta T_{edges}$) between experimental [53] and computational results at various CFC fiber rotation angles [74]

The average $\Delta T_{edges}$ for a PHF of 10.5 MW/m² was roughly 112°C in the experimental setting. The $\Delta T_{edges}$ yielded in the simulations is plotted directly against this average value from the experiments. Figure 6.44 shows that a rotation of ϕ=3° gives an edge temperature difference similar to the average value noted in the experiments. This reveals that even small angles of fiber misalignment can result in asymmetries at the outer monoblock edges.

## 6.7. Summary of Key Conclusions

The computational investigation with the monoblock geometry yielded a range of results for the fusion relevant conditions. The key conclusions from this chapter are summarized below:

- Computational results were compared to prototype testing performed in the GLADIS high heat flux test facility [53]. Discrepancies were noted between the experimental results and the simulations. In the experimental setting, there was a notable difference in the edge temperatures, but this was not significant in the

simulations. The computational results underpredicted the experimental values for a PHF of 10.5 and 15 MW/m$^2$ and fell within the experiments for a PHF of 20 MW/m$^2$ at the monoblock center. The simulations yielded results that were closer to the experimental data at the monoblock edges.

- Solutions were completed for W7-X relevant conditions with three peak heat fluxes (10.5, 15, and 20 MW/m$^2$). For all applied heat fluxes, the water surpassed saturation conditions along the top of the tube. Thus, subcooled boiling would be expected to occur on the top surface while convection would dominate near the bottom of the tube. Furthermore, extreme temperatures were also noted in the CFC, which exceeded the given design limits for the W7-X scraper element.
- Boiling regions were seen to cover a notable portion of the water domain, especially for the higher applied heat fluxes. The assumptions and governing parameters for the single-phase model begin to break down as the water temperature approaches the saturation temperature. These results highlight the need for the inclusion of the second phase in fusion relevant simulations.
- Potential causes for the differences between experimental and computational data could lie in the manufacturing process of the monoblock prototypes. Two possible explanations were investigated: 1) a non-uniform thermal contact resistance at the armor-interlayer interface resulting from the circumferential casting process and 2) a potential misalignment of CFC fibers. It was shown that a non-uniform thermal contact resistance had a limited impact on the solution. However, the misalignment of CFC fibers could be a potential answer to the discrepancy between the simulations and measurements. Future work could include investigations into potential degradation of CFC properties under high heat loads or possible property variation across CFC batches due to the manufacturing process.
- Local flow information was analyzed at fusion relevant conditions to determine if inflow regions and wall shear stress striping still occurs in this extreme environment. Inflow regions and shear stress striping were shown to still occur at fusion relevant conditions. However, the connection between these regions and the

surface temperature was shown to be minimal under one-sided, high heat flux conditions.

- The lack of a prevalent connection between the surface temperature and wall shear stress prompted further investigation into the relationship. Multiple avenues were explored including the following: the global effect on the full water contours, the IAPWS water properties at extreme temperatures, the near wall behavior, and the relationship at lower peak heat fluxes. The conclusions are summarized below:
    - The full contours revealed a noticeable effect on the wall heat flux due to the wall shear stress striping. However, there was a minimal impact on the temperature.
    - Investigation into the IAPWS water properties indicated that the fusion relevant investigation was stretching the limits of the single-phase model.
    - Analysis of the near wall behavior showed extreme temperature gradients at axial locations with significant applied heat flux. While large gradients are to be expected with twisted tape devices, this information could be used as a justification for the use of a low Reynolds number approach for the turbulence modeling where the solution can be resolved down to the wall.
    - Even at much lower peak heat fluxes (1 and 5 $MW/m^2$), the connection between the wall shear stress and the surface temperature was not prevalent.
- Overall, the fusion relevant investigation suggested that the effects of the wall shear stress striping on the surface temperature were minimal for one-sided, non-uniform heating conditions. The change in temperature due to the decreased wall shear stress was minimal when compared to the change in temperature due to the applied heat flux. Consideration of the results presented in previous chapters indicates that this phenomenon is more important for uniform, moderate heating applications.

# Chapter 7: Conclusions

## 7.1. Summary of the Work

The goal of this work was to perform a computational investigation into the thermal-hydraulic performance of water-cooled, twisted tape enabled high heat flux components at fusion relevant conditions. Fusion energy is a promising option for future clean energy generation, but the community must overcome significant scientific and engineering challenges before meeting the goal of electricity generation. One such challenge is the high heat flux thermal management of components in fusion and plasma physics experiments. Plasma facing components in the magnetic confinement devices, such as ITER or W7-X, will be subjected to extreme heat loads on the order of 10-20 $MW/m^2$. The heat dissipation issue will become critical as these next generations of experiments come online, and active cooling will be necessary to decrease the thermal loading and prevent failure of the components.

Initial investigations of water-cooled PFCs intended for use in W7-X revealed the need to include subcooled nucleate boiling in the computational model [3]. Following an investigation into two-phase modeling options, it was determined that an accurate single-phase twisted tape induced swirl flow model was a pre-requisite to the addition of the second phase. The research was then shifted to single-phase modeling of water-cooled twisted tape devices.

While there have been a substantial number of experimental studies to study the twisted tape devices, there have been fewer computational studies. Furthermore, a majority of these computational works have focused on the determination of global thermal-hydraulic design characteristics rather than investigating the local flow features. Unfortunately, this approach generally excludes the benefit of computational solutions where local flow information can be extracted more easily than in an experimental setting. This research exploited the advantage of computational simulations by analyzing the local flow

information and by drawing connections between those local features and the thermal-hydraulic performance.

Following a brief discussion of the twisted tape and CFD background, the work was completed for two different geometries and heating conditions. The initial investigation was performed for a general geometry of a tube equipped with a twisted tape insert. There were two main goals for this study. The first was to investigate the capability of the ANSYS CFX software to solve the twisted tape induced flow field, and the second was to analyze the local flow field and draw connections to the thermal-hydraulic performance. The investigation was perfomed for both adiabatic and diabatic conditions. For validation purposes, the diabatic heating conditions were chosen to be moderate and uniform. The general geometry and moderate conditions were also utilized in a parametric study to determine the effect of various twist ratios on the diabatic solutions. The results were compared to legacy correlations as well as experimental data for multiple twist ratios, and the influence of the twist ratio on the local flow information was discussed. Lastly, the computational investigation was extended to a fusion relevant geometry and conditions. The monoblock concept was implemented for this study, and conditions were chosen to align with the interests of the W7-X experiment—from which this work was generously funded. Computational results were compared to experimental values from W7-X prototype testing, and local flow features were analyzed for fusion relevant conditions.

## 7.2. Key Conclusions

### *7.2.1. Summary for a Tube Equipped with a Twisted Tape Insert*

The computational investigation and parametric twist ratio study for a tube equipped with a twisted tape yielded a wide range of results. The general geometry was investigated for a range of thermal-hydraulic conditions which consisted of adiabatic and diabatic cases. In the diabatic studies, the heating conditions were chosen to be moderate and uniform.

It was determined that global parameter calculations, such as the Fanning friction factor and Nusselt number, were credible when compared to the legacy twisted tape correlations [13-17, 22] as well as experimental data [14, 17]. A better thermal performance was noted

for higher Reynolds numbers, higher applied heat fluxes, and lower twist ratios. However, this typically comes with a higher friction factor penalty, and so an acceptable balance must be determined for twisted tape devices.

Furthermore, flow pattern predictions were qualitatively similar to legacy flow visualization experiments [22, 23]. Fully developed flow was not noted in this study as the flow field continued to change downstream for all conditions and twist ratios investigated. In all cases, the secondary circulation resulted in so-called "inflow" regions where the boundary layer fluid is reinjected into the freestream. These regions were shown to correspond to regions of low wall shear stress, low heat transfer coefficients, and high surface temperatures for the moderate, uniform heating conditions. Investigation of wall shear stress contours revealed apparent "striping" that develops in twisted tape induced swirl flow. The striping represents the inflow regions along the water-solid interfaces; the number and location of the stripes varied along the length of the test section and for different twist ratios.

The study also gave insight in to the CFD implementation for twisted tape induced swirl flow. The choice of turbulence model appeared to have little impact on the friction factor at higher Reynolds numbers. On the other hand, the Nusselt number was more affected, and a large variation was noted for difference models investigated. The curvature correction method by Spalart and Shur [47] appeared to have more of an effect at lower Reynolds numbers. At higher Reynolds numbers, the addition of the curvature correction coefficient (as implemented in this work) did not appear to have a significant impact on the solution for either adiabatic or diabatic conditions. Locally, the same qualitative features were captured across turbulence models. However, the flow patterns themselves varied for each turbulence model investigated. It was concluded that more detailed flow visualization experiments are needed to determine which model provides the most accurate representation of twisted tape induced swirl flow. Furthermore, a fully mesh independent solution was not achieved even with the addition of a transient mesh refinement study. Key qualitative features were captured, and the global hydraulic parameter reached a constant value. However, the flow field continued to change as the mesh was refined. This revealed

the need for a detailed transient study and for the development of CFD best practices for twisted tape induced swirl flow.

### *7.2.2. Summary for a Monoblock Geometry at Fusion Relevant Conditions*

Following the initial investigations at uniform and moderate heating conditions, the focus was shifted to fusion relevant conditions. This work was performed on a monoblock geometry with W7-X relevant parameters, and it yielded a wide range of results. The simulations were compared to prototype testing performed in the GLADIS high heat flux test facility [53]. The computational results underpredicted the experiments in some cases and fell within the data for others. It was determined that boiling can be expected to occur in localized regions along the top surface of the tube while convection would dominate near the bottom of the tube. Boiling regions covered a significant portion of the water domain, especially for the higher heat fluxes. Thus, the assumptions and governing parameters for the single-phase model were breaking down in these regions. These results add to the literature highlighting the need to include the second phase in fusion relevant simulations.

Discrepancies were noted between the simulations and the prototype testing data. Potential causes for these differences were identified in the prototype manufacturing process. Two possible explanations were investigated including 1) a non-uniform thermal contact resistance at the armor-interlayer interface due to the circumferential casting process and 2) a potential misalignment of CFC fibers. It was concluded that a non-uniform thermal contact resistance had a limited impact on the solution. However, the misalignment of CFC fibers could serve as a potential answer to the discrepancy between the simulations and measurements. Future work could include investigations into potential degradation of CFC properties under high heat loads or possible property variation across CFC batches due to the manufacturing process.

Local flow information was analyzed at fusion relevant conditions to determine if inflow regions and wall shear stress striping still occurred. These phenomena were shown to occur in this extreme environment. However, the connection between the inflow regions

and the surface temperature was concluded to be minimal under one-sided, high heat flux conditions. The lack of a prevalent connection between the surface temperature and wall shear stressed led to further investigation of the relationship. Four avenues were explored including 1) the global effect on the full water contours, 2) the IAPWS water properties at extreme temperatures, 3) the near wall behavior, and 4) the relationship at lower peak heat fluxes. These studies showed that the fusion relevant investigation was stretching the limits of the single-phase model and revealed large temperature gradients in the near wall region, which could be used as a justification for a low Reynolds number approach for the turbulence modeling. Even at much lower peak heat fluxes, the connection between the wall shear stress and surface temperature was not prevalent.

Overall, the fusion relevant investigation suggested that the effects of the inflow regions and wall shear stress striping on the surface temperature are minimal for one-sided, non-uniform heating conditions. The change in temperature due to the decreased wall shear stress was minimal when compared to the change in temperature due to the applied heat flux. Consideration of the results for general geometry indicates that this phenomenon is more relevant for moderate, uniform heating applications.

## 7.3. Opportunities for Future Work

The computational investigations of fusion relevant twisted tape components performed in this work revealed a host of opportunities for continued research on the topic. The addition of a two-phase model due to the expected boiling is an obvious task. However, there is also work to be done on a single-phase model at lower peak heat fluxes. On the purely computational side, high fidelity transient simulations should be performed to obtain a mesh-independent solution. Such simulations could be used to develop a CFD “best practices” guide to modeling twisted tape induced swirl flow. Considering the lack of consensus in the computational literature, this guide would be extremely useful to the community. As part of that guide, the computational solutions could be performed with the Reynolds stress turbulence model, which has been shown to outperform two-equation eddy viscosity models. High fidelity transient solutions can also provide better insight into

how and where the inflow regions (and the corresponding wall shear stress stripes) develop.

On the fusion side, solutions can be performed with a tungsten monoblock instead of the CFC armor used in this work. Tungsten is currently the most popular armor material for magnetic confinement devices, and so, the study would be valuable within the fusion community. Furthermore, the inclusion of tungsten rather than CFC would eliminate the modeling complications due to CFC manufacturing processes. The isotropic tungsten material properties may also lead to a different relationship between the wall shear stress and surface temperature because the isotropic thermal conductivity would likely allow for more diffusion throughout the solid.

Lastly, this research has highlighted the lack of experimental data available for validation. This is not only true for fusion relevant regimes but also for moderate, uniform heating conditions. Without more detailed flow visualization experiments, it is unclear which turbulence model provides the most accurate representation of the twisted tape induced swirl flow. Other useful experimental data could include circumferential temperature distributions at different axial locations or typical circumferential locations of burnout for twisted tape enable devices. Both sets of results would aid in the validation of computational models and would lead to a better understanding of twisted tape induced swirl flow.

# References

[1] G. Federici, R. Kemp, D. Ward, C. Bachmann, T. Franke, S. Gonzalez*, et al.*, "Overview of EU DEMO design and R&D activities," *Fusion Engineering and Design,* vol. 89, pp. 882-889, 2014.

[2] R. E. Nygren, "Science in Fusion Technology," *Fusion Science and Technology,* vol. 61, pp. 52-57, 2012.

[3] E. Clark, A. Lumsdaine, J. Boscary, K. Ekici, J. Harris, D. McGinnis*, et al.*, "Multiphysics analysis of the Wendelstein 7-X actively cooled scraper element," *Fusion Science and Technology,* vol. 68, pp. 635-639, 2015.

[4] A. Cardella, G. Vieider, E. Di Pietro, A. Orsini, M. Sacchetti, D. Ciric*, et al.*, "Design, manufacturing and thermo-mechanical testing of a relevant size monoblock divertor prototype," in *Fusion technology 1994. Proceedings. Vol. 1*, ed, 1995.

[5] S. Nakamura, S. Sakurai, H. Ozaki, Y. Seki, K. Yokoyama, A. Sakasai*, et al.*, "Infrared thermography inspection for monoblock divertor target in JT-60SA," *Fusion Engineering and Design,* vol. 89, pp. 1024-1028, 2014.

[6] N. Kurul and M. Podowski, "On the modeling of multidimensional effects in boiling channels," in *ANS Proc. 27th National Heat Transfer Conference, Minneapolis, MN*, 1991, pp. 28-31.

[7] G. Bartolomei and V. Chanturiya, "Experimental study of true void fraction when boiling subcooled water in vertical tubes," *Thermal Engineering,* vol. 14, pp. 123-128, 1967.

[8] R. M. Manglik and A. E. Bergles, "Swirl Flow Heat Transfer and Pressure Drop with Twisted-Tape Inserts," in *Advances in Heat Transfer*. vol. 36, J. P. Hartnett and T. F. Irvine, Eds., ed San Diego: Elsevier Science, 2002, pp. 183-266.

[9] S. Aravamuthan, G. S. Rathore, R. Pradhan, and R. T. K. Raj, "Numerical and Experimental Investigation of In-Cylinder Swirl Flow Using Twisted Tape in Diesel Engines," SAE Technical Paper 0148-7191, 2013.

[10] A. Kumar and B. Prasad, "Investigation of twisted tape inserted solar water heaters—heat transfer, friction factor and thermal performance results," *Renewable Energy,* vol. 19, pp. 379-398, 2000.

[11] E. Clark, A. Lumsdaine, K. Ekici, and A. E. Ruggles, "Computational Investigation of the Thermal-Hydraulic Performance for Twisted Tape Enabled High Heat Flux Components," *Accepted for Publication in Fusion Science and Technology,* 2017.

[12] R. Manglik and A. Bergles, "Heat transfer and pressure drop correlations for twisted-tape inserts in isothermal tubes: part I--laminar flows," *Transactions-American Society Of Mechanical Engineers Journal Of Heat Transfer,* vol. 115, pp. 881-881, 1993.

[13] W. Gambill and R. Bundy, "An evaluation of the present status of swirl-flow heat transfer," Oak Ridge National Lab., Tenn.1961.

[14] R. Lopina and A. Bergles, "Heat transfer and pressure drop in tape-generated swirl flow of single-phase water," *Journal of Heat Transfer,* vol. 91, pp. 434-441, 1969.

[15] R. M. Manglik and A. E. Bergles, "Heat transfer and pressure drop correlations for twisted-tape inserts in isothermal tubes: Part II—Transition and turbulent flows," *Journal of Heat Transfer,* vol. 115, pp. 890-896, 1993.

[16] M. Ibragimov, E. Nomsfelov, and V. Subbotin, "Heat transfer and hydraulic resistance with swirl-type motion of liquid in pipes," *Teploenergetika,* vol. 8, pp. 57-60, 1961.

[17] W. Gambill, R. Bundy, and R. Wansbrough, "Heat transfer, burnout, and pressure drop for water in swirl flow through tubes with internal twisted tapes," Oak Ridge National Lab., Tenn.1960.

[18] G. J. Kidd, "Heat transfer and pressure drop for nitrogen flowing in tubes containing twisted tapes," *AIChE Journal,* vol. 15, pp. 581-585, 1969.

[19] R. Manglik and A. Bergles, "Heat transfer enhancement and pressure drop in viscous liquid flows in isothermal tubes with twisted-tape inserts," *Wärme-und Stoffübertragung,* vol. 27, pp. 249-257, 1992.

[20] M. Araki, M. Ogawa, T. Kunugi, K. Satoh, and S. Suzuki, "Experiments on heat transfer of smooth and swirl tubes under one-sided heating conditions," *International journal of heat and mass transfer,* vol. 39, pp. 3045-3055, 1996.

[21] A. V. Dedov, A. T. Komov, A. N. Varava, and V. V. Yagov, "Hydrodynamics and heat transfer in swirl flow under conditions of one-side heating. Part 1: Pressure drop

and single-phase heat transfer," *International Journal of Heat and Mass Transfer,* vol. 53, pp. 4123-4131, 2010.

[22] E. V. Seymour, "Fluid flow through tubes containing twisted tapes(Pressure losses and improved heat transfer in incompressible fluid flow through tubes containing twisted tapes)," *The Engineer,* vol. 222, pp. 634-642, 1966.

[23] E. Smithberg and F. Landis, "Friction and forced convection heat-transfer characteristics in tubes with twisted tape swirl generators," *Journal of Heat Transfer,* vol. 86, pp. 39-48, 1964.

[24] W. Jones and B. Launder, "The prediction of laminarization with a two-equation model of turbulence," *International journal of heat and mass transfer,* vol. 15, pp. 301-314, 1972.

[25] A. Date, "Prediction of fully-developed flow in a tube containing a twisted-tape," *International Journal of Heat and Mass Transfer,* vol. 17, pp. 845-859, 1974.

[26] K. Hata, Y. Shirai, S. Masuzaki, and A. Hamura, "Computational study of twisted-tape-induced swirl flow heat transfer and pressure drop in a vertical circular tube under velocities controlled," *Nuclear Engineering and Design,* vol. 263, pp. 443-455, 2013.

[27] A. Lumsdaine, J. Boscary, E. Clark, K. Ekici, J. Harris, D. McGinnis*, et al.*, "Modeling and analysis of the W7-X high heat-flux divertor scraper element," *IEEE Transactions on Plasma Science,* vol. 42, pp. 545-551, 2014.

[28] M. Rahimi, S. R. Shabanian, and A. A. Alsairafi, "Experimental and CFD studies on heat transfer and friction factor characteristics of a tube equipped with modified twisted tape inserts," *Chemical Engineering and Processing: Process Intensification,* vol. 48, pp. 762-770, 2009.

[29] S. Eiamsa-Ard, K. Wongcharee, and S. Sripattanapipat, "3-D Numerical simulation of swirling flow and convective heat transfer in a circular tube induced by means of loose-fit twisted tapes," *International Communications in Heat and Mass Transfer,* vol. 36, pp. 947-955, 2009.

[30] W. Liu and B. Bai, "A numerical study on helical vortices induced by a short twisted tape in a circular pipe," *Case Studies in Thermal Engineering,* vol. 5, pp. 134-142, 2015.

[31] Y.-Z. Cui and M.-C. Tian, "Three-dimensional numerical simulation of thermal-hydraulic performance of a circular tube with edgefold-twisted-tape inserts," *Journal of Hydrodynamics, Ser. B,* vol. 22, pp. 662-670, 2010.

[32] Y.-G. Lei, C.-H. Zhao, and C.-F. Song, "Enhancement of turbulent flow heat transfer in a tube with modified twisted tapes," *Chemical Engineering & Technology,* vol. 35, pp. 2133-2139, 2012.

[33] T. O. Oni, "Numerical investigation of heat transfer and fluid flow in tubes induced with twisted tape inserts," University of Glasgow, 2015.

[34] T. O. Oni and M. C. Paul, "CFD Investigation of the Impacts of Variation in Geometry of Twisted Tape on Heat Transfer and Flow Characteristics of Water in Tubes," *Heat Transfer—Asian Research,* 2016.

[35] R. Yadav and A. Padalkar, "CFD analysis for heat transfer enhancement inside a circular tube with half-length upstream and half-length downstream twisted tape," *Journal of Thermodynamics,* vol. 2012, 2012.

[36] F. P. Incropera, D. P. Dewitt, T. L. Bergman, and A. S. Lavine, *Fundamentals of Heat and Mass Transfer* 6th ed. New Jersey: John Wiley & Sons, 2007.

[37] ANSYS, "ANSYS CFX-Solver Modeling Guide," ANSYS, Inc., Canonsburg, PA2013.

[38] ANSYS, "ANSYS CFX Introduction," ANSYS, Inc. , Canonsburg, PA2017.

[39] F. M. White, *Viscous Fluid Flow*, 3rd ed. New York, NY: McGraw-Hill, 2006.

[40] J. Milnes, "Computational modelling of the hypervapotron cooling technique for nuclear fusion applications," Ph.D., Department of Aerospace Sciences, Cranfield University, Cranfield, UK, 2010.

[41] CFD-Online. (March 17, 2017). *Navier-Stokes equations*. Available: https://www.cfd-online.com/Wiki/Navier-Stokes_equations

[42] ANSYS, "ANSYS CFX-Solver Theory Guide," ANSYS, Inc. , Canonsburg, PA2013.

[43] H. Tennekes and J. L. Lumley, *A first course in turbulence*: MIT press, 1972.

[44] D. C. Wilcox, *Turbulence Modeling for CFD*, 3rd ed. California DCW Industries, Inc. , 2006.

[45] CFD-Online. (March 17, 2017). *Two equation turbulence models* Available: https://www.cfd-online.com/Wiki/Two_equation_turbulence_models

[46] A. S. Cocic, M. R. Lecic, and M. C. Svetislav, "Numerical analysis of axisymmetric turbulent swirling flow in circular pipe," *Therm. Sci,* vol. 18, pp. 493-505, 2014.

[47] P. Spalart and M. Shur, "On the sensitization of turbulence models to rotation and curvature," *Aerospace Science and Technology,* vol. 1, pp. 297-302, 1997.

[48] F. R. Menter, "Two-equation eddy-viscosity turbulence models for engineering applications," *AIAA journal,* vol. 32, pp. 1598-1605, 1994.

[49] C. Rumsey. (2015, March 17, 2017). *The Menter Shear Stress Transport Turbulence Model*. Available: https://turbmodels.larc.nasa.gov/sst.html

[50] F. M. White, *Fluid Mechanics*, 6th ed. Boston: McGraw-Hill, 2008.

[51] W. Frei, "Which Turblence Model Should I Choose for My CFD Application?," vol. 2017, ed: COMSOL Blog, 2013.

[52] B. Kader, "Temperature and concentration profiles in fully turbulent boundary layers," *International Journal of Heat and Mass Transfer,* vol. 24, pp. 1541-1544, 1981.

[53] J. Boscary, H. Greuner, G. Ehrke, B. Böswirth, Z. Wang, E. Clark*, et al.*, "Prototyping phase of the high heat flux scraper element of Wendelstein 7-X," *Fusion Engineering and Design,* vol. 109, pp. 773-776, 2016.

[54] W. Wagner and H. J. Kretzschmar, *International Steam Tables: Properties of Water and Steam Based on the Industrial Formulation IAPWS-IF97*, 2nd ed. Berlin, Germany: Springer, 2008.

[55] R. M. Manglik, "Heat transfer enhancement of intube flows in process heat exchangers by means of twisted-tape inserts," Doctor of Philosophy Ph.D. Dissertation, Mechanical Engineering, Rensselaer Polytechnic Institute, Troy, New York, 1991.

[56] J. D. Anderson, *Modern compressible flow: with historical perspective*, 3rd ed. New York, NY: McGraw-Hill 2003.

[57] J. E. A. John and T. G. Keith, *Gas Dynamics*, 3rd ed. Upper Saddle River, New Jersey: Pearson Education, Inc., 2006.

[58] F. P. Incropera, D. P. Dewitt, T. L. Bergman, and A. S. Lavine, *Fundamentals of Heat and Mass Transfer*, 6th ed. New Jersey: John Wiley & Sons, 2007.

[59] T. Dormer Jr. and A. E. Bergles, "Pressure Drop with Surface Boiling in Small-Diameter Tubes," Massachusetts Institute of TechnologySeptember 1, 1964 1964.

[60] Y. A. Gostintsev, "Heat and mass transfer and hydraulic resistance for swirling pipe flow," *Fluid Dynamics,* vol. 3, pp. 76-78, 1968.

[61] T. Satoh, K. Yuki, S.-y. Chiba, H. Hashizume, and A. Sagara, "Heat transfer performance for high Prandtl and high temperature molten salt flow in sphere-packed pipes," *Fusion Science and Technology,* vol. 52, pp. 618-624, 2007.

[62] A. Raffray, J. Schlosser, M. Akiba, M. Araki, S. Chiocchio, D. Driemeyer*, et al.*, "Critical heat flux analysis and R&D for the design of the ITER divertor," *Fusion Engineering and Design,* vol. 45, pp. 377-407, 1999.

[63] K. Ezato, M. Dairaku, M. Taniguchi, K. Sato, S. Suzuki, M. Akiba*, et al.*, "Development of ITER divertor vertical target with annular flow concept-I: Thermal-hydraulic characteristics of annular swirl tube," *Fusion science and technology,* vol. 46, pp. 521-529, 2004.

[64] J. Boscary, J. Fabre, and J. Schlosser, "Critical heat flux of water subcooled flow in one-side heated swirl tubes," *International Journal of Heat and Mass Transfer,* vol. 42, pp. 287-301, 1999.

[65] Y. Bournonville, M. Grandotto, S. Pascal-Ribot, P. Spitz, and F. Escourbiac, "Numerical simulation of swirl-tube cooling concept, application to the ITER project," *Fusion Engineering and Design,* vol. 84, pp. 501-504, 2009.

[66] R. Koch, "Pressure Loss and Heat Transfer for Turbulent Flow," *VDI Forschungshaft,* vol. 24, pp. 1-44, 1958.

[67] L. Feinstein and R. Lundberg, "Fluid friction and boiling heat transfer with water in vortex flow in tubes containing an internal twisted tape," *Rome Air Development Center Report RADC-TDR-63-451,* 1963.

[68] M. Missirlian, J. Bucalossi, Y. Corre, F. Ferlay, M. Firdaouss, P. Garin*, et al.*, "The WEST project: Current status of the ITER-like tungsten divertor," *Fusion Engineering and Design,* vol. 89, pp. 1048-1053, 2014.

[69] M. Merola, D. Loesser, A. Martin, P. Chappuis, R. Mitteau, V. Komarov*, et al.*, "ITER plasma-facing components," *Fusion Engineering and Design,* vol. 85, pp. 2312-2322, 2010.

[70] T. Hirai, F. Escourbiac, V. Barabash, A. Durocher, A. Fedosov, L. Ferrand*, et al.*, "Status of technology R&D for the ITER tungsten divertor monoblock," *Journal of Nuclear Materials,* vol. 463, pp. 1248-1251, 2015.

[71] T. Hirai, F. Escourbiac, S. Carpentier-Chouchana, A. Fedosov, L. Ferrand, T. Jokinen*, et al.*, "ITER tungsten divertor design development and qualification program," *Fusion Engineering and Design,* vol. 88, pp. 1798-1801, 2013.

[72] R. Pitts, S. Carpentier, F. Escourbiac, T. Hirai, V. Komarov, S. Lisgo*, et al.*, "A full tungsten divertor for ITER: physics issues and design status," *Journal of Nuclear Materials,* vol. 438, pp. S48-S56, 2013.

[73] H. Greuner, H. Bolt, B. Böswirth, T. Franke, P. McNeely, S. Obermayer*, et al.*, "Design, performance and construction of a 2MW ion beam test facility for plasma facing components," *Fusion engineering and design,* vol. 75, pp. 345-350, 2005.

[74] E. Clark, A. Lumsdaine, J. Boscary, H. Greuner, and K. Ekici, "Thermal-hydraulics modeling for prototype testing of the W7-X high heat flux scraper element," *Submitted to Fusion Engineering and Design,* 2017.

[75] J. Boscary, "Personal Communication," ed, 2015.

[76] V. Barabash and C. H. Wu, "ITER Material Properties Handbook," 2000.

[77] J. P. Bonal, "Thermal properties of carbon fiber composites before irradiation in Paride 3/4 experiment."

[78] J. P. Bonal and D. Moulinier, "Thermal properties of advanced carbon fiber composites for fusion application," Commis. Energ. At.1995.

[79] A. Lumsdaine, "Personal Communication," ed, 2015.

[80] A. Lumsdaine, "Personal Communication," ed, 2014.

# Vita

Emily Buckman Clark was born as Emily Michelle Buckman in 1989 to Diana and Mitch Buckman in Panama City, Panama. Emily's father, an Army Captain and a Ranger, retired from the military, and the family settled down in Morristown, TN when she was four years old. Emily's interest in science was sparked at an early age. Her father owns a small airplane, and she spent countless hours flying with him and her mother. She would often look out and ask questions about how flight or weather or navigation worked. Those experiences undoubtedly inspired her to become an aerospace engineer.

This career path was enabled by her education in the Tennessee school system. Emily attended Morristown-Hamblen High School West and graduated with honors in 2007. The Tennessee HOPE and Volunteer Scholarships empowered Emily to pursue her Bachelor's of Science degree in Aerospace Engineering at the University of Tennessee, Knoxville. She earned her degree in 2011 with Summa Cum Laude honors and was awarded the Herman Morris Scholarship as the top aerospace student in the graduating class.

Emily's research career began the following summer in the Volkswagen Distinguished Scholars Program at the National Transportation Research Center—a user facility of Oak Ridge National Laboratory (ORNL). She went on to earn a Master's of Science degree in Aerospace Engineering at the University of Tennessee, Knoxville under the support of Dr. Kivanc Ekici. While earning this degree, Emily performed a diverse range of research topics including computational fluid dynamics research at Wright Patterson Air Force Base and thermal-fluids modeling at ORNL.

Emily married her high school sweetheart, John Clark, in May 2013 and completed her M.S. degree in August of the same year. Following graduation, Emily continued her graduate education under the Energy Science and Engineering Fellowship in the Bredesen Center for Interdisciplinary Research and Graduate Education. As a Bredesen Center Fellow, Emily was afforded the opportunity to perform research at ORNL during the pursuit of her Ph.D. She continued her work on thermal-fluids modeling in the Fusion and Materials for Nuclear Systems Division at ORNL under the support of the Office of Fusion

Energy Sciences for collaboration with the Wendelstein 7-X plasma physics project. She was guided under the direction of Dr. Arnold Lumsdaine and Dr. Kivanc Ekici.

In the spring of 2017, Emily was invited to the Alan Alda Center for Communicating Science Workshop held at ORNL. It was here that Emily realized her passion for science communication, which led to her involvement in the local Ask A Scientist chapter and the local Taste of Science events. As part of her career, Emily hopes to bridge the gap between the scientific community and the public through science communication in order to help address society's greatest challenges and foster the next generation of scientists.

Emily will complete her Ph.D. degree in 2017. Following graduation, she will continue to engage in a challenging, application-driven career at Raytheon Missile Systems in Tucson, AZ, where she will support projects that are critical to the defense of our nation.